DISSERTATION

A COMPARISON OF TRI-POLAR CONCENTRIC RING ELECTRODES TO DISC

ELECTRODES FOR DECODING REAL AND IMAGINARY FINGER MOVEMENTS

Submitted by

Saleh Ibrahim Alzahrani

Graduate Degree Program in Bioengineering

In partial fulfillment of the requirements

For the Degree of Doctor of Philosophy

Colorado State University

Fort Collins, Colorado

Spring 2019

Doctoral Committee:

Advisor: Charles W. Anderson

Jozsef Vigh
Don Rojas
Salah Abdel-Ghany

ABSTRACT

A COMPARISON OF TRI-POLAR CONCENTRIC RING ELECTRODES TO DISC

ELECTRODES FOR DECODING REAL AND IMAGINARY FINGER MOVEMENTS

The electroencephalogram (EEG) is broadly used for diagnosis of brain diseases and research of brain activities. Although the EEG provides a good temporal resolution, it suffers from poor spatial resolution due to the blurring effects of volume conduction and signal-to-noise ratio.

Many efforts have been devoted to the development of novel methods that can increase the EEG spatial resolution. The surface Laplacian, which is the second derivative of the surface potential, has been applied to EEG to improve the spatial resolution. Tri-polar concentric ring electrodes (TCREs) have been shown to estimate the surface Laplacian automatically with better spatial resolution than conventional disc electrodes.

The aim of this research is to study how well the TCREs can be used to acquire EEG signals to decode real and imaginary finger movements. These EEG signals will be then translated into finger movements commands. We also compare the feasibility of discriminating finger movements from one hand using EEG recorded from TCREs and conventional disc electrodes. Furthermore, we evaluated two movement-related features, temporal EEG data and spectral features, in discriminating individual finger from one hand using non-invasive EEG.

To do so, movement-related potentials (MRPs) are measured and analyzed from four TCREs and conventional disc electrodes while 13 subjects performed either motor execution or motor imagery of individual finger movements. The tri-polar-EEG (tEEG) and conventional EEG (cEEG) were recorded from electrodes placed according to the 10-20 International Electrode Positioning System over the motor cortex.

Our results show that the TCREs achieved higher spatial resolution than conventional disc electrodes. Moreover, the results show that signals from TCREs generated higher decoding ac-

curacy compared to signals from conventional disc electrodes. The average decoding accuracy of five-class classification for all subjects was of $70.04 \pm 7.68\%$ when we used temporal EEG data as feature and classified it using Artificial Neural Networks (ANNs) classifier. In addition, the results show that the TCRE EEG (tEEG) provides approximately a four times enhancement in the signal-to-noise ratio (SNR) compared to disc electrode signals.

We also evaluated the interdependency level between neighboring electrodes from tri-polar, disc, and disc with Hjorth's Laplacian method in time and frequency domains by calculating the mutual information (MI) and coherence. The MRP signals recorded with the TCRE system have significantly less mutual information (MI) between electrodes than the conventional disc electrode system and disc electrodes with Hjorth's Laplacian method. Also, the results show that the mean coherence between neighboring tri-polar electrodes was found to be significantly smaller than disc electrode and disc electrode with Hjorth's method, especially at higher frequencies. This lower coherence in the high frequency band between neighboring tri-polar electrodes suggests that the TCREs may record a more localized neuronal activity. The successful decoding of finger movements can provide extra degrees of freedom to drive brain computer interface (BCI) applications, especially for neurorehabilitation.

ACKNOWLEDGEMENTS

First, I would like to express my sincere appreciation and gratitude to Dr. Charles Anderson for his support, encouragement, feedback and critiques he has provided me throughout my research. Without his guidance, this work would not have come to fruition. I would also like to thank my committee members Dr. Jozsef Vigh, Dr. Don Rojas, and Dr. Salah Abdel-Ghany for their time, insights, and reviewing this dissertation. I am also grateful to Dr. Walter Besio for all the equipments he provided us to conduct this research and the time he devoted to help me. Dr. William Gavin deserves many thanks for providing his valuable comments on the preliminary results of this work. Finally and most importantly, I acknowledge with a deep sense of reverence, my gratitude towards my parents and family for their inspiration, support, and encouragement.

This dissertation is typset in LaTeX using a document class designed by Leif Anderson.

TABLE OF CONTENTS

LIST OF TABLES

LIST OF FIGURES

Chapter 1

Introduction

Brain-computer interface (BCI) is an assistive technology, which enables communication and control of a device such as a neuroprosthesis without using the brain's normal output pathways of peripheral nerves and muscles [2]. BCI systems are mainly targeted for people with severe neuro-muscular disorders such as amyotrophic lateral sclerosis (ALS), spinal cord injury, cerebral palsy, or brain stem stroke. They provide them with basic control and/or communication capabilities and determine the user's intent from a range of different electrophysiological signals, so that they can perform multiple tasks, such as controlling a wheelchair, operating a prosthetic limb, or controlling a two-dimensional cursor movement on screen [2–4].

Several neuroimaging modalities have been utilized to record and monitor the brain activity. These include electroencephalography (EEG), magnetoencephalography (MEG), positron emission tomography (PET), functional magnetic resonance imaging (fMRI), and optical imaging. Among these different modalities, scalp-recorded Electroencephalography (EEG) is considered the most commonly used modality in BCI systems. This can be attributed to several factors such as the high temporal resolution, relatively inexpensive, mobility, and measuring the brain signals with reasonable signal-to-noise ratio (SNR) [4–6].

BCI systems can be classified into two categories depending on the placement of the electrodes used to measure neurophysiological signals from the brain: invasive and noninvasive. For invasive BCIs, the electrodes are implanted directly into the brain tissue to record neural activities with high SNR and spatiotemporal resolution. Noninvasive BCIs use the brain activity measured by electrodes placed on the scalp, and for this reason they are by far the most widespread recording modality used in BCI research. However, they provide poor spatial resolution and low SNR, thereby limiting the bandwidth of control signals that can be reliably extracted.

Figure 1.1 shows the basic design and operation of any BCI system. A typical BCI system has input (e.g., the user's brain signals), output (i.e., device commands), and components that translate

1

input into output. The input of the BCI system is neural activity which is recorded from the inside of the brain (e.g., Electrocorticography (ECoG)) or from the scalp surface of the brain (e.g., EEG). These signals are amplified, digitized, and then processed to extract specific signal features (e.g., amplitudes of evoked potentials) that encode the user's intent. These features are translated into commands that operate a computer display or other device.
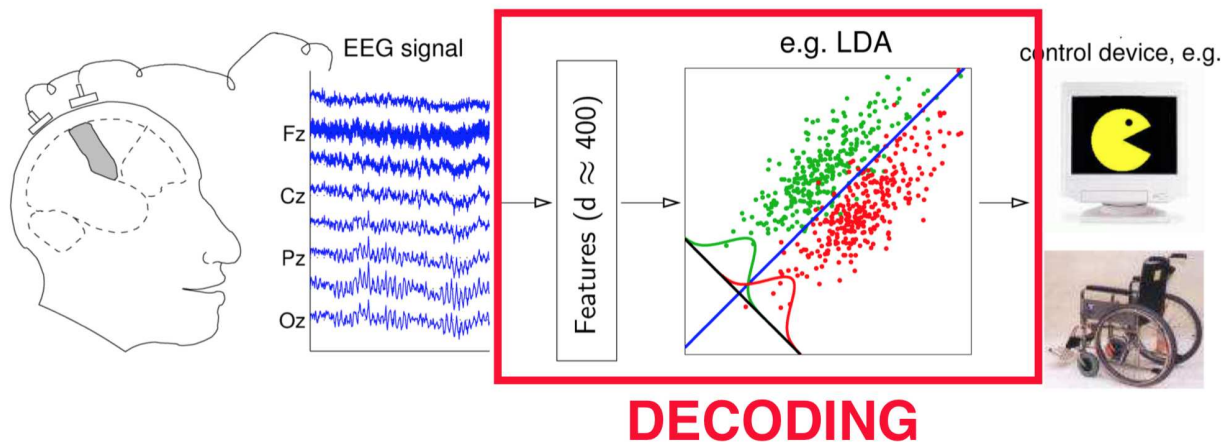
Figure 1.1: Elements of any BCI system and their principal interactions [7]. The signal is first acquired from the user's brain and then processed to extract specific features used for classification. The classification algorithms then attempt to identify the user's mental state which is translated into commands that operate an external device.

EEG-based BCI approach has provided paralyzed or 'locked in' patients alternative ways to communicate with the external world [8]. However, there are a number of challenges that must be considered when developing EEG-based BCI systems. Current EEG-based BCIs have limited communication capacity. They have maximum information transfer rates (ITRs) up to 10-25 bits $\min^{-1}$ [2, 8]. With this limitation of the transfer rates, EEG-based BCIs cannot provide those with severe neuromuscular disabilities with more complex BCI applications such as operating a multi-degree of freedom neuroprosthesis.

Furthermore, EEG signals have good temporal resolution with delays in the tens of milliseconds, but low spatial resolution on the scalp surface due to the blurring effects of different conductivities of the volume conductor such as cerebrospinal fluid, skull, skin, and many other layers.

The EEG also is susceptible to physiological artifacts due to muscle contractions, ocular movements and heart activity, or technical artifacts such as power-line noises or changes in electrode impedances. These artifacts may reduce the performance of EEG-based BCI systems.

Spatial resolution and the ITRs are not the only challenges facing EEG-based BCI systems, but there are other scientific and technical challenges. Some of these challenges are discussed in the following points.

Challenge 1: BCI research is inherently and necessarily dependent on very fundamentally multidisciplinary research such as neuroscience, engineering, cognitive science, computer science, and other technical and health-care disciplines.

Challenge 2: The brain is highly non-stationary, which means that the EEG signals rapidly vary over time and over sessions. Therefore, non-stationary signal processing and machine learning algorithms need to be developed.

Challenge 3: EEG has a very low signal-to-noise ratio (SNR). In other words, the relevant brain activity is small compared to brain background activity. Therefore, it is hard to detect relevant brain patterns.

Challenge 4: There is a high variability in the EEG signals recorded between subjects or even within sessions for the same subject. This would result in poor classifications and high error rate.

Challenge 5: The information transfer rate (ITR) achievable through EEG is low compared to the ITR observed by invasive methods [9]. Many communication and control BCI systems, such as neuroprosthesis control, require high ITRs. Low ITR makes the BCI applications suffer from accurate communication and control.

Challenge 6: The BCI system must have sufficient reliability to be practical and useful, especially in the clinical applications. Low reliability of current BCI systems is mainly due to the incorrect recognition of user intent by the BCI. This poor recognition by BCI is probably because it is difficult for the user to reliably perform the mental tasks or because the translation algorithm, which translates the EEG signals into device commands, does not work perfectly.

Challenge 7: User training is considered as one of the most important factors affecting the BCI

capabilities. In some BCI experiments such as motor imagery tasks, it is difficult to train the users to control their brain signals. In addition, some users may need more training time to achieve high performance. Therefore, providing appropriate feedback makes subjects more motivated and involved.

Despite these well-known shortcomings, numerous studies have successfully demonstrated practical EEG-based BCI applications for those with devastating neuromuscular disorders. For instance, Li, et al., [10] have proposed an EEG-based BCI paradigm which allows the user to control a cursor in two dimensions by combining two EEG signals: P300 potential and mu and beta rhythms during motor imagery. The subjects successfully controlled the cursor with accuracies of about 80%. Moreover, Pfurtscheller, et al., [11] have used steady-state visual evoked potentials (SSVEPs), resulting from repetitive flicker stimulation, to control a two-axis electrical hand prosthesis. In their study, the participants reached an online classification accuracy between 44% and 88%.

Due to the advancements in computational technology and machine learning, the field of BCI is progressing fast towards noninvasiveness. The most popular brain activity patterns that have been identified and used in constructing noninvasive BCI are P300 Event-Related Potential (ERP) and motor execution/imagery induced Event-Related (De)Synchronization (ERD/ERS) [12–14]. ERPs are electric brain responses time-locked to a particular external or internal event [15]. The P300 is an exogenous ERP component elicited approximately 300 ms after an infrequent, but expected, stimulus presented to a subject. A P300 speller is based on this concept, where the user attends to a grid of of letters displayed on a computer monitor. The rows and columns of the grid are flashed in a random sequence. When a row or a column that has the letter that the user wishes to type is flashed, a P300 component of the ERP is elicited [16].

The ERD/ERS BCIs based on motor real/imagined movement have been proposed to restore function and enhance communication in motor-impaired patients [17, 18]. The oscillatory activity of the EEG signals are changed when we move our left or right hand, for example. These changes are recognized in the EEG oscillation and used to drive a BCI. A typical example of the oscillatory

activity-based BCI is imagination of motor movements [19]. For example, a user might imagine moving his left/right hand, foot, or tongue to control a robotic arm [20]. The ERD/ERS appears during movement or preparation for movement as a power decrease or increase in μ (8-13 Hz) or β (16-32 Hz) bands observed in the contralateral motor cortex. These phenomena reveal the change of synchrony in underlying neuron populations in the motor area of the brain [13]. A variety of studies have demonstrated that healthy people or motor-impaired patients can learn to control the amplitude of μ or β rhythms detected from the sensory motor areas with EEG electrodes attached to the scalp. This can then be used to allow people with severe motor disabilities to control applications such as a robotic arm or a neuroprosthesis [21].

1.1 Overview of the Problem

The problem of decoding information from neurons is extremely important in the field of brain-computer interfacing and neural prosthesis. A common approach to design a BCI system is to decode kinematic parameters of movements. Several studies have demonstrated the decoding of the movements of large body parts of the human using ECoG and EEG, including wrists, upper limbs, elbows and shoulders [22–24]. However, there are some difficulties in decoding movements of fine body parts, such as individual finger using EEG recordings. Although it has been shown that individual finger movements can be accurately decoded using ECoG signals, it is hard to reach good performance using noninvasive EEG [25, 26].

Decoding individual finger movements has not been well-studied in EEG based BCI because it is still a challenging task [27, 28]. As mentioned previously, the EEG has poor spatial resolution and low SNR. These two disadvantages of the EEG make the decoding of individual finger movements hard since the finger movements activate adjacent brain regions and elicit close cortical motor areas [29]. Current noninvasive approaches of decoding finger movements from the brain use conventional disc EEG electrodes. Using the disc EEG electrodes is not promising to reach high reliability in recognizing patterns in EEG related to individual finger movements since they

lack the precision necessary to discern differences in brain activity. Therefore, this decreases the BCI's usability and convenience.

To the best of our knowledge, very few studies have shown that the kinematics of fine individual finger movements can be decoded from brain signals. All of these studies have shown that EEGs may contain information about the movements of fine body parts, such as individual finger, which can be used and translated into control signals to control external devices. This movement-related information has to be extracted from EEG signals reliably. With the current conventional disc EEG electrodes, the step of extracting movement-related information is not promising, especially if the temporal EEG is used as features.

Different features related to motor functions have been extracted as control features for BCI, such as ERD/ERS. However, we still do not know which feature works best for decoding different finger movements. In addition, there are many different ways in which the finger can be moved, such as tapping, extension or flexion, rapid or slow movements. Moreover, internally generated and externally triggered finger movements, i.e., during the absence and presence of an external cue, generates different movement-related potentials known as Bereitschafispotential and contingent negative variations, respectively [30, 31]. All of these different movement types and experimental protocols make it hard to study which ones should be chosen to design a more practical and reliable EEG-based BCI, such as neuroprosthetic device.

1.2   The Dissertation Objective

EEG-based BCI research has matured much in the last several decades. In the last two decades, there has been growing interest in developing new methods to achieve higher quality EEG signals, and therefore better estimates of cognitive state information. One of these methods is by developing new electrodes with higher capabilities than the current conventional disc electrodes which have not changed much in decades.

Recently, new electrodes, tri-polar concentric ring electrodes (TCREs), were developed by Dr. W. Besio, at the University of Rhode Island [32]. These TCREs have been proven to have several

advantages compared to conventional disc electrodes, such as better spatial resolution and higher signal to noise ratio. The design of the TCREs automatically cancels the noise and reduces mutual information between electrodes [33, 34]. In addition, the TCREs estimate the surface Laplacian and therefore increase the spatial resolution of the EEG signals.

The objective of this research is to use the neural signals generated during real and imaginary finger movement to discriminate between the five fingers. In this study, we investigated the hypothesis that brain signals recorded non-invasively through scalp EEG can be used to decode fine finger movements. We also evaluated the performance of decoding real and imaginary finger movements with EEG signals recorded from the TCREs and conventional disc electrodes. In this study, we focused on recording and analyzing the contingent negative variation (CNV) movement-related potentials (MRPs) [35]. We focused on this type of MRPs because we wanted to make a comparison between all the subjects. In order to do that, we need the movement to be performed at the same time window, and this can be done by presenting a cue to the subjects so they know when they should start moving their finger. This paradigm will generate the CNV.

Also, we compared temporal and spectral features from EEG signals recorded by tri-polar and disc electrode systems after finger movement onset. Previous study has shown that the temporal features computed from the MRP recorded by conventional disc electrodes may not suffice for the task of decoding movements of fine body parts, that is, individual finger movements [36]. This is due to the fact that the conventional disc electrodes detect the same signal when they are placed closer than 4 cm. However, we hypothesized that the TCREs provide higher spatial resolution than the conventional disc electrodes needed to distinguish and identify brain activity and spatiotemporal patterns related individual finger movements.

We suspected the combination of the TCREs and machine learning algorithms will lead to a practical, reliable, and accurate BCI for controlling a neuroprosthesis. The choice of the best machine learning algorithm leads to design a practical, accurate BCI application. For this reason, we compared decoding classification performance of different classification algorithms including linear discriminant analysis and artificial neural networks. Since the TCREs automatically apply

7

the Laplacian to the EEG signals, we hypothesized that using TCREs will discriminate between finger movements better that the conventional disc electrodes. This hypothesis is based on previous studies that have shown that applying Laplacian to EEG signals yields good performance on EEG classification [37, 38].

Determining the finger movement time onset precisely is critical in analyzing MRPs. The conventional way of doing that is by recording EMG activity simultaneously with EEG. The synchronization of EEG signals and EMG activity requires additional signal processing for both data and more equipments (e.g., amplifiers, electrodes, etc.). Additionally, the type of devices used to run the experiment might be not sufficient to collect EEG and EMG data simultaneously. For instance, in this study we used Cyton OpenBCI board, which has only eight input channels, to measure and record EEG data. All the input channels were connected to TCREs and the output of the outer rings, which means there was no any available input channel to be used by EMG electrode. Here we designed a new method for detecting the finger movement onset precisely by using accelerometer and Arduino board. More details is in Section 3.2.

1.3 Overview of Dissertation

The dissertation is organized as follows. Chapter 2 gives background information about the classification algorithms used in this study, the TCREs, and MRPs. The related works in decoding finger movements are discussed in the last section of this chapter. Chapter 3 explains in details the experimental protocol and data acquisition. In addition, a new method of detecting finger movement time onset is discussed in this chapter. Chapter 4 discusses the results that have been achieved for different finger movement classification using TCREs and disc electrodes. Chapter 5 gives the conclusion to the study and outlines the future work. Appendix lists the code used in this research.

Chapter 2

Background and Related Works

This chapter explains the basic information relating to our work. The first section of this chapter introduces two classification algorithms, Linear Discriminate Analysis and Artificial Neural Networks, which were used in this research to classify individual finger movements from EEG recordings. The second section introduces the tri-polar concentric ring electrodes. The main two types of the MRPs which are Bereitschaftspotential and contingent negative variations are discussed in the third part of this chapter. The related works that have been achieved in the decoding of finger movements is summarized in the last section.

2.1   Classification Algorithms

Classification algorithms are methods of supervised learning that aim to estimate the class of data as represented by a feature vector. In this study, our goal of classification is to classify the data into different classes. For instance, classifying the data into movement and resting conditions or classifying the data based on the finger movement. To accomplish the task of classification, we will use two different classifier techniques that are well-studied to classify different movement tasks [39]. These classifier techniques are linear discriminant analysis (LDA) and artificial neural networks (ANNs).

2.1.1   Linear Discriminant Analysis

Linear Discriminant Analysis (LDA), also called Fisher's LDA, is used in machine learning (ML) to find a linear combination of features that separate two or more classes of objects. The goal of a discriminant function is to take an input vector x and assign it to one of K discrete classes, denoted C_k, where $k = 1, 2, ..., K$. Suppose we have an input vector x together with a corresponding vector t of target variables, and the goal is to predict t give a new value for x. The joint probability $p(x, t)$ provides a complete summary of the uncertainty associated with these

variables [40]. Using Bayes' Theorem, these probabilities can be expressed in the form:

$$P(C_k|x) = \frac{P(x|C_x)P(C_k)}{P(x)} \qquad (2.1)$$

Let us assume that all classes share the same covariance matrix Σ. By testing if the probability that a sample x is contained in one class or another, we can find the discriminant function:

$$\delta_k(x) = x^T\Sigma^{-1}\mu_k - \frac{1}{2}\mu_k^T\Sigma^{-1}\mu_k + \log P(C = k) \qquad (2.2)$$

where μ_k is the mean of class k, $P(C = k) = \frac{N_k}{N}$, and N is the total number of samples from all classes. This approach tells us that the class of x is argmax $\delta_k(x)$. Since equation 2.2 is linear in x, it can be written as:

$$\delta_k(x) = x^T w_k + x_o \qquad (2.3)$$

where w_k is weight vectors, and x_o is a bias. Consider we have two classes, C_1 and C_2. If $\delta_k(x) \geq 0$, the input vector w is assigned to class C_1 and to C_2 otherwise. The decision boundary is defined by the relation $\delta_k(x)$.

2.1.2 Artificial Neural Networks

The artificial neural network "ANN", sometimes is called neural network "NN", is an information processing paradigm that is inspired by the way biological nervous systems, such as the brain, process information. The key element of this paradigm is the novel structure of the information processing system. It is composed of a large number of highly interconnected processing elements (neurons) working in unison to solve specific problems. The ANN is configured for a specific application, such as linear/nonlinear regression, pattern recognition or data classification, through a learning process. Learning in biological systems involves adjustments to the synaptic connections that exist between the neurons [40].

The commonest type of ANNs consists of three groups, or layers, of units: a layer of "input" units is connected to layers of "hidden" units, which is connected to a layer of "output" units.

The activity of the input units represents the raw information that is fed into the network. The purpose of the hidden units is determined by the activities of the input units and the weights on the connections between the input and the hidden units. The number of units in the hidden layers can vary from no hidden layer to n hidden layers. Each layer has a set of weights associated with the inputs to hidden layer. These layers apply a nonlinear function to the weighted sum of inputs. The first hidden layer operates on the input values, while subsequent layers operated on the outputs of the previous hidden layer. At the end, the behavior of the output units depends on the activity of the hidden units and the weights between the hidden and output units. The output layer produces a weighted sum of the outputs from the last hidden layer as the output of the neural network. The neural network learns the weights through an iterative process using training data. Figure 2.1 shows an example of simple ANN structure.
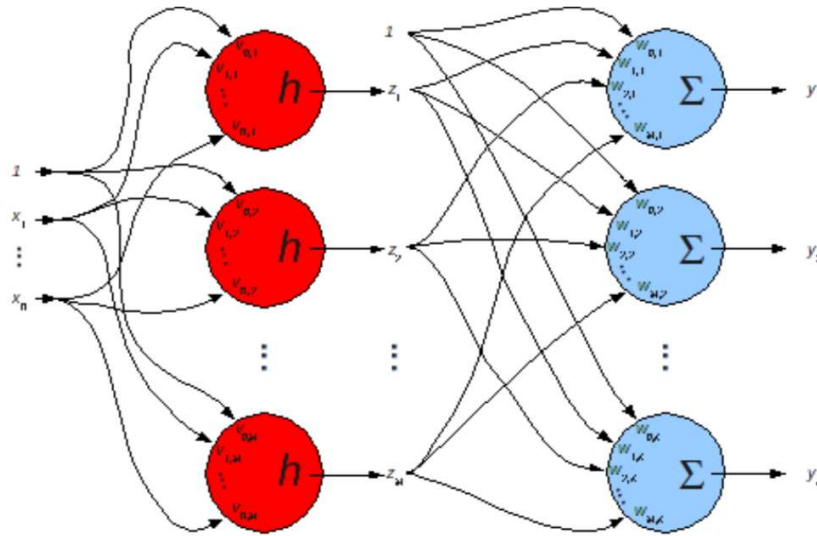
Figure 2.1: A Simple of Neural Network Representation [41].

The following equation computes the value of the predicted output Y for a given set of X as inputs in a two layers, which are hidden and output layer, neural network [41]:

$$Y = h(XV)W \tag{2.4}$$

11

where h is the activation function for the units in the hidden layer. In addition, V and W are weights associated with the hidden and output layers. In general, gradient descent (GD) is used to optimize the weights of the neural network. Before using this method, the mean squared error between each target value and the $t_{n,k}$ and output value $y_{n,k}$ is needed to be calculated by the following equation [41]:

$$E = \frac{1}{N}\frac{1}{K}\sum_{n=1}^{N}\sum_{k=1}^{K}(y_{n,k} - t_{n,k})^2 \qquad (2.5)$$

The neural network model then learns by the training the values of the weights for the hidden V and output W layers. This process is done by minimizing the mean squared error E between the values predicted Y and the target values T associated with the training data. Moreover, the neural network model also uses gradients of the mean squared error E to improve the weights. The gradient of mean square error is used to make small changes into the weights $v_{j,m}$ and $w_{m,k}$ [41].

$$v_{j,m} \leftarrow v_{j,m} - \rho_h \frac{\partial E}{\partial v_{j,m}} \qquad (2.6)$$

$$w_{m,k} \leftarrow w_{m,k} - \rho_o \frac{\partial E}{\partial w_{m,k}} \qquad (2.7)$$

where ρ_h is the learning rate of the hidden layer, and ρ_o is the learning rate of the output layer.

If the NN is used to solve a multi-class classification problem, the output layer uses a $softmax$ function. By using the $softmax$ function, we are forcing the output of the neural network to sum to one, so that they can represent a probability distribution across discrete mutually exclusive alternatives [40]. The output of $softmax$ is the probability of each class and the target class will have the high probability. The $softmax$ function is defined as:

$$Y(x)_j = \frac{e^{x_j}}{\sum_{k=1}^{K} e^{x_k}} \qquad (2.8)$$

where x_j is the weighted sum of output unit j, and $j = 1, 2, ..., K$.

2.2   Tri-polar Concentric Ring Electrodes

In 1924, Hans Berger recorded the first human electroencephalogram (EEG) using conventional disc electrodes [42]. Since that time, the basics of the EEG measurement have been the same even though the conventional electrodes have many shortcomings. Beside the poor spatial resolution provided by disc electrodes, the EEG signals recorded with conventional disc electrodes have reference electrode problems. The choice of the reference electrode for the measurement of EEG is a critical issue since there is no ideal location for it. Therefore, placing the reference electrode at different locations provides EEG signals with different characteristics [32, 43].

There is a need for new electrodes that may be utilized to overcome the current disadvantages of the conventional disc electrodes. There has been little effort on improving the conventional disc electrodes. Recently, tri-polar concentric ring electrodes (TCREs) were invented by Dr. W. Besio. The TCRE has the same size as the conventional disc electrode. However, it consists of three electrode elements: the outer ring, the middle ring, and the center disc, as shown in Figure 2.2(B). The potential differences are taken between the outer ring and the central disc and between the middle ring and the central disc.
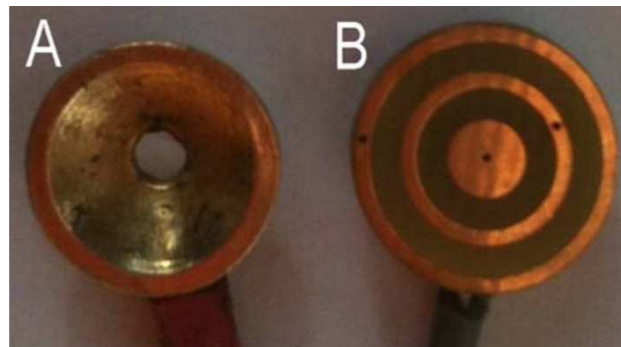
Figure 2.2: Conventional disc electrode (A) and tri-polar concentric ring electrode (B).

The TCRE estimates the surface Laplacian (SL) based on a nine point finite difference method (NPM) automatically and better than the conventional disc electrodes. The SL, also known in the literature as current source density or current scalp density (CSD), is one of the spatial filters that is commonly used in EEG data to clean the data and prepare it for connectivity analysis. Laplacian

attenuates the volume conduction by minimizing contributions of deep and distant sources, and estimates current flow at the dura.

The spline surface tri-polar estimation relies on the potential recorded on every electrode to optimize the interpolation parameters, therefore more sensors lead to a better estimation of the parameters. On the other hand, each TCRE measures the surface Laplacian independently, and as a result, the tri-polar surface Laplacian does not rely on the number of sensors. The TCRE performs the Laplacian automatically and takes bipolar differences of the surface potentials from closely spaced ($\sim$1 mm) concentric electrode elements.

There is a local relationship between the SL of scalp potentials and the underlying flow of electric current caused by brain activity [44]. This relationship approximates the cortical potentials from scalp voltage distributions. Laplacian is the second spatial derivative of the scalp potentials. Bin He [45] has shown that SL increases the spatial resolution and spatial selectivity of the brain activity. Several approaches have been used to estimate the SL resulting from the EEG potential measurements, such as the five-point method (FPM), spline Laplacian algorithm, ellipsoidal spline Laplacian algorithm, and realistic geometry Laplacian algorithms [46–49].
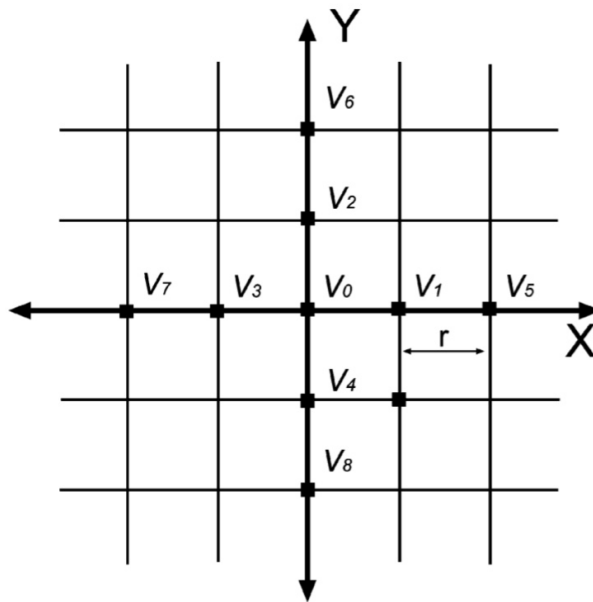
Figure 2.3: Arrangement of the five-point method (FPM) and nine-point method (NPM). v_o through v_8 are the potentials at points p_o through p_8, respectively.

14

The five-point method (FPM) was first reported by Hjorth to increase the EEG spatial selectivity using conventional disc electrodes [46]. Hjorth's five point method calculates the local surface Laplacian by taking the difference of the potential on the electrode and the average potential on its neighboring four electrodes. In the 10-20 system configuration, electrodes that are often used are not close to each other. Hence, the surface Laplacian might not be estimated correctly. Instead of utilizing nearby electrodes to estimate the surface Laplacian, the three elements of a single TCRE are used to calculate the surface Laplacian. As shown in Figure 2.3, v_5, v_6, v_7, v_8, and v_o form the FPM.

The Laplacian potentials at point p_o are calculated as:

$$\Delta v_o = \frac{\partial^2 v}{\partial x^2} + \frac{\partial^2 v}{\partial y^2} = \frac{1}{(2r)^2}(\sum_{i=5}^{8} v_i - 4v_o) + O((2r)^2) \tag{2.9}$$

where r is the interpoint distance and the truncation error is given as:

$$O((2r)^2) = \frac{(2r)^2}{4!}(\frac{\partial^4 v}{\partial x^4} + \frac{\partial^4 v}{\partial y^4}) + \frac{(2r)^4}{6!}(\frac{\partial^6 v}{\partial x^6} + \frac{\partial^6 v}{\partial y^6}) + ... \tag{2.10}$$

After neglecting the truncation error and solving 2.9, we get the approximation to the Laplacian at p_o as [50, 51]:

$$\Delta v_o \cong \frac{4}{(2r)^2}(\overline{v} - v_o) \tag{2.11}$$

where $\overline{v}$ is the average of the potentials v_5, v_6, v_7, and v_8.

The TCREs are based upon the nine-point method (NPM). As shown in Figure 2.3, v_o through v_8 form the NPM (which can be seen also as two FPM). The Laplacian potentials at point p_o are calculated as:

$$\Delta v_o = (\frac{\partial^2 v}{\partial x^2} + \frac{\partial^2 v}{\partial y^2}) = \frac{1}{12r^2}\left\{ 16\sum_{i=1}^{4} v_i - 60v_o - \sum_{j=5}^{8} v_j \right\} + O(r^4) \tag{2.12}$$

where the truncation error is given as:

$$O(r^4) = (\frac{r^4}{270})((\frac{\partial^6 v}{\partial x^6}) + (\frac{\partial^6 v}{\partial y^6})) + ...$$ (2.13)

If we compare equations 2.10 and 2.13, we find that the NPM truncation error does not have the 4th order derivative term. Therefore, the NPM is more accurate than the FPM. By applying a similar procedure, we can generalize the FPM to a TCRE. Hence, the average potential on the middle ring and outer ring, respectively, is given as:

$$\Delta v_o \cong \frac{1}{3r^2} \left\{ 16(\frac{1}{2\pi} \int_0^{2\pi} v(r, \theta)d\theta - v_o) - (\frac{1}{2\pi} \int_0^{2\pi} v(2r, \theta)d\theta - v_o) \right\}$$ (2.14)

Previous studies in a wide range of applications have demonstrated the superiority of the TCREs to conventional disc electrodes. Besio, et al., [33] used the TCREs to measure the surface Laplacian electrocardiogram (LECG). They compared the accuracy in estimating the SL and the spatial resolution with the concentric bipolar, concentric quasi-bipolar and disc electrode configurations. They found that the TCREs configuration results in higher accuracy and spatial resolution over other electrodes configurations.

In another study, the EEG signals were acquired using TCREs and disc electrodes while the subjects performed left/right hand motor imagery [52]. The purpose of their work was to compare the classification of left/right hand imagery movements between signals from disc and tri-polar electrodes. They used a Mahalanobis distance based linear classifier for classification, and an autoregressive (AR) model for feature extraction [53,54]. For each subject, 160-200 trials for both left and right hand imagery movements were recorded. The average accuracy for the subjects from TCREs and disc electrodes were $78.7 \pm 3.3\%$ and $68.0 \pm 5.0\%$, respectively.

TCREs can also be used to provide more precise stimulation. Besio, et al., [55] applied non-invasive transcutaneous electrical stimulation (TcES) via TCREs on the scalp of rats after inducing seizures with penicillin G, pilocarpine, and pentylenetetrazole (PTZ). The results showed that the seizures induced by PTZ were attenuated significantly after applying the TcES via TCREs. They also found that TcES via TCREs attenuated the severity of behavior induced by seizures such

16

as motor contractions. However, when they applied the electrical stimulation via conventional electrodes, the rats had vocalizations, escape behavior, and uncontrollable motor activity.

Liu, et al., [56] used a computer simulation, by Cuffin and Cohen [57], to compare the spatial resolution for disc electrodes and TCREs. The simulation was based on 4-layer concentric spherical human head model. The four layers represent brain, cerebrospinal fluid, skull, and scalp. They placed an 8x8 electrode array above the visual cortex area. To generate visual evoked potentials (VEPs), they placed a signal dipole under the electrode array. They recorded the VEPs with two electrodes configurations and found that the half sensitivity volume (HSV) of TCRE is 1/10 the HSV of the disc electrodes. The HSV is defined by Malmivuo and Suihko [58] as "the volume of the source region in which the magnitude of the detector's sensitivity is more than one half of its maximum value in the source region" and it is inversely proportional to the spatial resolution. Therefore, higher spatial resolution is achievable with TCREs.

The TCREs also can be used to detect high frequency oscillations (HFOs) preceding seizures from patients with epilepsy, which improves diagnosis epilepsy and localization of seizure onset. Besio, et al., [59] recorded EEG signals with TCREs and disc electrodes from patients with epilepsy at the same time. High-gamma band (between 60 and 80 Hz) was observed in TCREs EEG data with less muscle and movements artifacts starting approximately 10 min prior to the seizure activity, but not in the conventional EEG data. In another patient, 70 Hz gamma band was found approximately three minutes before the seizures.

Boudria, et al., [60] compared disc EEG with tri-polar EEG based BCIs for real-time one-dimensional cursor control. The subjects were asked to move a cursor (imaginary movement) from the center of the screen and hit a target that presented in the left or the right of the screen. The subjects performed 10 runs in which each run contained 20 trials. The accuracy for each subject was calculated for disc and tri-polar electrode. The subjects achieved higher average accuracies with the tri-polar EEG (between 30-66% for disc EEG, and between 44-100% for tri-polar EEG).

Another comparative study between the tri-polar and disc electrodes was done by Koka and Besio [34]. In their work, they compared the SNR, spatial selectivity, and mutual information (MI)

17

of the movement-related potentials (MRPs) signals recorded using tri-polar, bipolar, and unipolar electrode systems. The MRP is a negative EEG deflection preceding and accompanying self-paced voluntary real and imaginary movements [35]. The subjects were asked to press a micro-switch when a cue is presented. The results showed that the averaged SNR for disc, bipolar, and tri-polar electrodes were 1.454, 2.829, and 5.431, respectively. The results also showed that the TCREs have significantly higher spatial selectivity and MI than disc and bipolar electrodes.

2.3   Movement-Related Potentials

In present-day EEG-based BCIs, movement-related potential (MRP) has received much attention. The MRP is a low-frequency negative shift in the EEG recording that takes place about 2 seconds prior to voluntary movement production. The MRP is present in real as well as in imaginary volitional movements [1]. The MRPs are observed in self-paced and cue-based paradigms. The former is often referred to Bereitschaftspotential potential (BP) and the latter is called contingent negative variation (CNV). The MRP comprises three events called BP or readiness potential (RP), motor potential (MP), and movement-monitoring potential (MMP). An example of MRP and its components is presented in Figure 2.4.

The following two subsections give an overview of two types of movements related potentials: Bereitschaftspotential and contingent negative variation. We narrow the focus down to the main components and the source generators for each type. Moreover, Sections 2.3.1 and 2.3.2 describe the similarity and difference between BP and CNV.

2.3.1   Bereitschaftspotential

The Bereitschaftspotential (BP, which means "readiness potential" in German) was first described by Kornuber and Deecke in 1964 [62]. It is a negative potential which commences 1 to 2 s prior to the planning of voluntary movement onset. BP has two distinguishable components. The first component starts about 2 s before to movement onset, known as early BP or BP1, and is more distinguished in the supplementary motor area (SMA) and the cingulate motor area (CMA).
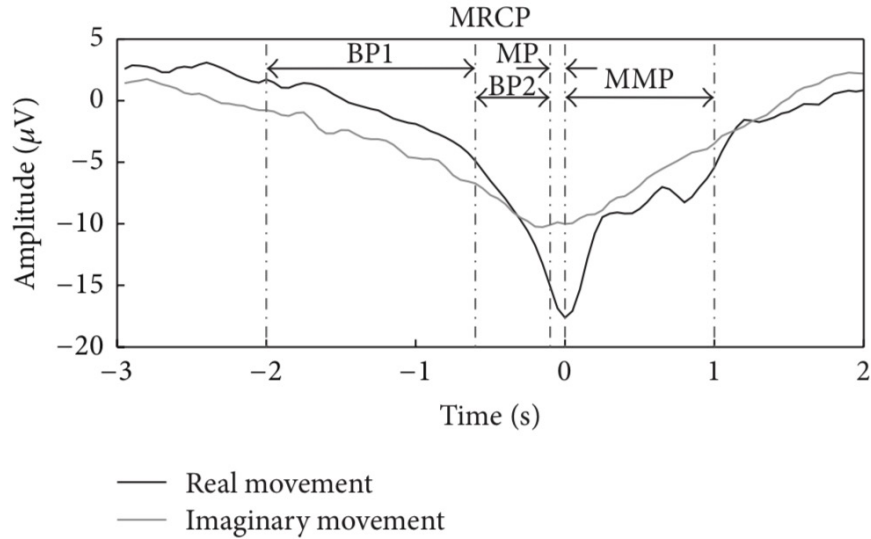
Figure 2.4: MRPs for real and imaginary right ankle dorsiflexion movements. Time 0s is defined as the movement onset. BP1 and BP2 are early BP and late BP, respectively. MP is motor potential, and MMP is movement-monitoring potential [61].

The second component, known as late BP or BP2, has a steeper slope and occurs about 0.4-0.5 s prior movement onset and has maximum amplitude over the contralateral primary motor cortex. It is believed that BP1 may represent the more general preparation for the forthcoming movement or reflect an intention to act [1].

The generator sources of the BP are still unclear. Based on the results of invasive recording in epileptic patients, the source generators of the BP in human are thought to be primary and supplementary motor areas (SMA) [63]. An intracranial recording study showed that the BP might be recorded from basal ganglia and thalamus [1]. Another study reported that the BP was produced by both the ipsilateral and contralateral supplementary motor areas (SMAs) [64]. There are various factors influencing the magnitude and time course of BP. Table 2.1 shows some factors which influence the early and late BP components. More details on BP can be found in the comprehensive book "The Bereitschaftspotential-Movement Related Cortical Potentials" [35].

2.3.2   Contingent Negative Variation

The contingent negative variation (CNV), also known as movement-preceding negativity (MPN), was first described by Walter et al., in 1964 [65]. It is a negative brain potential that occurs in the

Table 2.1: Some factors which influence the magnitude and time course of early and late BP [1].

Factors	Early BP	Late BP
Level of intention	Larger	
Preparatory state	Earlier onset	
Movement selection	Larger	No effect
Speed	Later onset	
Mirror movement	No change	Involved
Complexity	No effect	Larger
Precision	No effect	Larger

interval between a "Warning" (S1) and a "Go" (S2) stimulus (Figure 2.5). The CNVs are produced with the planning and execution of externally-paced, voluntary movements. Similar to the BP, the CNV has two main components: early and late CNVs. The early CNV begins immediately after S1 and has maximum amplitude over the frontal cortex. The late CNV starts about 1.5 s before the "Go" cue stimulus and has maximum amplitude over the motor cortex.

Several studies have investigated whether the late BP and late CNV components are identical or not. Rohrbaugh et al., found that the late CNV may share some generator mechanisms with BP [66]. Another work [67] found that the late CNV has larger amplitude as compared with BP. Recent study suggests that the generators of the late CNV component are in the premotor cortex, while the late BP is generated in the supplementary motor area [68]. Deecke and Komhuber found that the CNV is larger over the frontal area, and the BP over the parietal areas [62]. Also, they found that the CNV increases suddenly, while the BP increases gradually. In contrast, various studies reported that the late BP and late CNV components are identical. For instance, McAdam et aI., found that late CNV during larger forepreriods had a similar morphology as the late BP [69].

2.4 Related Works in Decoding Finger Movements

Numerous studies over the past seven decades have shown that the neural activities in the motor cortices recorded invasively or non-invasively provide specific movement information capable of controlling an output device. In 1951, Bates used a photographic superimposition technique to record a cerebral potential during voluntary hand movements [71]. He found a negative potential
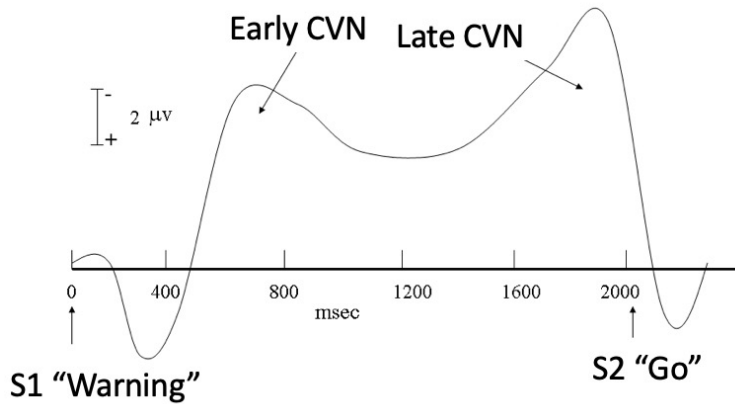
Figure 2.5: Example of contingent negative variation with early and late CNVs [70].

starting 20–40 msec after the onset of the EMG, but no potential change was found preceding the movement. Kornhuber and Deecke were the first who discovered a potential preceding voluntary movements in 1965 [62]. They found a slowly increasing surface negative potential of 10–15 μV preceding a voluntary hand and foot movement.

Since the findings of Kornhuber and Deecke, there has been a surge of interest in brain activity associated with the movement of large body parts, e.g., upper and lower limbs. For instance, Pistohl, et al., predicted movement trajectories of 2D hand position from the ECoG signals recorded during arm movements [72]. In another MEG study, Wang, et al., decoded intended of wrist movement from MEG signals [73]. Moreover, Zhou, et al., investigated the classification of shoulder versus elbow movement using EEG recordings [24].

The decoding of fine body parts, such as individual fingers, was also investigated using different neuroimaging modalities. However, the ability to decode information about fine body movements from EEG has not been well demonstrated. The following subsections summarize related work that has been done in decoding finger movements from three different neural electrophysiological signals: local field potential (LFP), ECoG, and EEG.

2.3.1 DECODING FINGER MOVEMENT FROM LFP. A number of studies have demonstrated the use of LFP recorded in human and non-human primates to differentiate between different fingers movements. Baker, et al., implanted Utah electrode array (UEA) and μECoG grid into the motor cortex of a monkey [74]. The goal of the study was to perform a real-time decoding of

the monkey's finger movements. The monkey was trained to perform finger flexions and extensions of the thumb, index, and middle finger. They calculated the average LFP and μECoG spectrum across trials for a one second window. They also developed a naïve Bayes classifier algorithm to decode finger movements in real time. The results showed that the decoding performance over all finger movements in real time was 96%. The result of the averaged spectrogram for LFP indicated a difference in power in the gamma band across fingers just prior to finger flexion.

Aggarwal, et al., analyzed the LFP recorded from the primary motor cortex (M1) and dorsal (PMd) and ventral (PMv) premotor areas, while the monkeys making reach-to-grasp movements to four different objects in space [75]. The purpose of the study was to accurately decode arm, hand, and finger kinematics during movement. They used a kinematic decoder and trained it to decode hand end point position and 18 joint angles of the wrist and fingers. Using LFP from up to 16 electrodes, the finger movements were decoded and distinguished from wrist and hand movements with a 73% accuracy.

Most of the studies about the decoding of finger movements from LFP were done on monkeys and little work has been undertaken in human. One of these studies has been conducted by Litvak, et al., [76]. They recorded MEG signals and LFP, simultaneously, in a Parkinson's disease patient with bilateral deep brain stimulation electrodes in the subthalamic nucleus (STN). The recordings were performed while the subjects performed either simultaneous button press with index, middle and ring finger or index-ring-middle with either left or right hand. The authors studied the power changes around finger movements onset. They observed an ERD in α and β bands started about 1 second before the movement onset. This ERD was followed by ERS in the same frequency bands started about 2 seconds after the movement onset. The results also showed ERS in high gamma band started about 0.5 to 1.5 seconds before button press.

2.3.2 DECODING FINGER MOVEMENT FROM ECoG. Recent ECoG-based BCI studies have shown promising results in discriminating between different fingers movements. Scherer, et al., have shown that thumb and index finger movements can be discriminated from ECoG signals in both contra- and ipsilateral hand (with average accuracy of 87.8%) [77]. They also found that

ipsilateral movements induce less activity, particularly in the higher frequency ranges (> 50 Hz), compared with contralateral movements. In another study, Flamary, et al., proposed a method for finger flexions prediction from ECoG signals based on switching models base on a single hidden Markov model (HMM), which have already been successfully used for arm movement prediction on monkeys, based on micro-electrode array measures [73, 78]. The proposed model consists of two blocks. The first block estimates which finger is moving and the second block predicts the movements of all other fingers. They achieved a correlation of 0.46 between the feature extracted from the ECoG signals and the finger flexions using a linear regression.

The cortical power spectrum changes in the ECoG signals during finger movements have been investigated as well. Miller, et al., studied the broad-spectral change in the frequencies between 5-200 Hz [79]. The results showed that there is a decrease in power at lower frequencies (< 40 Hz) before the finger movement onset and a power increase at higher frequencies (> 40 Hz). Furthermore, they found distinct representations of different fingers in cortical area. However, Schieber and his colleagues have shown that there is an extensive overlap between the activated neurons with movements of different fingers [80]. In addition, Wang, et al., have observed a mixed representation between index and thumb fingers in ECoG signals [101].

The work of Samiee, et al., focused on finding the best algorithm to classify between individual finger movements using ECoG signals [81]. The authors compared three classification algorithms: Fisher Linear Discriminate (FLD), linear Support Vector Machine (SVM) and k Nearest Neighbour (kNN). They extracted different features from the data and calculated the classification accuracy for each feature. Theses features include statistical features (mean and variance), frequency transform related features (discrete sine transform (DST), discrete cosine transform and fast Fourier transform (FFT)), parametric model related features (Auto Regressive Model), and energy at different frequency bands (δ, θ, α, and β). They also used principal component analysis method for feature extraction and scatter matrix method for feature selection. The results showed that FLD has better accuracy (45%) compared to the other classifiers.

Another work, which investigated the possibility of decoding the time course of the flexion of individual fingers using ECoG signals in humans, was conducted by Kubanek,et al., [25]. The study aimed also to localize the sources of different fingers movements in the brain. The subjects were asked to flex and extend specific individual fingers in response to visual cues. 384 features were extracted using 100-ms time windows from the ECoG signals. The results showed that it is possible to accurately distinguish between different fingers movements using ECoG signals. The maximum classification accuracy between fingers was achieved 90.6%. Furthermore, the results provide strong evidence that the Local Motor Potential (LMP) and amplitudes at high gamma frequencies (> 50 Hz) over motor cortex area are associated with different changes for different fingers.

Other studies have attempted to design real-life application of ECoG BCI by detecting and classifying finger movements online. One such study tried to control individual prosthetic fingers by using high gamma responses recorded with a high-density ECoG array [26]. They performed three kinds of experiments: vibrotactile stimulation (to control sensory feedback), finger tapping (was done offline to collect training data for online finger decoder and for offline analysis), and online testing. LDA classifier was used in the study. When specific finger movement is detected, a command is sent to the prosthetic limb and the corresponding finger is flexed at fixed velocity. The authors used the 5-way individual finger classifications to evaluate the performance of the prosthetic limb control. The results showed that the individual finger prediction accuracy reached 81%. Moreover, the results indicated that the somatosensory areas were activated before movement onset.

2.2.3 DECODING FINGER MOVEMENT FROM EEG. Recent studies have shown that the EEG signals may contain information about planning and execution of real and imaginary finger movements. The study of Stankevich, et al., aimed to classify real and imaginary finger movements using EEG signals [82]. The EEG signals were recorded from 19 electrodes. They converted the recorded EEG data to current source density to reduce the effect of volume conduction on the EEG signals. They also calculated changes in EEG power using Morlet wavelet transform. A two-level

committee of classifiers based on SVM and artificial neural networks was developed and used for classification. Moreover, two features were selected for classification: the area under the curve and the curve length calculated in a sliding window. In their study, the EEG power changes during real finger movements showed an ERD in the β frequency band prior the movement onset. Similar pattern were observed in during imaginary finger movements, but less pronounced. The average accuracy of four-class classification of the imagination finger movements reached $50 \pm 7\%$ for the pair of sites F3-C3 and $46 \pm 11\%$ for the pair of sites C3-Cz.

Hayashi, et al., [83] reported the results of predicting real and imaginary finger (thumb, index, middle and little) movements through the use of EEG. They studied the feasibility of using temporal changes in frequency spectrum power of EEG signals as a feature to discriminate between fingers by LDA during right hand finger flexion-extension and motor imagery of the task. The classification accuracies were calculated for three frequency bands (α, β, and γ) as well as the combination of those bands. The results showed that the highest accuracy was 61.13% on index-middle classification in motor imagery task, while the highest accuracy was 67.39% on thumb-middle classification in motor real task. The results also suggested that using the combined features of α, β, and γ could yield significantly increased classification accuracy between fingers in both motor real and imagery tasks.

Previous studies have focused on developing and applying algorithms to enhance the spatial resolution of the EEG signals and hence increase finger classification from one hand. For instance, Cerny, et al., applied common spatial filter (CSP) on EEG signals recorded during voluntary movements of thumb and little fingers [84]. They used Hidden Markov Model-based classifier to classify between thumb and little finger flexion movements. The best classification accuracy obtained was $63.8\% \pm 4.9\%$. Additionally, the results did not show any significant improvement in the classification accuracy of CSP when compared the classification accuracy achieved by Laplacian filter ($61.9\% \pm 5.2\%$).

A few recent studies have investigated several EEG features in discriminating individual finger movements from one hand. A comparative study of three EEG features, including projections on

spectral principal components (PCs), ERD/ERS in α and β bands, and temporal data, in decoding finger movements shows that the use of the first three PCs as a feature can yield the best decoding accuracy (45.2%) among all other EEG features. Also, the results suggested that combined features could improve the discrimination of individual fingers movements.

2.5 Chapter Summary

This chapter gives background information and reviews previous work related to topic of this dissertation. The first section of this chapter introduces two classification algorithms, LDA and ANNs, which were used in this research to classify individual finger movements from EEG recordings. The classification of individual finger movements from one hand requires a good SNR. Moreover, the representations of different fingers in the sensorimotor cortex are largely overlapped, which necessitate high spatial resolution to extract reliable control signals that originate from relatively small brain regions. Conventional EEG recorded with disc electrodes has two major drawbacks including low SNR and poor spatial resolution. These shortcomings impose difficulties when using non-invasive EEG to classify individual finger movements from one hand. TCREs have been shown to have significantly better SNR and spatial resolution compared to EEG with conventional disc electrodes. This superiority to conventional disc electrodes has motivated us to use the TCREs to decode different finger movements from one hand. The second part of this chapter describe the TCREs in more details. The main two types of the MRPs, which are Bereitschaftspotential and contingent negative variations, are discussed in the third section of this chapter. The last direction of this chapter reviews the previous works in decoding finger movements using different techniques: LFP, ECoG, and EEG.

Chapter 3

Methodology

3.1   Experiment Protocol and Data Acquisition

The experimental protocol used in this study is shown in Figure 3.1. Thirteen right handed subjects (12 men, 1 woman; mean age 27.77 ± 10.05 (SD)) performed real and imaginary finger movements according to visually presented cues. The tri-polar-EEG and conventional EEG recorded from four electrodes (C_z, C_1, C_3, and C_5) were placed at different locations according to the 10-20 International Electrode Positioning System over the motor cortex, as illustrated in Figure 3.2. The reference and ground electrodes were placed on the forehead of the subject. The skin-to-electrode impedance was checked before each experiment and kept below 10 kΩ. The sampling rate was 1000 samples/sec per channel. The recording protocol was approved by the CSU Institutional Review Board (IRB), and all subjects gave their written informed consent for the study.

During the experiment, each subject was asked to perform two tasks: real and imaginary movements of the right hand fingers. The number of successful trials completed by the subjects for each finger is shown in Table 3.1. Each trial lasted for 6 seconds. The total duration of the experiment was 2 hours. A break of 2-3 minutes was introduced each 10 minutes in order to prevent fatigue. Also, the subject was instructed to avoid eye blinks, swallowing, or any unnecessary movement other than the required finger movements during the last 4 seconds of the trial. The subjects were seated comfortably in an armchair with the right arm relaxed and resting on a pillow. To record the time of movement onset, we designed an electronic circuit using accelerometer, Arduino and optocouplers, and the data was sampled at 1000 Hz.

Each trial began with a blank black screen at second 0, allowing swallowing or blinking for the subject. We did not use the first 2 seconds of each trial in any analysis. After that, a visual cue was presented for 2 seconds to tell the subject which task (real or imaginary) he/she will perform. The subject was instructed during this time window to relax and avoid any unnecessary movements.

The EEG data in this time window was used for resting condition. Next, the fingers' names were presented on the screen for 2 seconds (index, middle, ring, little, thumb) to tell the subject which finger movement must be performed. A training period was given before the recording sessions, and was continued until the subject could conduct the above tasks correctly.

Table 3.1: Number of successful trials for the real movement task.

Subjects	Index	Middle	Ring	Little	Thumb
1	44	45	42	41	45
2	46	45	45	39	44
3	43	43	43	45	45
4	39	40	45	46	39
5	46	45	46	44	44
6	40	42	42	42	44
7	45	44	46	45	45
8	43	45	45	40	39
9	44	40	46	37	42
10	46	44	43	40	44
11	45	45	42	44	44
12	46	45	44	44	43
13	45	45	43	42	44
Average	44	43.7	44	42.2	43.2
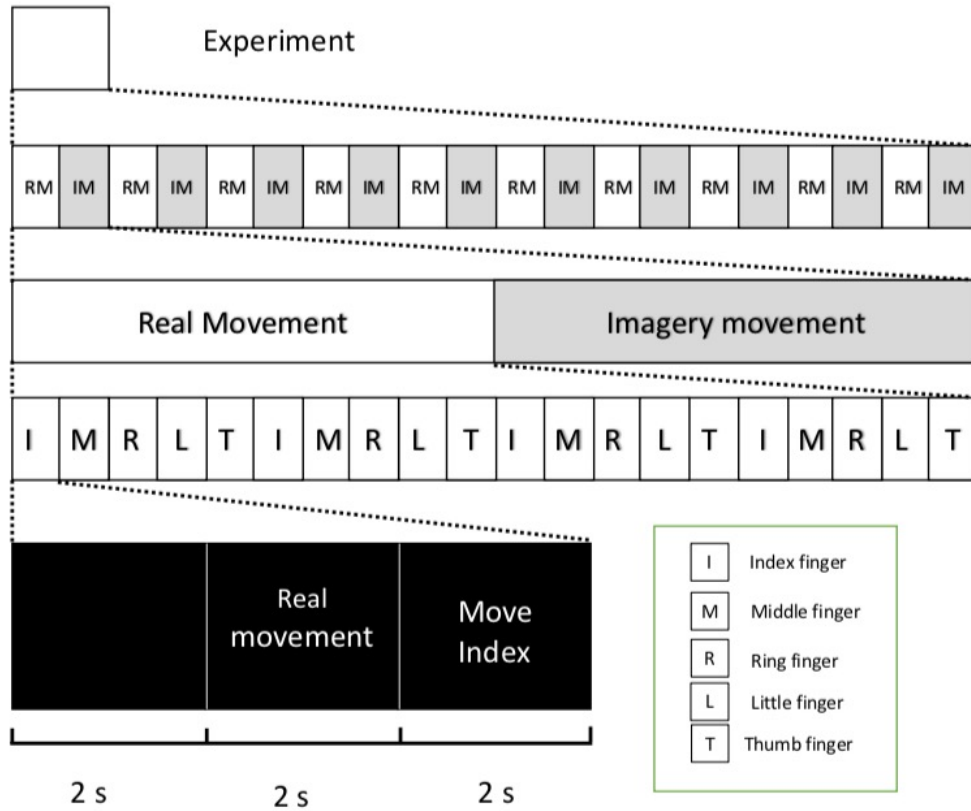
Figure 3.1: This figure illustrates the experimental protocol. The time window of each trial is 6 seconds. The first 2 seconds is blank screen where the subject can rest. The next 2 seconds will be used for resting condition. During this time window, subject will avoid any unnecessary movements. In the last 2 second, the subject will perform either real or imaginary movement of corresponding fingers according to visually presented cues.

Figure 3.2: Illustration of a 128-channel EEG sensor layout with 4 electrodes (in red) which are used in our study to decode finger movements. The upper left used to compare ipsilateral and contralateral sides. The upper right used to study only the contralateral side. The bottom used to compute the surface Laplacian on the EEG recorded with outer ring and compare it to the tEEG.

3.2 Detection of Finger Movement Time Onset

A variety of approaches have been used to detect finger movements, including datagloves, EMG, and accelerometer. Although these methods are widely used, they are limited by high cost and the need for specialist knowledge to use them. We present a new low-cost and accurate system for measuring of finger movements onset time. The following subsections discuss the components used to build the system in more details. The electrical connection between the components and how the circuit works are described in the last subsection.

3.2.1 Arduino

Arduino is a microcontroller-based open source electronic prototyping board which can be programmed with an Arduino IDE, which uses a basic version of C++. There are different types of Arduino boards such as Arduino Uno, Due, Mega, Pro Mini, etc. In this research we used Arduino Uno (Figure 3.3a) and Arduino Pro Mini (Figure 3.3b).

The Arduino Uno consists of 14–digital I/O pins (labeled "Digital 0 to 13"), where 6-pins can be used as pulse width modulation (PWM) outputs, 6–analog inputs (labeled "Analog 0 to 5"), a reset button, USB connection, and a power jack. The microcontroller used on the Uno board is ATmega328P manufactured by Atmel. ATmega328P consists of flash memory of 32KB, RAM of 2KB, CPU, and Electrically Erasable Programmable Read Only Memory (EEPROM) of 1KB. The board can be supplied with power either from the USB connector (5V), the DC power jack (7–12V), or the V_{in} pin of the board (7–12V).

The Arduino Pro Mini is similar to Arduino Uno, but smaller in size. It also consists of a 6–pin header which can be connected to an FTDI cable to provide USB power and communication to the board. The Arduino Pro Mini has only one voltage regulator that operates at 3.3V unlike the Uno which has a regulator operates at either a 5V or 3.3V. Another major difference between Pro Mini and Uno is that the Pro Mini runs at 8MHz which is the half speed of the Arduino Uno.

3.2.2 Optocoupler

Optocoupler, also known as an opto-isolator, is a passive electronic component that allows the transmission of electrical signals between two isolated circuits by using only light. A typical optocoupler is usually a 6 pin device that contains a source (emitter) of light (LED) on one side and a phototransistor on the other side, as shown in Figure 3.3c. The LED receives an electrical signal and converts it into light. The phototransistor detects the incoming light and generates electrical energy.

The optocoupler uses an LED emitter with a phototransistor that are separated by an insulating film within a silicon dome. When a current flows through the LED emitter, the light that falls on the phototransistor allows a different current to flow through the collector-emitter of the phototransistor. When no current flows through the LED emitter, there will not be a collector-emitter current.

3.2.3 LIS3DH Accelerometer

Accelerometer is a micro-electromechanical systems (MEMS) sensor measures either static (e.g., gravity) or dynamic (e.g., vibrations and movement) forces of acceleration, which is the rate of change of velocity of an object. The unit of the acceleration is meters per second squared (m/s^2) or G-forces (g), where 1 g = 9.8 m/s^2. In this research we used LIS3DH accelerometer (Figure 3.3d) produced by ST Microelectronics [85].

The LIS3DH is low power, low cost, lightweight, and easy to use triple-axis accelerometer. Additionally, LIS3DH accelerometer has 12 bit of resolution in a range of ± 2 to ± 16 g and data rate up to 5 kHz. Moreover, the LIS3DH accelerometer operates over I^2C or serial peripheral interface (SPI) digital output interface making the sensor particularly suitable for interfacing with the microcontroller.

3.2.4 OpenBCI and Wifi Shield Boards

OpenBCI stands for open-source brain-computer interface. It is an affordable and powerful tool for measuring and recording different bioelectrical signals include EEG, EMG, and ECG. There are different types of OpenBCI boards, such as Ganglion, Cyton, and Wifi shield boards. Additionally, all OpenBCI boards have an accelerometer for decoding movement. In this research we used the OpenBCI Cyton board (Figure 3.3e) and the OpenBCI Wifi shield (Figure 3.3f).

The OpenBCI Cyton board is an eight channel biosensing board with a 32–bit processor. It has PIC32MX250F128B Micrcontroller with chipKIT UDB32-MX2-DIP bootloader. The OpenBCI USB dongle is used to connect the Cyton Board to a computer. In the Cyton board, data is sampled at 250Hz. To sample the data at higher sampling rate, the OpenBCI WiFi Shield is used. The OpenBCI WiFi Shield transmits the data via Wi-Fi, as opposed to bluetooth when using Cyton, and has a ESP8266 on-board microcontroller and wireless connection which enables faster data streaming than the Cyton. The WiFi Shield can stream data at 1000Hz with the Cyton and Daisy boards and at 1600Hz with the Ganglion board.
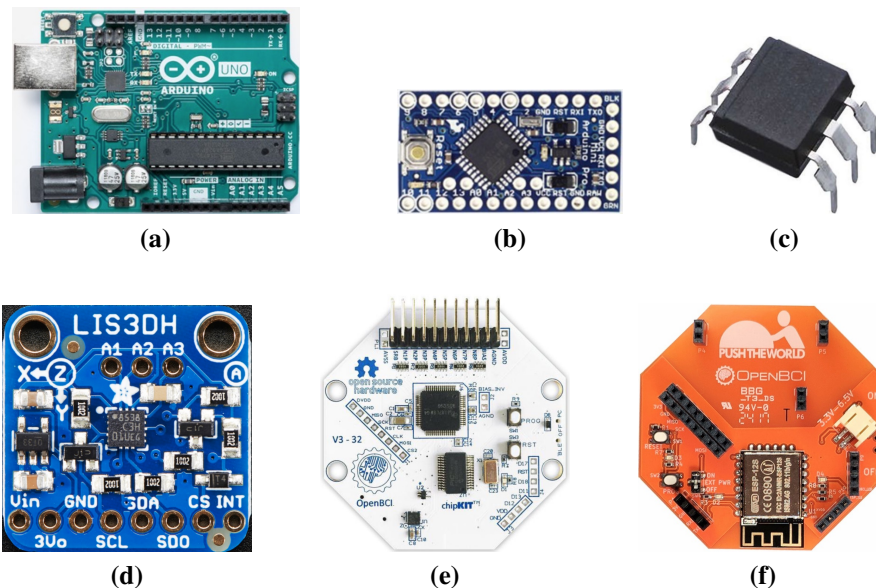

Figure 3.3: (a) Arduino Uno (b) Arduino Pro Mini (c) Optocoupler (d) LIS3DH accelerometer (e) Cyton Biosensing Board (f) OpenBCI WiFi Shield

3.2.5   Schematic Diagram of the Circuit

In this research, a real-time finger movement detecting system has been designed. Figure 3.4 illustrates the circuit schematic for the system and the connection between the components. Two screens were used. One was used to display the protocol described in Section 3.1 to the subject. The other screen was used to monitor the signals and the impedance during the recording session. Three events were detected simultaneously during the EEG recording. The first event corresponds to the warning stimulus (S1). The second event is for the "Go" stimulus (S2). The third event represents the data recorded from the accelerometer. Figure 3.5 depicts a three trials of the data and the events.

The Arduino Pro Mini is connected to a computer via FTDI USB-to-serial cable to provide USB 5V power to the Arduino board and to transfer the data between the computer and Arduino. The other side of the cable is terminated with a 6-pin connector with the following pinout: RTS, RX, TX, 5V, CTS, GND. These 6-pin headers were connected to the pins on the Arduino board. The Arduino Uno was mainly used to detect the time onset of the S1 and S2 stimulus as follows. Pyfirmata module in Python was used to write data to digital pins 3 and 5 on Arduino Uno (see the code in Appendix). When the S1 stimulus starts, the digital pin 3 goes from 0 (low) to 1 (high) state. Similarly, when S2 stimulus begins, the digital pin 5 goes from low (0) to high (1) state. The output of digital pins 3 and 5 are connected to pin 1 (anode of photodiode) on two separate optocouplers. An external 100Ω resistor was used between the Arduino and the optocoupler to drive a current of about 38 mA to the emitter side of the optocoupler ($(5V-1.2V)/100\Omega = 38mA$), where the maximum input current must be less than 60 mA according to the Optocoupler datasheet. Pin 2 on the optocoupler was connected to the ground. On the other side of the optocoupler, pin 5 receives a 3.3V from the OpenBCI wifi shield board. A resistor of $1k\Omega$ was used to limit the collector current to be less than 50mA ($(3.3V-1.2V)/1k\Omega = 2.1mA$). The ground side (pin 6) is connected to the ground of the OpenBCI wifi shield board. In addition, digital pins D11 and D12 on the OpenBCI wifi shield board are connected to pin 5 on the optocoupler.

When S1 or S2 stimulus starts, a 5V pulse is sent from the USB port to the Arduino Uno. Consequently, pin 3 or 5 switches from low to high state. When they switch from the low to high state, a current flows in the photodiode. As a result, an infrared light from the photodiode will come on and fall on the phototransistor. The phototransistor then goes into conduction mode which means that there will be a current flow between the collector and emitter of the phototransistor. Finally, the D11 or D12 on the OpenBCI wifi shield board will receive a power input from the output of the phototransistor and switches from low to high state.

The LIS3DH accelerometer is connected to the Arduino Pro Mini using I^2C wiring as follows. V_{in} pin is connected to the V_{cc} pin on the Arduino Pro Mini. The SCL pin is connected to the I2C clock SCL pin on your Arduino Pro Mini. Finally, the SDA pin is connected to the I2C data SDA pin on the Arduino Pro Mini. Digital pin 9 is set to be an output and the ground is connected to the ground on the Arduino Pro Mini. Only the value of y-axis was measured. The accelerometer is very sensitive, so a thresholding technique was used to detect the movement only when it is required. The source code used to program the accelerometer is shown in Appendix.

When the y-axis value exceeds the threshold, the pin 9 goes from low to high. A resistor of 100Ω is connected between the output of pin 9 and the input of the optocoupler (pin 1) to limit the current in the circuit. The anode of the photodiode on the optocoupler receives a voltage pulse from pin 9, and hence the photodiode emits light and an emitter-collector current flows on the phototransistor. The output of the emitter of the phototransistor is connected to pin D17 on the OpenBCI wifi shield. When the emitter-collector current flows, the D17 switched from low to high state.
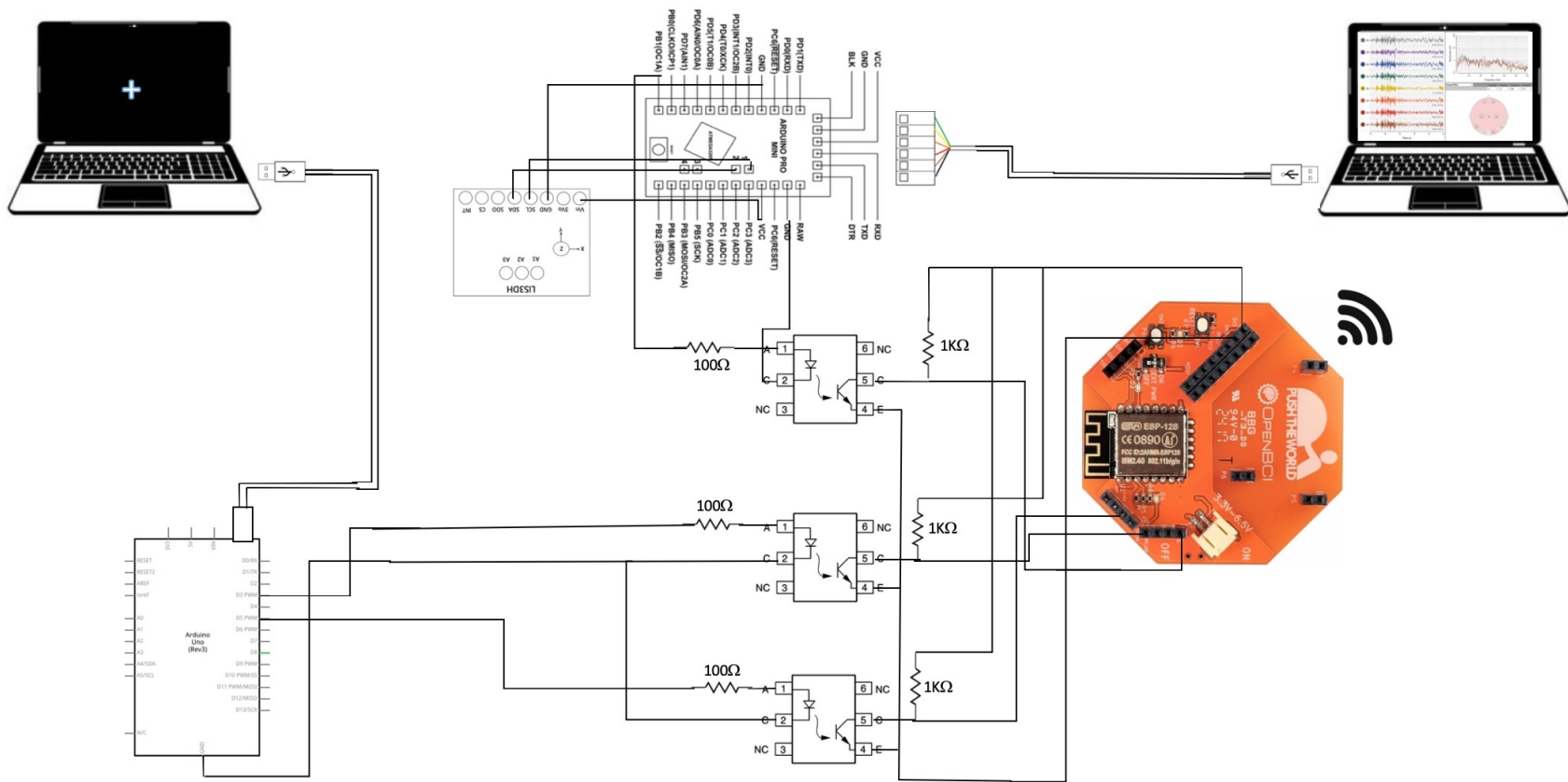
Figure 3.4: The circuit schematic for system designed for detecting finger movement onset.
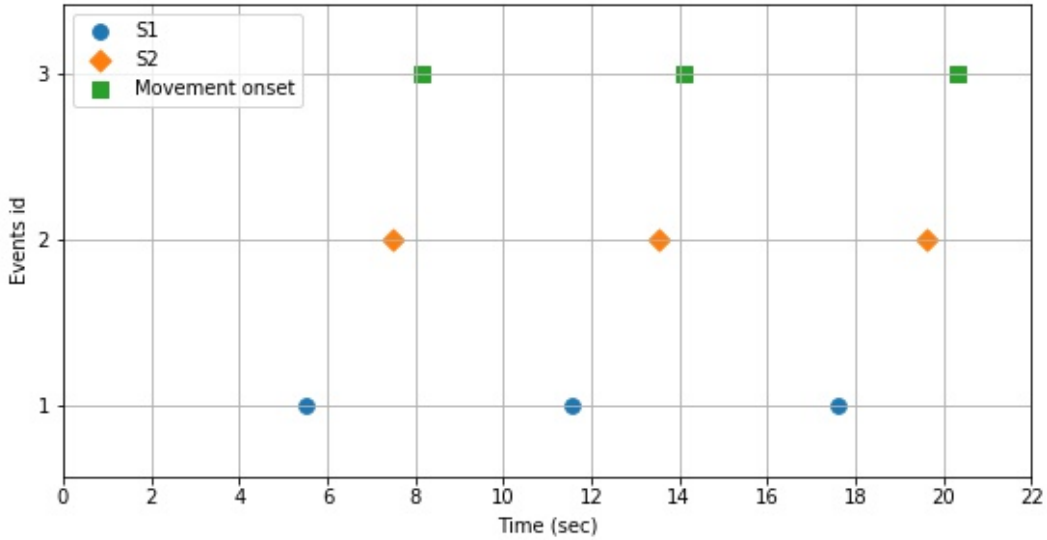
Figure 3.5: This figure shows three trials (each trial is 6 sec). Three different events can be seen. The first event corresponds to the warning stimulus (S1). The second event is for the "Go" stimulus (S2). The third event represents the data recorded from the accelerometer.

3.3 Pre-processing of MRP signals

Figure 3.6 illustrates the pipeline for processing the MRPs in this study. First, we collected tri-polar EEG and conventional EEG simultaneously using four tri-polar concentric ring electrodes [86]. After acquiring the EEG signals, a 60 Hz notch filter was applied to the data to remove the power-line noise. Then, the EEG data was passed to a high-pass filter with a cut-off frequency of 0.3 Hz. In the MRP studies, the EEG signals are usually filtered using band-pass filter from 0.3 to 30 Hz since the movement-related information is found to be in this range. However, previous studies using ECoG electrodes has shown that there are high gamma band activity generated prior and during movements [87]. In addition, it was proven that the TCREs can detect higher frequencies oscillations than the conventional disc EEG electrodes [59]. Therefore, we studied the possibility of detecting these high frequencies from the scalp using the TCREs.

The next step was to examine the data visually to see what type of artifacts are present in the data. Then, bad channels were identified and rejected. To further increase the SNR, the EEG

signals were passed to a spatial filter which is a common average reference (CAR). The CAR is calculated by subtracting the average EEG potentials of total N channels at sample point t from the potential $V(n, t)$ at channel n and that sample point. The formal equation is given as follows [37]:

$$V_{CAR}(n,t) = V(n,t) - \frac{1}{N}\sum_{i=1}^{N} V(i,t) \tag{3.1}$$

where $V_{CAR}(n, t)$ is the common average referenced potential at channel n and sample point t.

After applying the CAR, we inspected the data visually and rejected large artifacts (EMG, eye movements, etc.). The last step in this pipeline is to run an algorithm called independent component analysis (ICA) to identify and reject components that contain physiological or non-physiological noise not caused by EEG dynamic. The ICA is a blind decomposition that finds maximally statistically independent variance in the EEG. It is used for identifying and removing common artifacts (such as eye blinking), electrooculogram (EOG), electrocardiogram (ECG), electromyogram (EMG) components. ICA method implemented in the EEGLAB toolbox [88] was used, and 1-2 artifact-related independent components were rejected in each subject.

Okano and Tanjis [89] recorded neuronal activity prior to externally triggered movements. They observed short-lead activity (late CNV component) which occurred within 480 ms prior to movement onset. This short-lead activity was observed in neuronal recordings in the supplementary motor area (SMA), premotor cortex, and primary motor cortex (M1) and prior to triggered movements. In another study, Shima, et al., [90] reported that the late CNV component occurs 500 ms to 2 s prior to visually triggered movement in single cell recordings in the anterior cingulate. Based on these observations and other studies, the EEG data were segmented into epochs of 2 sec duration starting 1000 ms before and 1000 ms after the onset of a finger movement.
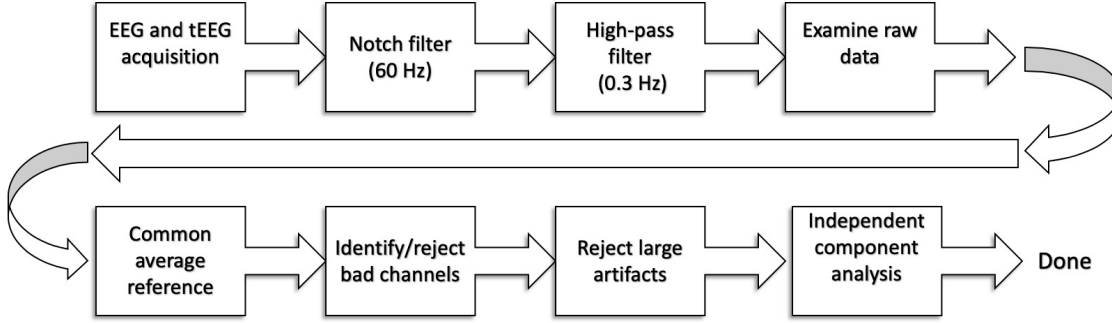
Figure 3.6: Preprocessing pipeline used to prepare the EEG data for analysis.

3.4 Calculation of Signal-to-Noise Ratio

The signal to noise ratio (SNR) has been defined as the ratio of the signal power to the noise power. In this study, we followed Klug, et al., [91] method to calculate the SNR for each tri-polar and conventional electrode using the following equation.

$$SNR = \frac{E_{peak}}{E_{noise}} = \frac{(1/p)\sum_{i=1}^{p} x_i^2}{(1/n)\sum_{j=1}^{n} x_j^2} \tag{3.2}$$

where

SNR: signal-to-noise ratio;

E: energy;

x_i: amplitude of the filtered signal (CAR and ICA) at sample i;

p: number of points in the peak;

n: number of points in the noise;

Figure 3.7 illustrates the MRP signals recorded during self-paced right index finger movement from tri-polar and disc electrodes at C_z position. The red dashed line indicates the movement onset. This figure shows how the peak signal and noise signal are determined. The peak signal window was determined as shown by the two blue vertical lines. The peak signal is chosen to be the pre-movement potential (before the movement onset) and the post-movement potential (after the onset). The remaining-activity is considered the noise signal.
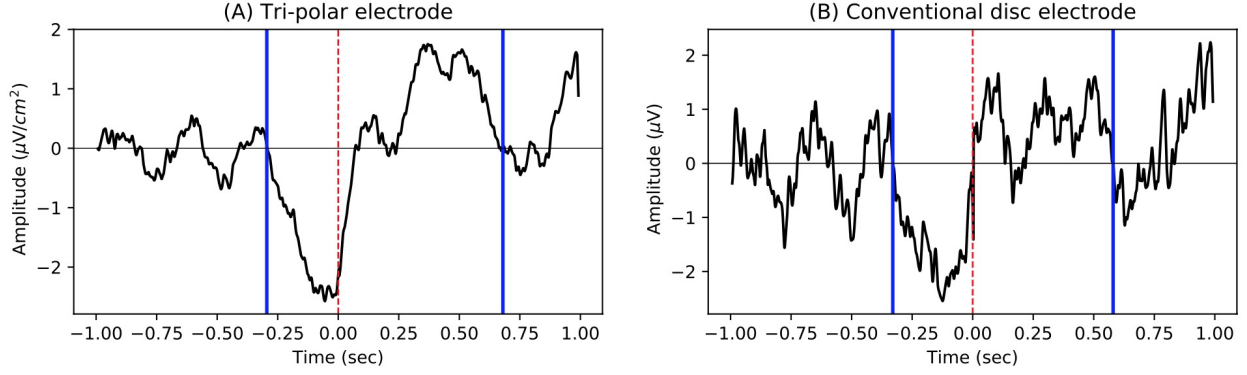
Figure 3.7: MRP signals recorded from (A) tri-polar electrodes and (B) conventional electrode at the C_Z position. Vertical dashed red line indicates the movement onset.

3.5 Measuring the Interdependency Between Neighboring Electrodes

We used two different techniques to measure the level of interdependency between different locations for the two electrode systems. The first technique is the Mutual information (MI). The MI is a measurement technique used to measure the statistical dependencies between random data variables. It was first introduced by Shannon [92]. If two random variables are strictly independent, the MI is zero. A binned process approach, which is the most common technique for estimating MI more precisely, was used for calculating the MI. The continuous valued observations are first partitioned into bins of finite size and then the number of points that fall within each bin is counted. The MI was calculated as follows [93, 94].

$$I(X_i, X_j) \approx I_{binned}(X_i, X_j) = \sum_{kl} p(k,l) log(\frac{p(k,l)}{p_{x_i}(k)p_{x_j}(l)}) \tag{3.3}$$

where $p_{x_i}(k) = \int_k dx_i \mu_{x_i}(x_i)$, $p_{x_j}(l) = \int_l dx_j \mu_{x_j}(x_j)$, and $p(k,l) = \int_k \int_l dx_i dx_j \mu(x_i, x_j)$ and $\int_k$ means the integral over bin k. $p_{x_i}(k)$, $p_{x_j}(l)$, and $p(k,l)$ are calculated by

$$p_{x_i}(k) = n_{x_i}(k)/N \tag{3.4}$$

$$p_{x_j}(l) = n_{x_j}(l)/N \tag{3.5}$$

$$p(k, l) = n(k, l)(l)/N \tag{3.6}$$

where $n_{x_i}(k)$ is the number of points falling into the kth bin of X_i, $n_{x_j}(l)$ is the number of points falling into the lth bin of X_j, $n(k, l)$ is the number of points within their interaction, and N is the total number of points in a window.

In this research, MI between each electrode for the two electrode systems (tri-polar and disc) were calculated with a custom Python script. Previous studies have shown that decreasing the MI improves the classification with fewer numbers of electrodes [94].

The second method used to measure the interdependency is the coherence, which is a tool for describing the relationship between different signals in the frequency domain. The coherence is based on the cross-correlation between two signals. The coherence values range between 0 (no coherence) and 1 (max coherence). In this study, the coherence analysis was used to measure the independency between EEG signals recorded from different electrodes for both the tri-polar electrodes and the conventional disc electrodes. The coherence between EEG signals recorded from all possible pairs of of data channels in the tri-polar and disc systems was calculated as

$$C_{x_i x_j}(f) = \frac{\left|P_{x_i x_j}(f)\right|^2}{P_{x_i}(f) P_{x_j}(f)} \tag{3.7}$$

where $C_{x_i x_j}$ is the cross-channel coherence between x_i and x_j, P_{x_i} and P_{x_j} are the spectral density of x_i and x_j, respectively, and $P_{x_i x_j}$ is the power spectral density of x_i and x_j.

3.6   Applying Local Hjorth's Laplacian on the Outer-Ring Signal

In this study, we aimed to investigate the effect of applying surface Laplacian on the EEG signal acquired from the outer ring of the TCREs. The estimation of the surface Laplacian is commonly used to enhance the spatial resolution of the conventional monopolar EEG. There are several methods available for surface Laplacian estimates. The most common method used is Hjorth's method. The Hjorth's method is obtained by computing the difference between the potential at each elec-

trode site and the average potential of its nearest four neighbour electrodes, where the distances between electrodes are equal and the angles built by the electrodes configuration are equal [95].

To estimate surface Laplacian by Hjorth's method, we used an electrode configuration shown in Figure 3.2(c). This configuration was proposed by Tandonneta et al., and MacKay [95, 96]. The electrode configuration formed the vertices of an equilateral triangle, where the "nodal" electrode (C3) was at the center of the triangle and surrounded by three other electrodes. The estimation of the surface Laplacian by Hjorth's method as modified by MacKay is given by the following equation.

$$V_{lap} = \left\{ \frac{4}{3}[3V_N - (V_A + V_B + V_C)]) \right\} / d^2 \tag{3.8}$$

where V_{lap} is the potential at the nodal electrode computed with Hjorth's method, V_N is the potential recorded at the nodal electrode, V_A, V_B, V_C are the potentials recorded at the surrounding electrodes, and d is the distance between the nodal and the surrounding electrodes. We compared the signal-to-noise ratio and the mutual information for the tri-polar concentric ring electrodes, disc electrodes with Hjorth's Laplacian, and conventional disc electrodes. The results are shown in the next chapter.

3.7   Classification Procedures

The Linear Discriminant analysis (LDA) and Artificial Neural Networks (ANNs) classifiers were chosen for classification. For LDA classifier, the classification accuracy was calculated by five-fold cross validation, where the data were split up into five subsets, with each subset used for testing once while the remaining four subsets were used for training the classifier. Before classification, the segments and the corresponding labels were randomly permuted. Then the data was randomly partitioned into training and testing sets in the ratio of 80:20. Next, the feature data and its labels in the training set were used to train the LDA classifier. This procedure was repeated 30 times to evaluate the decoding accuracies. After training the classifier, it was used to predict

labels of segment data in the testing set. The decoding accuracy was calculated as the average percentage of correctly classified trials in all five folds.

For ANNs classifier, the data was partitioned into training, validation, and testing partitions. To do this, a five-fold cross validation was performed. The ANNs classifier was trained on the training set and then evaluated on the validation set. The accuracies on the validation set were calculated and used to choose the number of hidden units. Multiple hidden layers were tested on the validation set. We observed that the validation accuracies were the best at number of hidden units equal to 10. We also tested different number of units in each layer. We observed that the best ANNs structure that lead to best accuracy is as follows: 10 hidden layers, 20 units in the first layer and 8 in each of the following 9 layers. The network was trained for 50 iterations, which was chosen by the validation accuracies result.

Chapter 4

Results and Discussion

In this chapter, the results of the experiments we outlined in Chapter 3 are presented and discussed. In the first section, the results of analyzing and comparing the MRP signals recorded using TCREs and disc electrodes are discussed. This section also discusses the results that have been obtained after applying the Hjorth's Laplacian on the outer-ring signal, as well as the comparison with TCREs and disc electrodes. In addition, this section provides and discusses the results of MRPs during contralateral and ipsilateral movements, as well as real and imagined movements. In the next two sections, the signal-to-noise ratio (SNR), mutual information (MI), and coherence of the MRP signals recorded with TCREs and disc electrodes are compared. We also study and evaluate two types of EEG features, including temporal EEG data and spectral power increases and decreases in both α and β bands during individual finger movements from one hand, and the results are presented in Section 4. Section 5 provides a comparative analysis of ERD/ERS between TCREs and disc electrodes. Finally, we report and discuss the results of applying LDA and ANNs classifiers to the datasets in the last section.

4.1 Movement-Related Potentials

Two data sets recorded during self-paced and cued-paced conditions are presented and discussed. The first data set consists of tri-polar EEG (tEEG) and conventional EEG (cEEG) recorded from one subject using four electrodes (C_z, C_1, C_3, and C_5) over the contralateral motor area during self-paced movement (finger tapping). The experiment was conducted in the Neuro Rehabilitation Laboratory at the University of Rhode Island. The second data set consists of tEEG and cEEG recorded from 13 subjects using the same electrodes. The electrodes were placed on the scalp using three different montages as shown in Figure 3.2. However, the subject followed the proposed method explained in Section 3.1. The experiment was conducted in the EEG Labora-

tory at Colorado State University. Two different movement-related potentials (MRPs) components, Bereitschaftspotential (BP) and contingent negative variation (CNV), were recorded and analyzed.

Figures 4.1 and 4.2 show grand averages of movement-related potentials (MRPs) waveforms at four electrode sites recorded over the contralateral motor cortex during self-paced, voluntary right index finger movement. The data in Figures 4.1 and 4.2 was not filtered by CAR or ICA and no trials were removed. The two main components of the MRP, pre-movement peak (pre-MP) and post-movement peak (post-MP), are observed in both tEEGs and cEEGs. The pre-MP and post-MP differ in latency and topography. The waveforms of the MRPs recorded from the TCREs show significant differences in the relative size of its components depending on the site of recording. These differences were not seen in the MRPs recorded from disc electrodes, Figure 4.1(b).

The pre-MP is a negative deflection preceding the movement onset. We can see clearly in Figures 4.1 and 4.2 that its amplitude decreases as we move toward the temporal electrodes sites. For instance, the pre-MP at C_1 is approximately 50% of its amplitude at C_z. Starting with a negative deflection at about 250 ms before the movement onset, the pre-MP peaked in C_z at about 12 ms after the movement onset, followed by a positive deflection starting approximately 30 ms after the movement onset. The post-MP component follows the movement onset. Its amplitude decreased toward the temporal electrodes. Mostly, it was absent in the channel posterior to C_3 (e.g., C_5). The post-MP peaked in C_z at approximately 80 ms after the movement onset. At the time of finger movement onset, pre-MP decreases to about 30-40% of peak amplitude, followed by a positive deflection starting approximately 50 ms after the movement onset.

From Figure 4.1, we can see that contralateral index finger movements elicited MRPs with significantly larger amplitudes of the BP recorded from TCREs compared to the BP recorded from the conventional disc electrodes. Moreover, the BPs in the tEEG (Figure 4.1) are more distinguishable and have less noise as compared to those in the cEEG. This result shows that the TCREs provide higher spatial resolution than the conventional EEG electrodes. In addition, these findings suggest that the TCREs detect the MRPs more precisely.

It has been shown that if the conventional electrodes are placed any closer on the brain surface than about 4 cm they will see the same signal. However, the MRPs, as shown in Figure 4.2, are quite different among the tEEG electrodes (left column), even though they are placed close on the brain surface. To improve control of BCIs we need to improve the EEG spatial resolution. According to our results we hypothesized that using TCREs non-invasively is adequate to detect brain activity that will decode the movement of fine body parts such as finger movements with high accuracy.
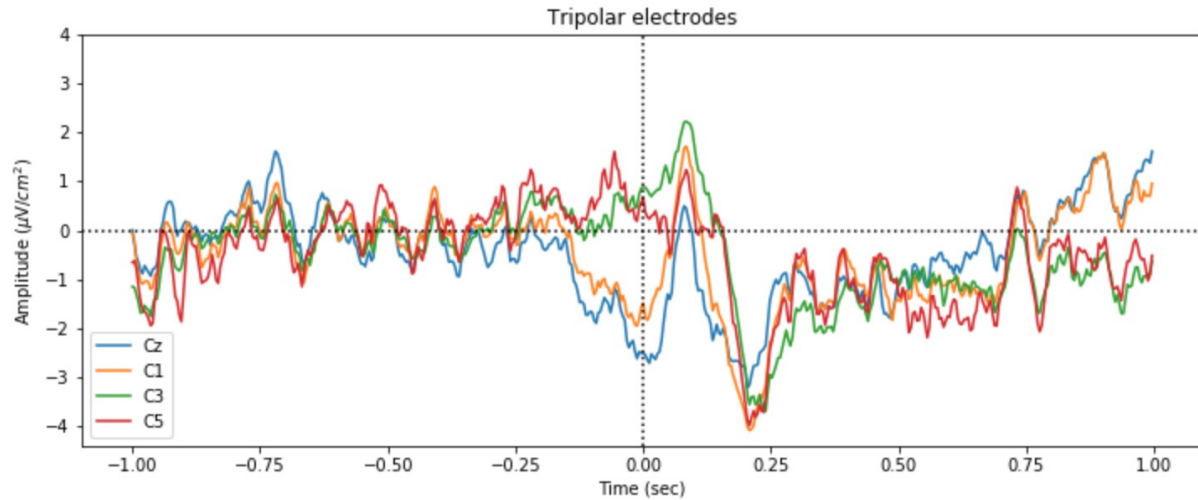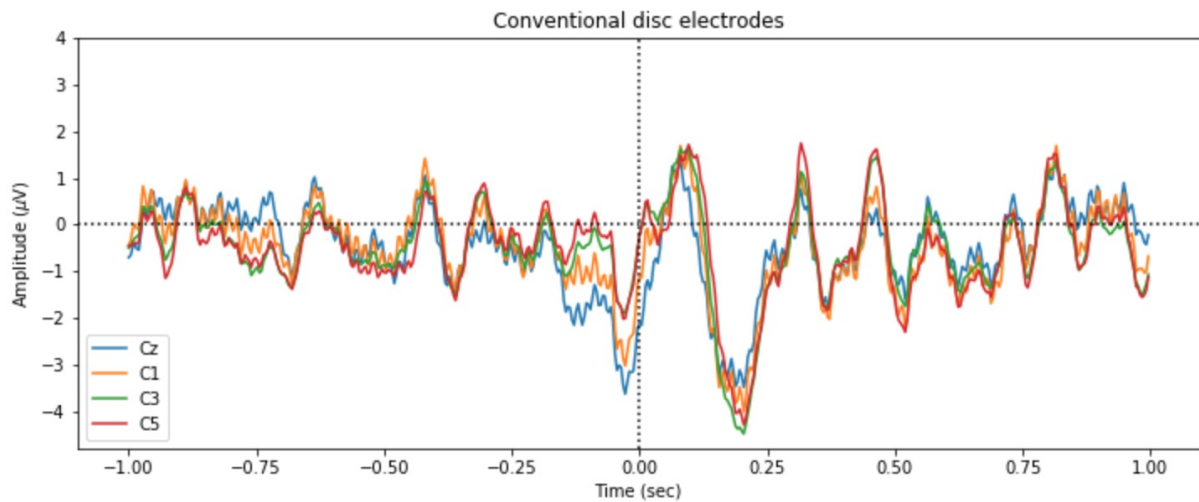
Figure 4.1: Grand averages of the Movement-related potentials (MRPs) preceding and accompanying the execution of index finger movement recorded from tri-polar ring electrodes (a) and conventional disc electrodes (b). Epoch length was 2 sec, starting 1 s before and ending 1 sec after onset of movement onset. These MRPs are averages of 60 trials. The vertical line indicated the movement onset.
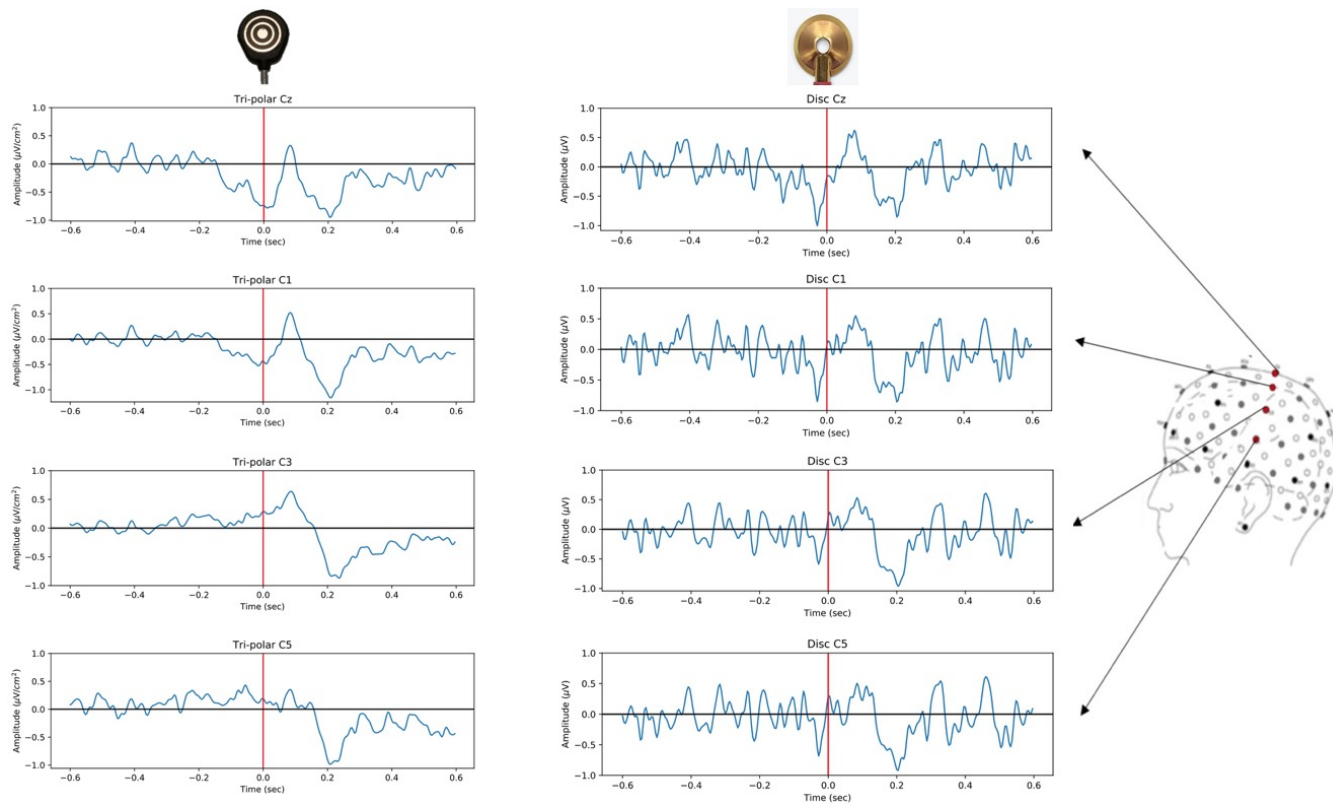
Figure 4.2: Movement-related potentials (MRPs) during a self-paced finger movement task. The conventional EEG see the same signal at different locations. In contrast, the TCREs show different MRPs. Data are averages of 211 self-paced right index finger movements. Vertical red lines indicates the movement onset.

The average waveforms of CNV recorded from tri-polar and disc electrodes during real finger movements are shown in Figure 4.3 (a) and (b), respectively. The late CNV is clearly seen as a negative slope during index finger movements at all recording sites in both tri-polar and disc electrodes. The late CNV, a negative slow potential, started about 1380 ms after the S1, and gradually increased in amplitude until the movement onset at all recording sites. In the tEEGs, the late CNV measured at 1380 ms after the S1 was -3.67±1.28 μV at Cz, -2.25±2.02 μV at C1, -4.05±3.31 μV at C3, and -3.88±1.92 μV at C5 (mean±SD). In the cEEGs, the late CNV was -3.67±1.28 μV at Cz, -2.25±2.02 μV at C1, -4.05±3.31 μV at C3, and -3.88±1.92 μV at C5 (mean±SD), and and no significant difference of the late CNV amplitude was observed at those 4 sites.

The use of TCREs have been shown to have enhanced characteristics over disc electrodes. Previous studies have compared different EEG characteristics such as spatial selectivity and SNR for different electrodes systems, including: TCREs, bipolar concentric ring electrodes, and disc electrodes. A few of them conducted this comparison on MRPs. Here, we compare the MRPs recorded from TCREs and disc electrodes. The signal-to-noise ratio (SNR), coherence, and mutual information (MI) of the MRP signals recorded with the TCREs and disc electrodes were compared.

With tri-polar concentric and disc electrodes, the BPs and CNVs were recognized as slow negative potentials preceding the movement onset. Figures 4.1 and 4.3 show that the MRPs recorded using the TCREs are more distinguishable than the disc electrodes. This result was expected as the TCREs apply surface Laplacian based on the nine-point method which have higher attenuation of global signals, and this attenuation improves the spatial selectivity of the signals. For the conventional disc electrodes there is not much difference in the signal morphologies noted in all four locations. These results suggest that the TCREs have the ability to measure more localized brain activity than the conventional disc electrodes. Since the finger movements activate adjacent brain regions and elicit close cortical motor, we hypothesized that with the TCREs, it is possible to record high spatial and temporal resolution of EEG. By increasing the spatial and temporal res-

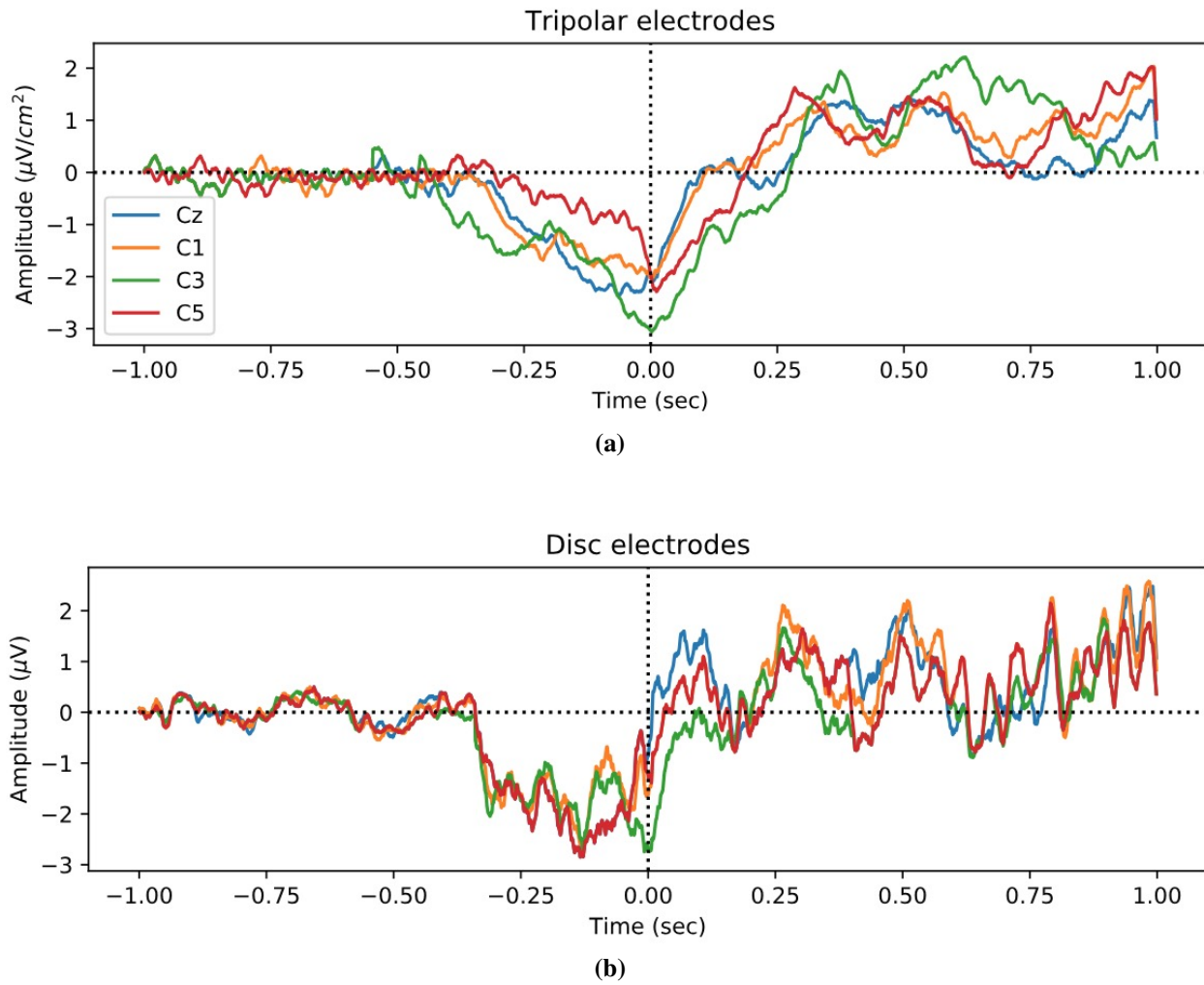olutions of EEG, we can decode different fingers movement from the scalp with high decoding accuracy.

Figure 4.3: Grand averages of the Movement-related potentials (MRPs) preceding and accompanying the execution of middle finger movement recorded from tri-polar ring electrodes (a) and conventional disc electrodes (b). These MRPs are averages of 43 trials. The vertical red line indicated the movement onset.

We also studied the effect of applying surface Laplacian computed by Hjorth's method on the outer-ring signal. Figure 4.4 presents monopolar (μV; top), Laplacian computed from Hjorth's method (μV/cm^2; middle), and tri-polar (μV/cm^2; bottom) grand averages of MRPs. Similar topographic information was observed in all waveforms. A negative wave at C3 site starts about 1300 ms after the S1 stimulus, and peaking about 20 ms before the finger movement onset. The other waveforms show similar negative wave beginning at the same latency, but peaking at different time (130 ms before the movement onset). To further examine the effect of the Laplacian on the outer ring signal of the TCREs, we compared the SNR and mutual information for the different electrode systems. The results are presented in the following sections.
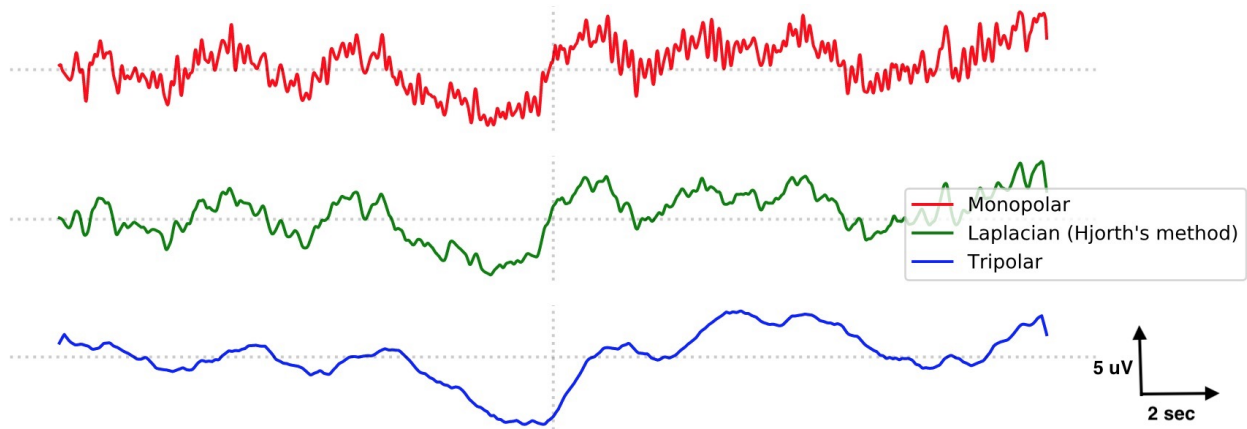
Figure 4.4: Monopolar (μV; top), Laplacian computed from Hjorth's method (μV/cm^2; middle), and tri-polar (μV/cm^2; bottom) grand averages of MRP for real middle finger movement. Vertical line indicates movement onset

We studied the temporal EEG changes associated with contralateral and ipsilateral individual finger movement. Figure 4.5 shows the MRP for both contralateral and ipsilateral ring finger movement. In recordings above the primary motor cortices (C3, C4) CNV was observed with larger amplitudes contralateral to the moving finger (C3 > C4). Moreover, the contralateral and ipsilateral recordings were different from each other in the latency and amplitude of MRPs. Before the finger movement onset, the contralateral MRP occurred earlier (by 14 ms) than the ipsilateral MRP. The result demonstrates that both contralateral and ipsilateral finger movements can be
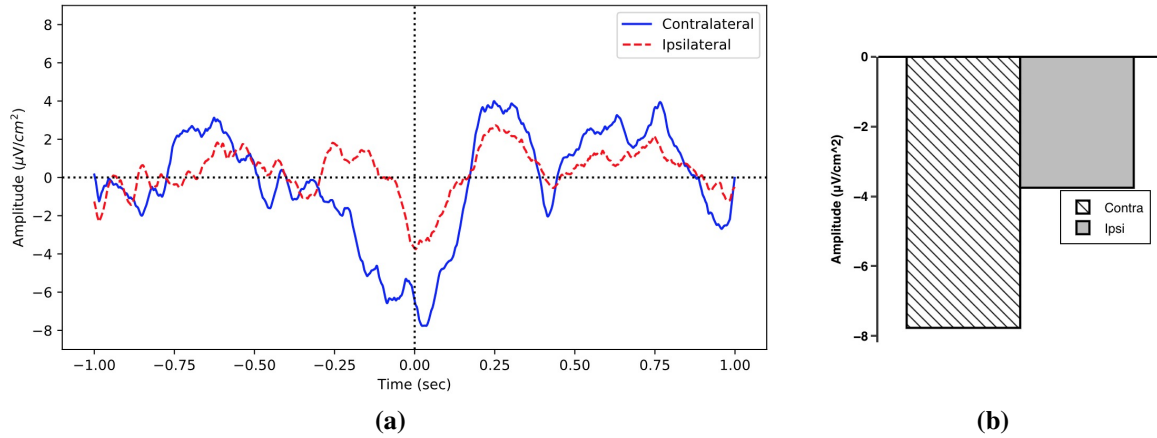
Figure 4.5: MRP associated with contralateral and ipsilateral finger movement. The CNV is present similarly for movement of either side.

discriminated from EEG signals recorded from a single brain hemisphere. The possibility of decoding both contralateral and ipsilateral finger movements would have important implications for neurorehabilitation, in particular for the use of BCI in stroke recovery patients.

We also studied the possibility of distinguishing movements from rest periods. Figure 4.6 shows the MRP for right thumb movement (blue) versus rest (red). We can see that the amplitude of the post-MP is higher for contralateral C3 channel located over the sensorimotor cortex than for rest. This result suggests that we can discriminate between movement and rest in the time domain as well as in the frequency domain. Classification experiments are described in Section 4.6.
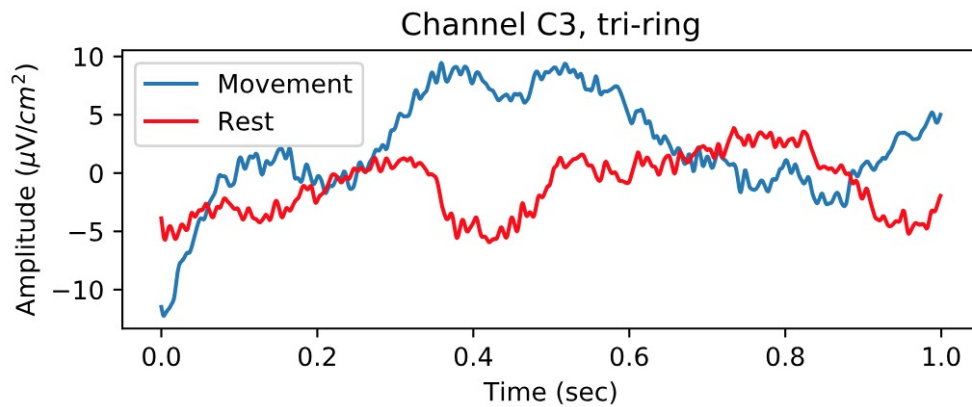
Figure 4.6: Time-course of average EEG trace from channel C3 during rest (in red) and right thumb movement in one subject.

The late CNV components related to movement preparation and execution were examined separately by comparing CNVs associated with imagined and actual finger movements. Figure 4.7 illustrates with data from one subject the MRP of ring finger recorded from tri-polar C3 electrode during real (black) and imagined (red) movement task. The result shows that motor imagery activates sensorimotor cortex in a similar way to movement execution. Previous studies have shown that movement imagination and movement execution share a lot of similarity. For instance, Personnier, et al., found that imagined and real movement follow the same spatial-temporal constraints [97]. Also, neuroimaging techniques have shown that movement imagination and movement execution reveal overlapping activity in the cortical areas [98]. These similarities between movement imagination and movement execution leads to the fact that movement imagination has been suggested as a promising rehabilitation approach for patients suffering from stroke [99].
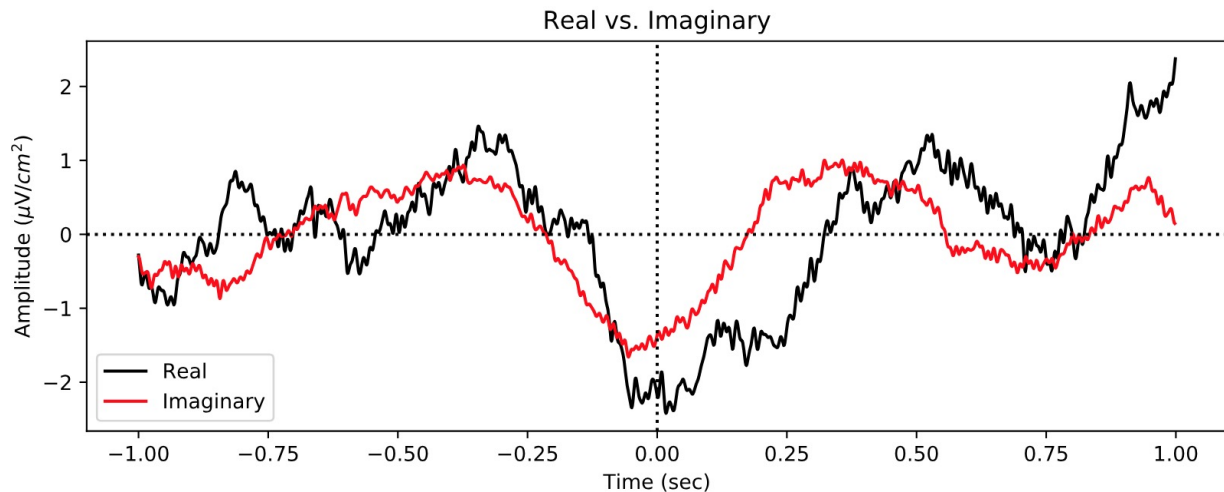
Figure 4.7: Grand averages of the Movement-related potentials (MRPs) of ring finger recorded from tri-polar C3 electrode during real (black) and imagined (red) movement task.

4.2 Mutual Information and Coherence

Mutual information (MI) of the MRP signals recorded with the different electrode systems was calculated using equation 3.3. Additionally, the MI of the different electrode systems were compared using a single factor ANOVA and Bonferroni tests. Table 4.1 shows the grand averages of

the MI for each subject for different electrode systems. The MI of the tri-polar and disc electrodes were statistically compared and the results are shown in Figure 4.8. Furthermore, we compared the MI between the disc, tri-polar, and the disc with Hjorth Laplacian, and the results are illustrated in Figure 4.9.

The MRP signals recorded with the TCRE system have significantly less ($p < 0.0001$) MI between electrodes than the conventional disc electrode system and disc with Hjorth Laplacian ($p=0.003$). On the other hand, the result shows no significant difference between disc electrode and disc with Hjorth Laplacian ($p = 0.719$). These results suggest that the TCRE data have less MI than the other two systems even if we apply the Laplacian on the signals recorded from the outer ring.

Koka, et al, compared the MI between three different electrode configurations: tri-polar, bipolar, and disc electrodes [34]. They found that the MI for TCREs was significantly less ($p = 0.0104$) than the other two systems. Koka, et al., suggested that the significance in the decrease of MI may be improved by increasing the number of channels recorded concurrently.

The MI results showed the interdependency between the neighbouring electrodes in the time domain. To measure the level of interdependency in the frequency domain, we measured the inter-electrode coherence. EEG coherence was computed between neural signals recorded from all possible pairs of electrodes in the tri-polar and all possible pairs in the disc electrode systems using equation 3.7. The coherence values were compared over the following frequency bands: 1-4Hz (δ), 4-7Hz (θ), 7-12Hz (α), 12-30Hz (β), 30-60Hz (γ) followed [100]. Table 4.2 shows coherence values between four electrode pair combinations for tri-polar and disc electrode systems from one subject at different frequency bands. Figure 4.10 shows the grand average coherence averaged over 10 subjects at five frequency bands. Figure 4.11 compares the coherence values at various frequencies between neighboring electrodes for the tri-polar and the disc electrode systems.

The mean coherence between neighboring tri-polar electrodes was found to be 0.6, 0.53, 0.36, 0.24, and 0.15 for δ, θ, α, β, and γ, respectively. Moreover, the mean coherence between neighboring disc electrodes was 0.92, 0.87, 0.78, 0.74, and 0.63 for δ, θ, α, β, and γ, respectively. The

Table 4.1: Grand averages of MI for different electrode systems.

	Disc	tri-polar
Subject 1	0.235	0.017
Subject 2	0.310	0.028
Subject 3	0.401	0.022
Subject 4	0.226	0.026
Subject 5	0.198	0.019
Subject 6	0.301	0.022
Subject 7	0.271	0.019
Subject 8	0.288	0.020
Subject 9	0.313	0.022
Subject 10	0.311	0.019
Average	0.285	0.021

coherence was found to decrease at higher frequencies. The coherence of the high frequency band (γ) recorded by neighboring tri-polar electrodes shows the lower than that of the disc electrodes, indicating greater signal independence. The lower coherence in the high frequency band between electrodes suggests that it may reflect a more localized neuronal activity [73]. The disc electrodes exhibited higher coherence at all frequency bands than that observed in the tri-polar electrodes, indicating a significant amount of dependence between them for recording neural activity.

The pioneering study by Wang and his colleagues has demonstrated that the coherence between ECoG electrodes decreases at higher frequency band [101]. Our results suggest that the TCREs have low coherence between electrodes, especially at γ band, similar to ECoG electrodes. We suggest, based on the results presented here, that TCREs is a promising recording method for obtaining high quality signals especially for the BCI based on the high-frequency rhythms.
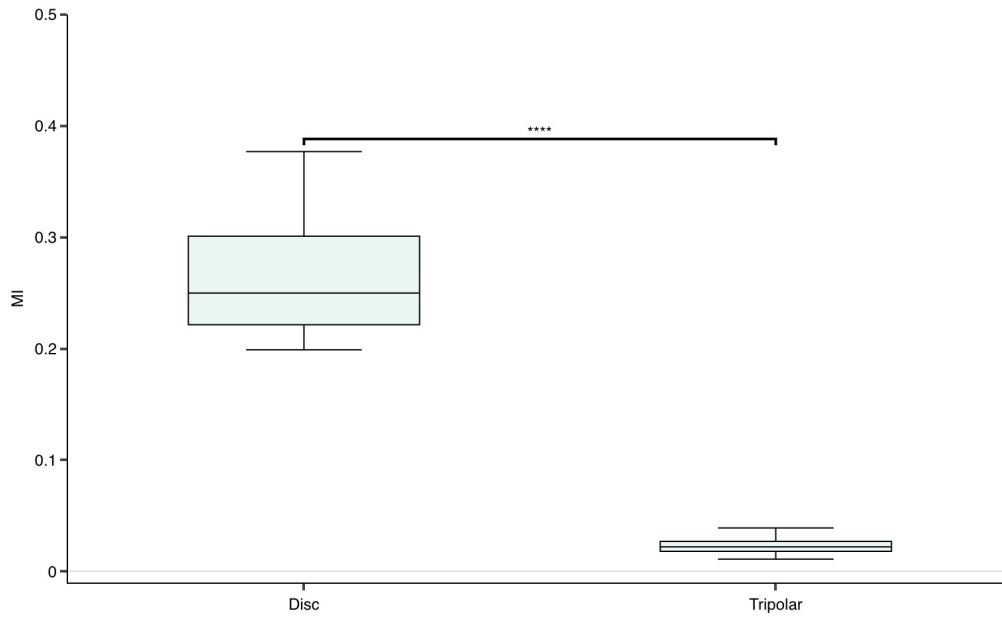
Figure 4.8: Box-plot comparing the MI of disc and tri-polar electrodes. $^{****}p < 0.0001$.
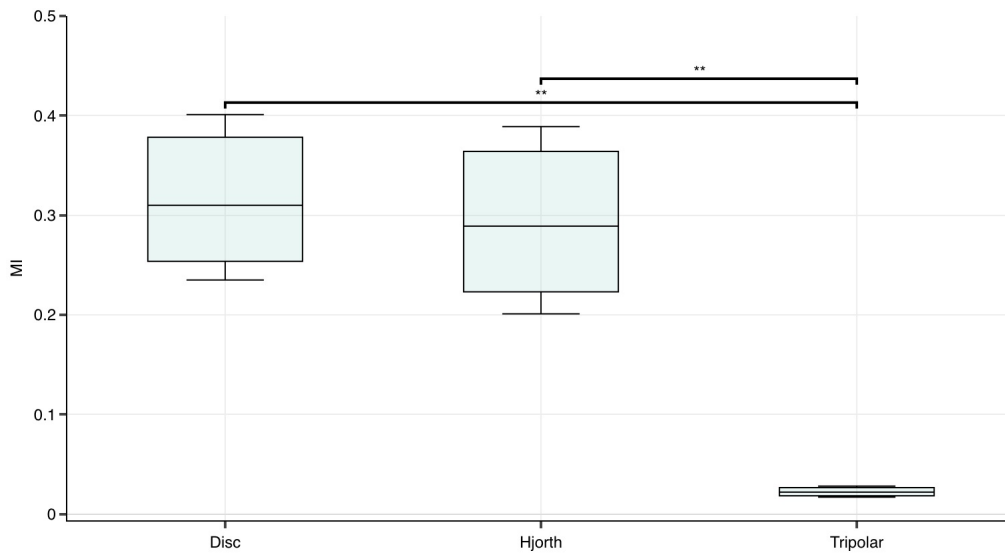
Figure 4.9: Box-plot comparing the MI of disc, disc with Hjorth, and tri-polar electrodes. $^{**}p < 0.01$.

Table 4.2: Coherence values between four channels for tri-polar and disc electrode systems from one subject. The coherence values were compared over the following frequency bands: 1-4Hz (delta), 4-7Hz (theta), 7-12Hz (alpha), 12-30Hz (beta), 30-60Hz (gamma).

Channels	Delta		Theta		Alpha		Beta		Gamma	
	Tri-polar	Disc	Tri-polar	Disc	Tri-polar	Disc	Tri-polar	Disc	Tri-polar	Disc
Cz, C1	0.895	0.968	0.821	0.938	0.672	0.887	0.352	0.652	0.129	0.786
Cz, C3	0.568	0.918	0.340	0.849	0.295	0.729	0.136	0.412	0.075	0.633
Cz, C5	0.830	0.892	0.691	0.766	0.471	0.590	0.164	0.231	0.107	0.374
C1, C3	0.612	0.949	0.462	0.926	0.377	0.881	0.262	0.770	0.020	0.757
C1, C5	0.896	0.931	0.801	0.864	0.647	0.757	0.302	0.467	0.124	0.491
C3, C5	0.585	0.932	0.442	0.919	0.362	0.865	0.233	0.676	0.106	0.610
Average	0.731	0.932	0.593	0.877	0.471	0.785	0.242	0.535	0.094	0.609

Figure 4.10: Grand averaged cross-channel coherence over all 10 subjects at the different frequency bands analyzed for tri-polar and disc electrodes.

Figure 4.11: Coherence analysis for the tri-polar electrodes (black lines) and the disc electrodes (blue lines).

4.3 Signal-to-Noise Ratio

We used the MRP signals to compare the SNR for tri-polar concentric ring electrodes and conventional disc electrodes, as shown in Figure 3.7. The SNR of the two different electrode configurations was calculated for the signals at each location using equation 3.2. Table 4.3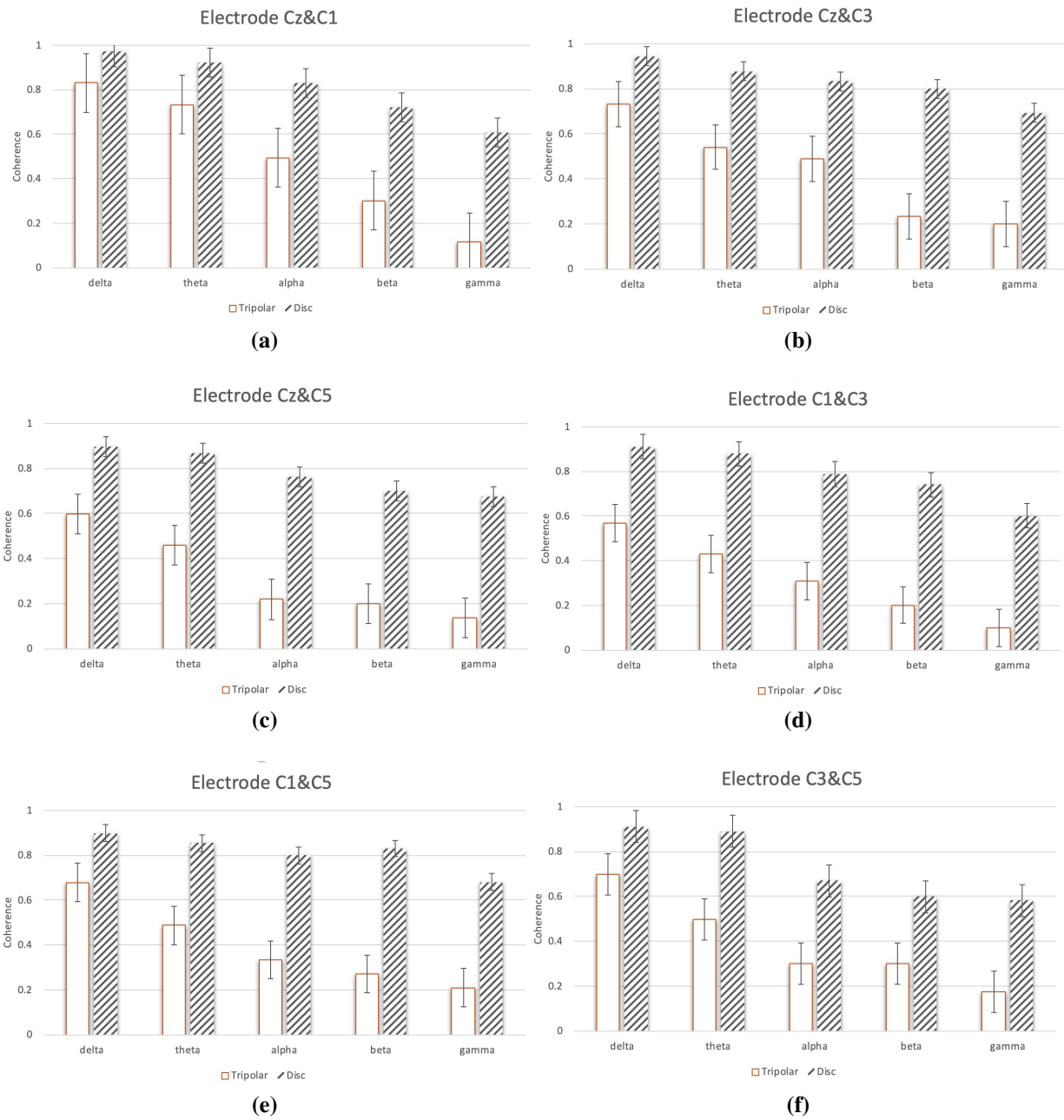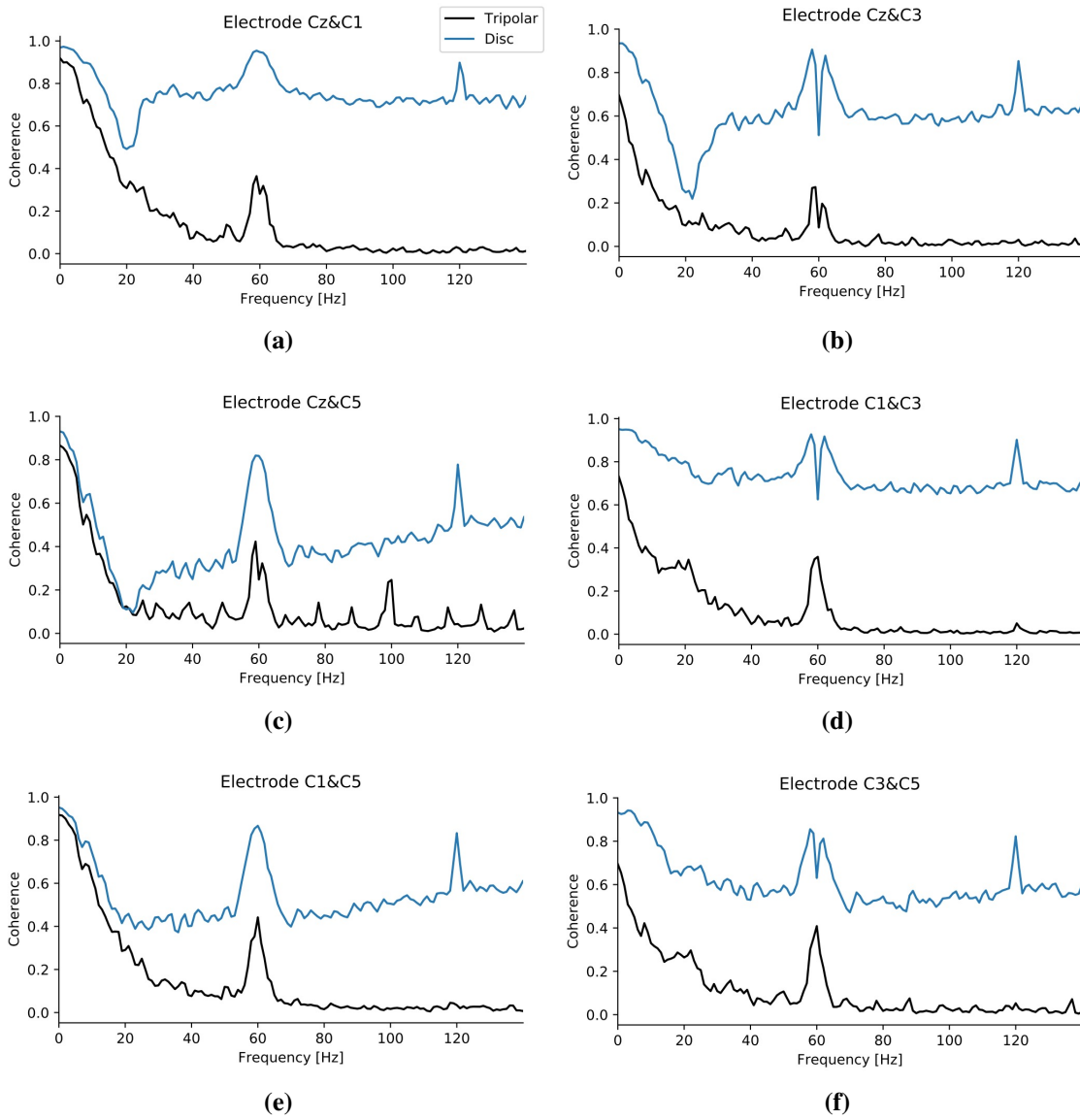 and Figures 4.12 and 4.13 show the SNR for the conventional disc and tri-polar electrodes for the real index finger movement data. It can be seen clearly that the signals from tri-polar concentric ring electrodes have significantly higher SNR than the signals from the conventional disc electrodes. For the MRP signals, the tri-polar electrode has mean SNR of 4.854 and the conventional disc electrode has mean SNR of 1.115. The tri-polar concentric ring electrodes have higher SNR because they have higher attenuation of global signals, and this attenuation improves the spatial selectivity and, as a result, higher spatial resolution [33, 51]. A previous study has shown that the EEG recorded with the TCRE (tEEG) has about a 4-fold (374%) increase in signal-to-noise ratio (SNR) as compared with disc signals [59]. These results suggest that using the TCREs will attenuate the volume conductance effects significantly.

The SNR data was analyzed using a single factor ANOVA test. The SNR of the tri-polar concentric ring electrode signals showed significant improvement (p = 5.48E-10, Table 4.4) over the SNR of conventional disc electrode emulation. This higher SNR provided by TCRE will increase the ability to extract meaningful information from the recorded signals and therefore simplify the BCI's detection and classification task.

Table 4.3: Averaged SNR for conventional disc electrodes and tri-polar electrodes

	Disc	Tri-polar
Subject 1	1.220	5.672
Subject 2	1.548	5.344
Subject 3	0.631	5.611
Subject 4	1.105	3.679
Subject 5	0.556	4.644
Subject 6	0.982	3.302
Subject 7	1.390	5.691
Subject 8	1.011	4.998
Subject 9	0.782	4.093
Subject 10	0.921	5.504
Average	1.115	4.854
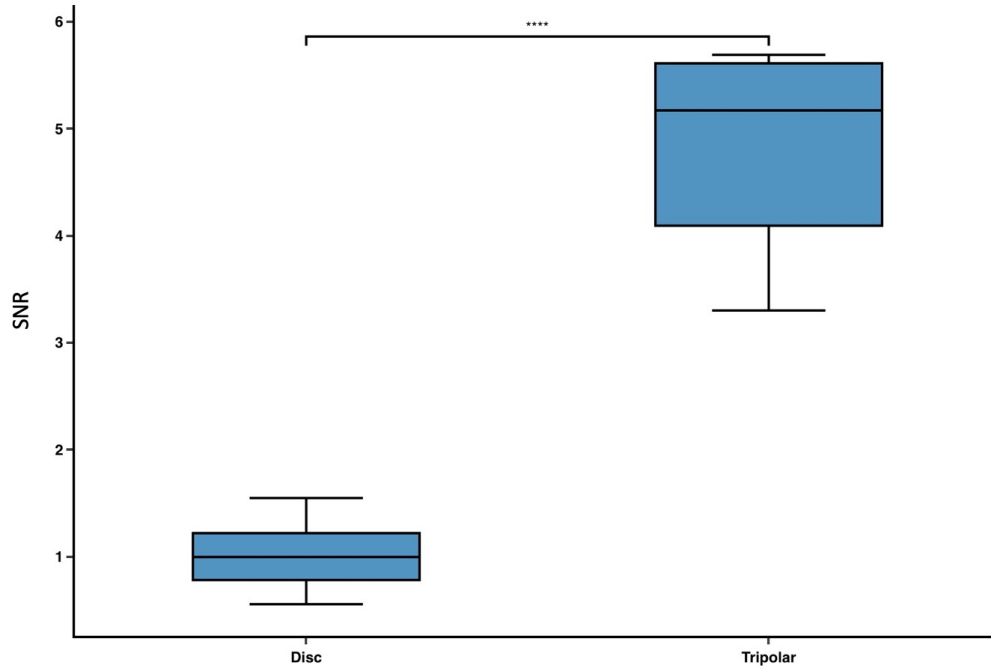
Figure 4.12: Box-plot comparing the SNR of disc and tri-polar electrodes. ****$p < 0.0001$.
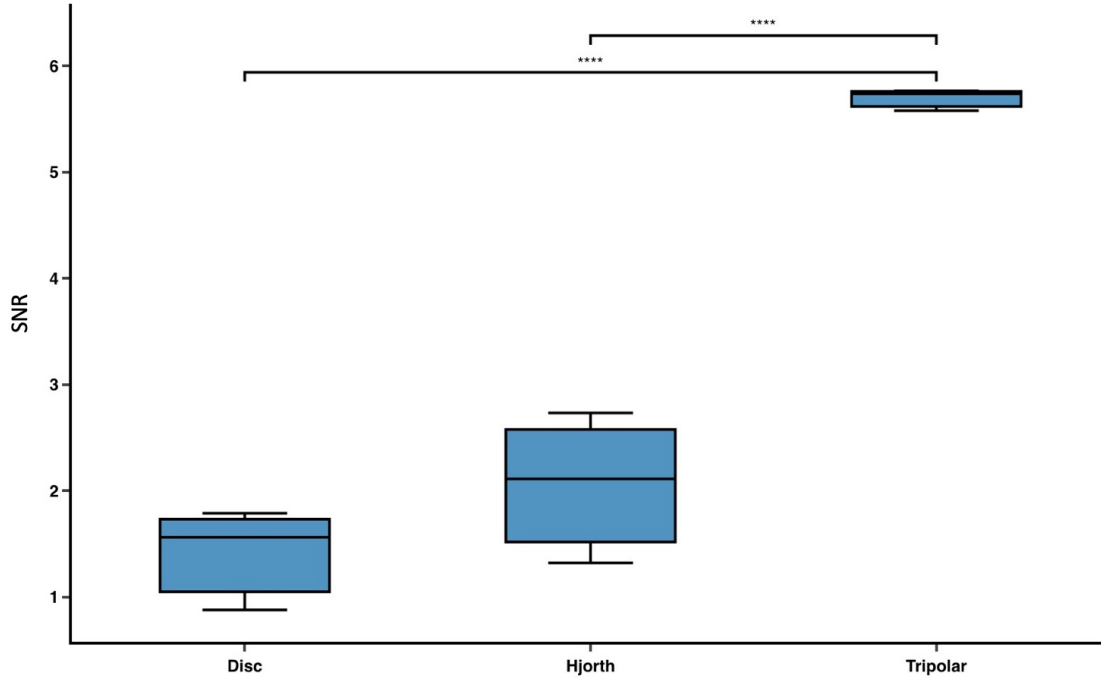
Figure 4.13: Box-plot comparing the SNR of disc, Hjorth, and tri-polar electrodes. ****$p < 0.0001$.

Table 4.4: ANOVA table

Source of Variation	SS	df	MS	F	$P\text{-}value$	F_{crit}
Between Groups	69.91	1	69.91	142.53	5.48E-10	4.41
Within Groups	8.83	18	0.49			
Total	78.74	19				

4.4 Evaluation of Temporal and Frequency Features in Decoding Individual Finger Movements

Figure 4.14 shows grand average MRP waveforms from different fingers recorded using tripolar (a) and disc (b) C3 electrode during real finger movement task. For all fingers, the late CNV was clearly seen at C3 electrode site. Those waveforms present similar pattern prior to the finger movement onset in the disc electrode (b). However, different EEG patterns prior to the finger movement onset was observed in the tri-polar electrode. This results suggest that we can use the tri-polar electrodes to predict the intention of the movement of a specific finger from EEG signals using temporal data. Even though the individual finger representations are known

to largely overlap, these differences in the late CNV amplitudes from each finger detected by tri-polar electrode are evidence on the superiority of the tri-polar electrodes to the disc electrodes in recording more localized EEG activity from the scalp.

The differences in the CNV amplitudes for movements are due to many factors, and some are mentioned in Section 2.3. The movement of the middle finger is more difficult and effortful than index finger movements. If we compare the CNV of the index and middle fingers, we can see that the CNV amplitude for movements of the middle finger is larger than the CNV amplitude for index finger. This difference was expected since a complex movement would generate a larger amplitude of CNV due to greater activation of SMA as compared to simple movement. Similarly, the movement of the ring finger is more complex than of the little finger, thus the CNV amplitude of the ring finger is larger. The figures also show that different fluctuations in amplitudes can be seen from different finger movements after the movement onset from both tri-polar and disc electrodes. Because these fluctuation in amplitudes were seen in both electrode systems, we selected the time window (1 sec) after the movement onset to decode individual finger movements. Based on these results, we hypothesized that it is possible to classify movements from five fingers using temporal data as movement-related features with high decoding accuracy, especially with the tri-polar electrodes.

In this study, we used movement-related spectral changes as features to classify fingers movements and compare them with the temporal EEG features. Particularly, increases and decreases of the spectral power in α (8-13 Hz) and β (13-30 Hz) bands were utilized as features to decode individual finger movements from one hand. To estimate the power spectral density (PSD) of EEG on each channel, we used Welch's method. We first split the EEG data into a short-time Hanning window T centered at movement peaks τ_q, where q = 1,2,...,5 is the time window at different fingers. Then, for each window, the discrete Fourier transform (DFT) was computed. Finally, all the DFTs were scaled and averaged together as follows [28, 79].

$$P_n(f, \tau_q) = \frac{1}{T} \left| \sum_{t=-\frac{T}{2}}^{\frac{T}{2}-1} X_n(\tau_q + t) \, |H(t)| \, exp(i\frac{2\pi}{T}(f-1)t)) \right|^2 \tag{4.1}$$

where $P_n(f, \tau_q)$ is the PSD at frequency f and time τ_q on channel n, $H(t)$ is the Hanning window, and T is the window length.

Figure 4.15 shows the averaged α and β power changes from C3 electrode over the contralateral motor cortex from both tri-polar (a) and disc (b) electrodes. We compared the power changes between different fingers and between movement data and resting data. The resting data were selected as 1 sec segments after the S1 stimulus onset. We can see that all finger movements elicit power decreases (ERD) in both α band and β band compared to the resting condition. Two identifiable peaks are present in the rest condition, one in the α band at approximately 10 Hz and one in the β band at approximately 20 Hz. Power in these bands were greater at rest than during the movement for all fingers. Interestingly, the spectral power changes among different finger movement conditions can be identified in both α and β bands with the tri-polar electrode. However, spectral powers changes did not discriminate between different fingers movement when we used disc electrode.

The high-frequency band (HFB) power (> 35 Hz) is commonly used to differentiate between different movements because it has been shown that the HFB contains distinct spatial activation patterns for different body parts [102]. On the other hand, the low-frequency band (LFB) power (α and β) features are less informative for motor activity, and are not sufficient for good classification between different body parts. Here, with the tri-polar electrodes, the LFB power can be utilized as features to discriminate between different fingers movement-associated activations, whereas the disc electrodes do not.
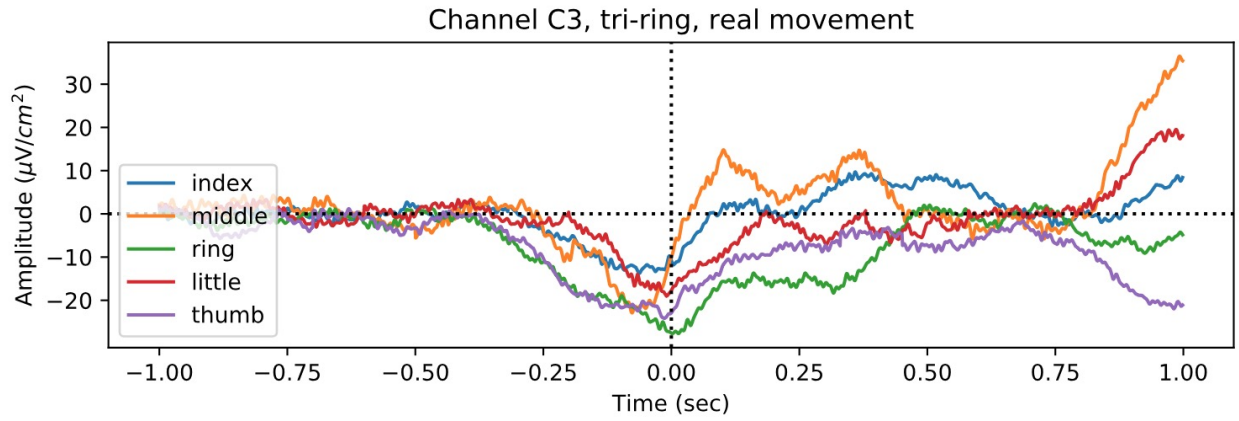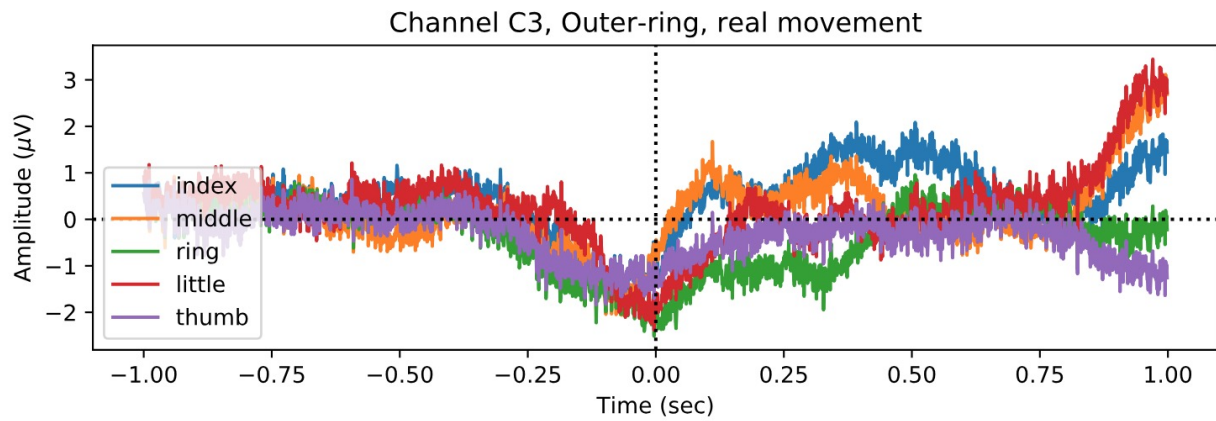
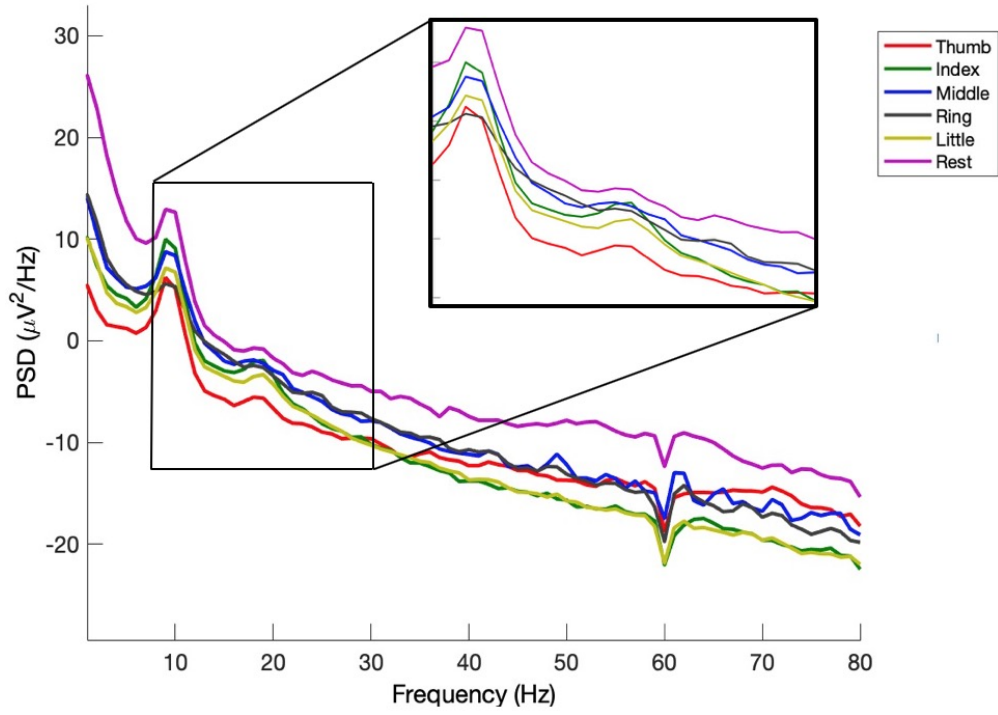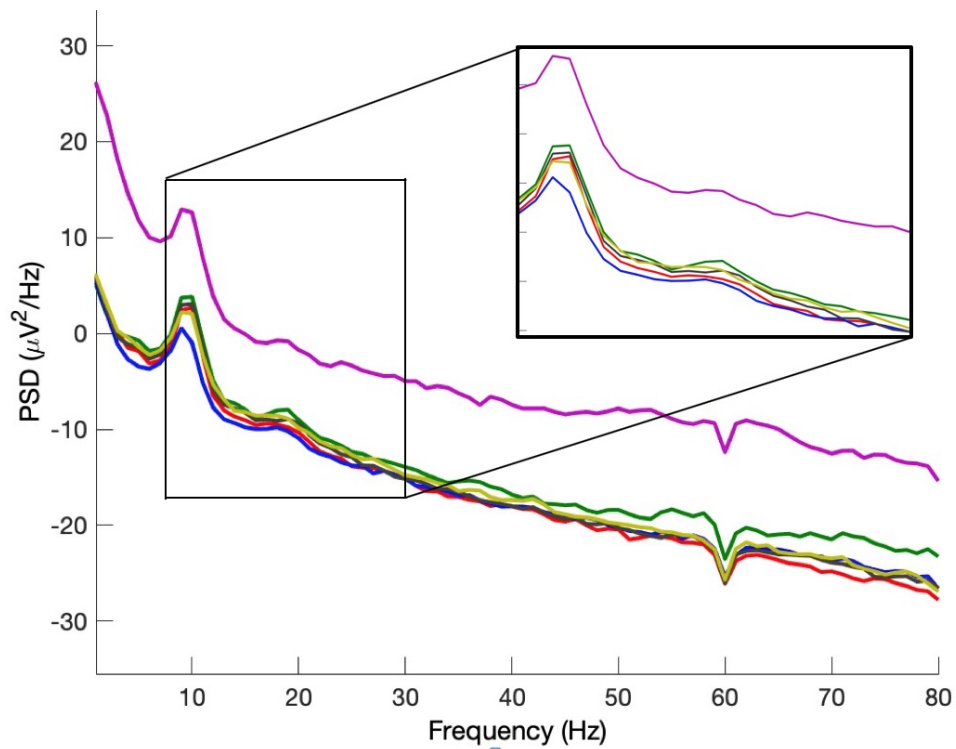**Figure 4.14:** Grand averages of the Movement-related potentials (MRPs) of different fingers recorded from tri-polar ring electrodes (a) and conventional disc electrodes (b). Epoch length was 2 sec, starting 1sec before and ending 1sec after onset of movement onset. The vertical red line indicated the movement onset.

Figure 4.15: Averaged alpha/beta power changes from tri-polar (a) and disc (b) C3 electrode.

## 4.5 EEG (De)synchronization Prior, During, and After Finger Movement

A comparison of ERD/ERS between tri-polar and disc electrodes in a real thumb finger movement is given in Figure 4.16. Starting with low frequency changes, pre-response θ-band ERS can be observed. We can see that thumb finger execution elicits power changes in different frequency bands. An α and β ERS started about 800 ms prior to the movement onset followed by ERD is shown in Figure 4.16. In addition, ERD in α band was found during and after the movement onset. Furthermore, the results demonstrated before the beginning of thumb finger movement an existence of a 10 Hz ERD. The results also show post-movement β ERS started 100 ms after the movement onset. These ERD/ERS may be considered to be due to a decrease or an increase in synchrony of the underlying neuronal populations, respectively. ERD and ERS were visible in all subjects for real movement and imagined movement.

Movement or preparation for movement is typically accompanied by a decrease in μ and β rhythms, particularly contralateral to the movement. The ERD around 10Hz can represent an electrophysiological correlate of activated different cortical areas related to motor preparation [103, 104]. In the present study, the finger movement does not result only on ERD in the upper α (μ) band, but also in ERS. This enhancement in the α band may be due to the fact that the subject was receiving a visual input during the experiment. Brechet and Lecasble found a synchronized upper α (μ) band rhythm during flicker stimulation [105]. Also, Koshino and Niedermeyer reported an enhanced μ rhythms during pattern vision test [106]. A few studies have reported an α post-movement ERS, such as in [13].

The β ERS after the movement onset was not strong, and this is because a small muscle mass is required to move one finger and a small population of cortical neurons is required. However, for the large body parts such as wrist, the β ERS is significantly large as compared to finger movement [107]. Another factor affecting the size and amplitude of the ERD is the complexity of the movement task. Derambure et al., compared the ERD in elderly and young subjects during

planning of voluntary finger movements task. They found a spatial diffusion of ERD over motor and premotor areas in elderly subjects compared with young subjects which was limited to the central regions [108].

Additionally, we can notice the decrease of power in the β-band (16–28 Hz) after movement onset for the channel from the left sensorimotor region. The results also show a strong induced oscillations in γ band prior the movement onset for tri-polar electrode as compared to disc electrode. Around 60 and 80 Hz, we can see γ ERS started about 800 ms prior the movement onset. Recent ECoG studies have found that there is a significant γ power increase prior movement onset representing neural activation beyond somatosensory feedback [109, 110]. Similar finding was reported in [111].
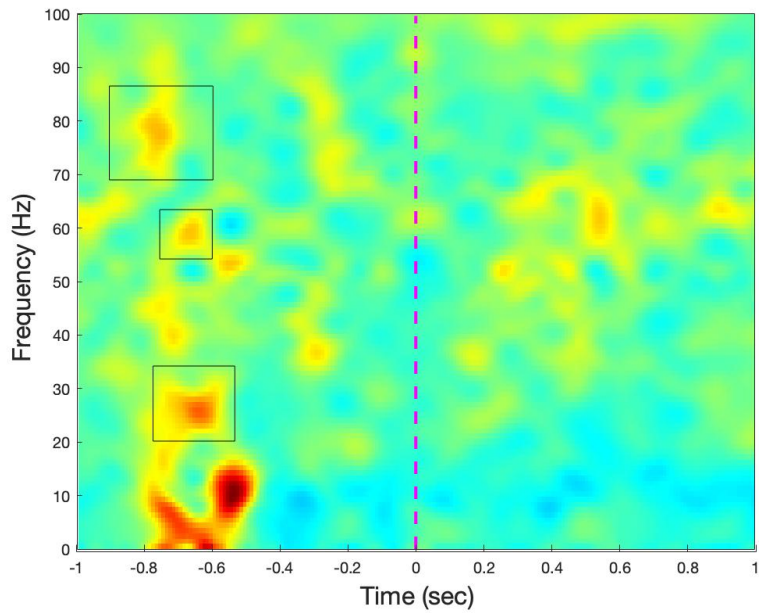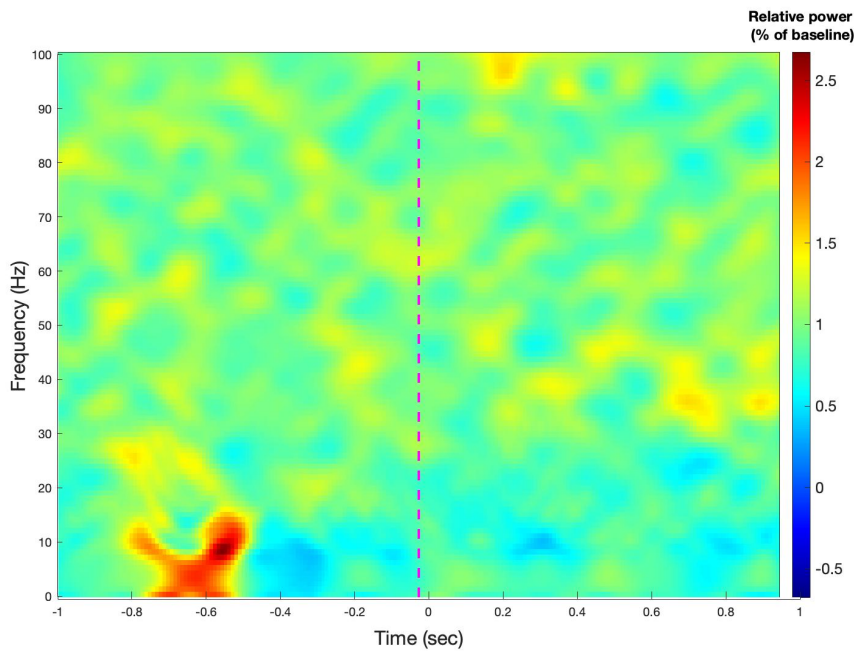
Figure 4.16: Time-frequency map from 45 trials EEG recorded from (a) tri-polar electrode and (b) conventional disc electrode in one subject. This time-frequency map calculated from EEG signals acquired during a real movement for thumb finger following the experimental paradigm described before.

4.6 Classification Results

Two classification algorithms were used in this study: LDA and ANNs. We chose these methods because we wanted to test which classification algorithm, linear (LDA) and nonlinear (ANNs), will yield to higher decoding accuracies for individual finger movements. In addition, we investigated two movement-related features, EEG temporal data and spectral features in EEG data, to discriminate individual fingers from one hand. Furthermore, we performed two statistical methods to evaluate the performance of decoding individual finger movements using these features. To evaluate the performance of decoding individual finger movements from each feature individually, we compared the classification accuracies obtained by each feature with the guess level (1/5 = 20%) using one-sample t-test. To further evaluate the decoding performance, we compared the decoding accuracies obtained by each pair of features using pairwise t-test. Moreover, the performance evaluation of the ANNs classifier and LDA classifier are examined using confusion matrices, which contain information about the true and predicted classifications performed by a classification algorithm and provides the common misclassifications in the classification of EEG signals.

Using temporal EEG and ERD/ERS features from individual frequency bands (i.e., α and β bands) as features, 80% of the data were selected as the training set and the remaining (20%) as the testing set. We first classified movements from resting conditions. Movement data and resting data were combined together with the corresponding labels for fingers. Figure 4.17 summarizes the decoding accuracies in discriminating movements from resting using α, β, and temporal EEG as features from tEEG (a) and cEEG (b). For the tEEG, the mean classification accuracy of movements from resting condition achieved by the temporal EEG feature is 84.83%. Spectral powers on the α and β bands achieved significantly lower classification accuracy than the temporal EEG feature, 75.27% and 76.65% respectively (p < 0.05, Table 4.5). For the cEEG, the mean classification accuracy of movements from resting condition achieved by the temporal EEG feature is 70.55%, followed by spectral powers for β at 70.23% and α at 66.62%. The classification accuracy achieved by spectral powers on the α and β bands are significantly lower than the temporal EEG

feature (p < 0.05, Table 4.6). Tables 4.5 and 4.6 also show that all features achieved significantly higher decoding accuracy than the guessing level (p < 0.05).

Table 4.5: Summary of t-test results on decoding accuracies from tEEG using different features, as well as the guess level (20%).

	Temporal data	Alpha band	Beta band	Guess level
Temporal data	—	0.0028	0.0068	9.30E-15
Alpha band	—	—	0.2859	3.89E-13
Beta band	—	—	—	5.22E-14

Table 4.6: Summary of t-test results on decoding accuracies from cEEG using different features, as well as the guess level (20%).

	Temporal data	Alpha band	Beta band	Guess level
Temporal data	—	0.0040	0.0046	2.170E-11
Alpha band	—	—	0.3456	1.20E-15
Beta band	—	—	—	6.45E-17

The results of five-class classification of the motor real and imagery EEG patterns corresponding to the right hand finger movements (thumb, index, middle, ring, and little fingers) of 13 subjects are presented in Figures 4.18, 4.19, 4.20, and 4.21. Tables 4.7 and 4.8 display the averaged decoding accuracies for each feature and for real and imagined finger movements classified by LDA and ANNs classifiers. The decoding accuracies were calculated from the confusion matrices as follows.

$$\text{Decoding accuracy} = \frac{\text{Correct predictions}}{\text{Total predictions}} \times 100 \tag{4.2}$$

The TCRE accuracy on average was higher than for the conventional disc electrode. This is because, as our results showed, the TCREs improve spatial resolution, SNR, and mutual information of the EEG signals compared to the conventional disc electrodes. The results suggest that with the TCRE we can achieve higher decoding accuracy for real movement if we use temporal EEG

data as feature with the ANNs classifier (70.04 ± 7.68%). Similarly, with the disc electrode, it achieved highest accuracy with temporal EEG data feature and ANNs (46.13 ± 6.77%). For the imaginary finger movements, using temporal EEG data with ANNs yielded the highest accuracy from TCRE (63.33 ± 5.79 %), and similar with disc electrode (34.03 ± 5.03%). The results also showed that ANNs classifier generated higher classification accuracy than the LDA classifier for both electrode systems and for the real and imagined finger movement, but with no statistically significant difference ($p > 0.05$).

When comparing confusion matrices from different features, the temporal EEG feature shows less confusions than the frequency-based features. Figure 4.18 shows the confusion matrices for real finger movement classifications using ANNs classifier. From the TCRE results shown in Figure 4.18, the most confused finger is the middle finger using the β band, the index finger using α band, and the little finger using temporal EEG data. From the disc electrode results (Figure 4.18, bottom), the little finger is most misclassified finger using temporal EEG data or α band, and the ring finger is the most confused finger using β band.

Similar phenomenon is also observed when using LDA classifier (Figure 4.19) with both TCRE and disc electrode. The misclassification occurred generally between the adjacent fingers (i.e., index vs. middle, ring vs. little). This indicates that the anatomical representation of the fingers are likely represented by overlapping neural activity. In addition, the results obtained by the TCREs when we use temporal data as feature show that there is some degree of independence between the decoded movements of the different fingers, in particular between the neighboring fingers. This suggests that different fingers movements are more distinguishable when using the temporal EEG data as feature.

The results also show that the decoding accuracies for most of the fingers with disc electrodes are close to the guessing level (i.e., 20%), especially for features from α and β bands. Moreover, the disc electrode results illustrate that thumb and middle are usually better classified than other fingers. Figures 4.20 and 4.21 show the results of classification of imagined fingers movements. Overall classification accuracies for imagined movement tended to be lower than for real move-

ment. The superior classification results for real movements is due to the fact that real movements generate stronger motor neural activity [112, 113]. However, some studies have shown that when the subjects are familiar with motor imagery, the classification results for imagined movements could be better than for real movements [114].

Table 4.7: Decoding accuracies results for different features used to decode real and imaginary fingers movements using TCRE.

Features	Real		Imaginary	
	ANNs	LDA	ANNs	LDA
Temporal data	70.04%	64.20%	63.33%	59.62%
Alpha band	55.57%	53.22%	54.56%	48.46%
Beta band	63.04%	56.38%	55.92%	51.50%

Table 4.8: Decoding accuracies results for different features used to decode real and imaginary fingers movements using disc electrode.

Features	Real		Imaginary	
	ANNs	LDA	ANNs	LDA
Temporal data	46.13%	34.15%	38.53%	34.03%
Alpha band	35.69%	31.3%	30.06%	27.03%
Beta band	31.36%	29.36%	26.70%	26.05%
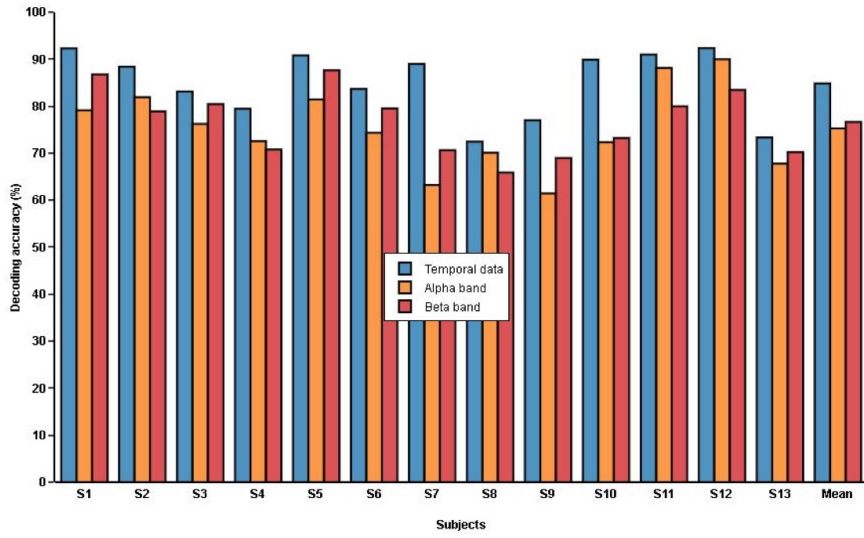
(a)
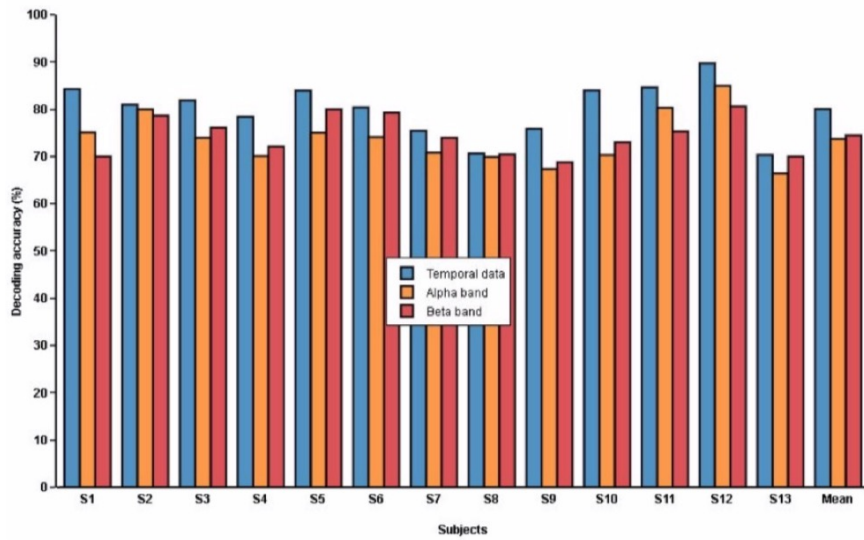
(b)

Figure 4.17: The accuracy in decoding movements from resting conditions using temporal data, α and β bands from tEEG (a) and cEEG (b).
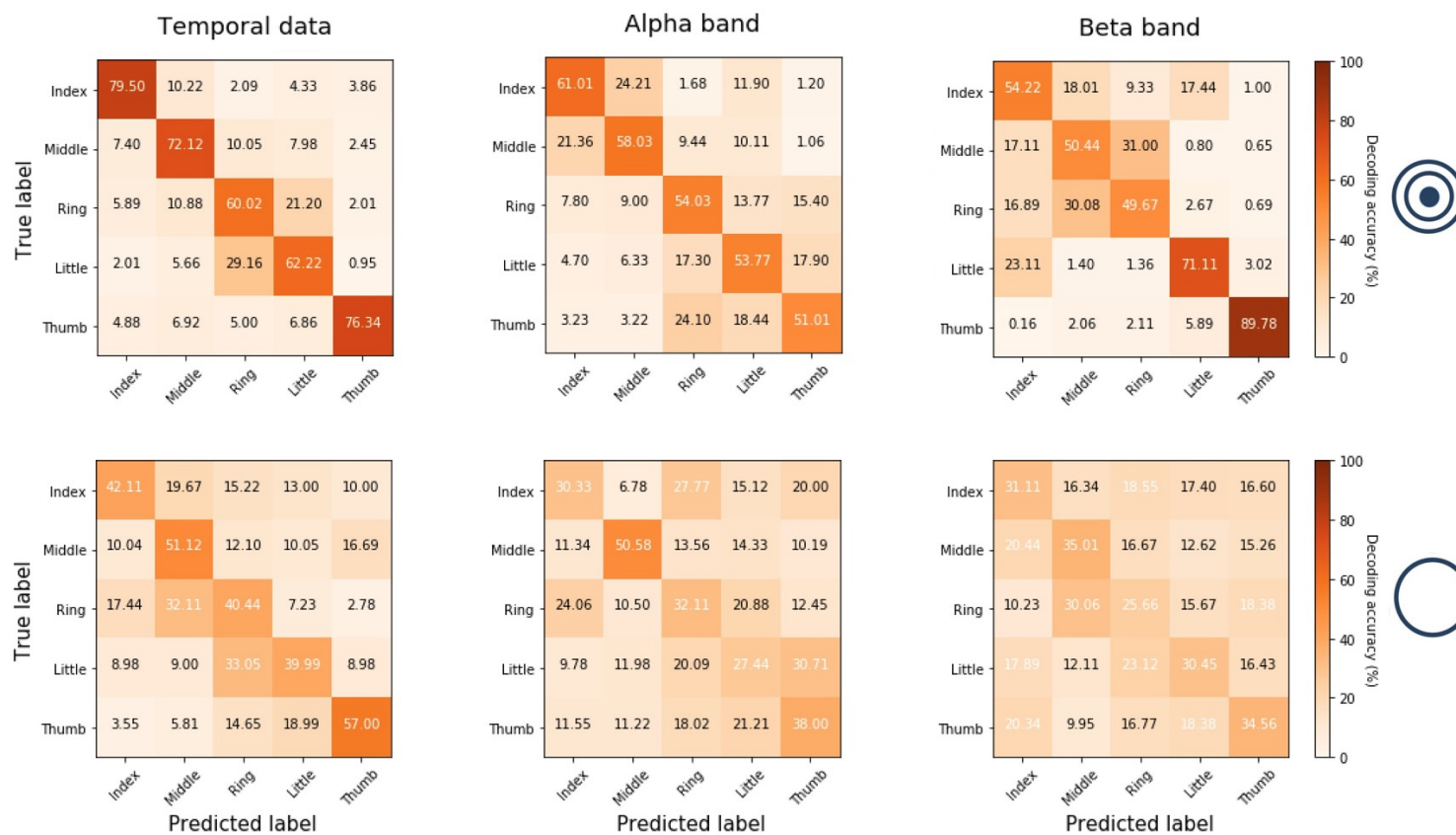
Figure 4.18: Confusion matrices of the **ANNs** classifier for classification of **real** fingers movements using temporal data, α, and β as features from TCRE (top) and disc electrode (below). Each row indicates true labels and each column indicates predicted labels.
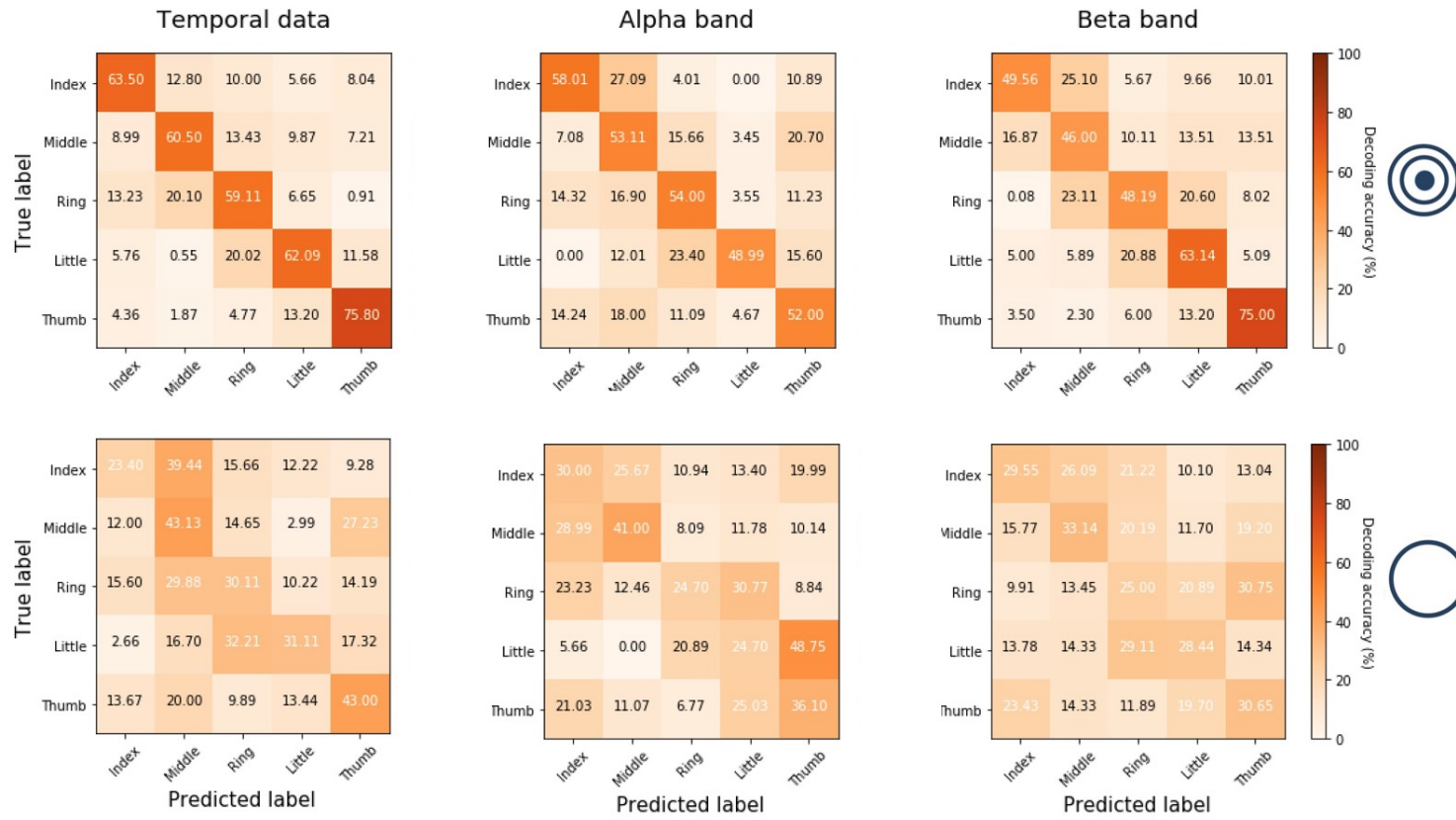
Figure 4.19: Confusion matrices of the **LDA** classifier for classification of **real** fingers movements using temporal data, α, and β as features from TCRE (top) and disc electrode (below). Each row indicates true labels and each column indicates predicted labels.

Figure 4.20: Confusion matrices of the **ANNs** classifier for classification of **imagined** fingers movements using temporal data, α, and β as features from TCRE (top) and disc electrode (below). Each row indicates true labels and each column indicates predicted labels.

Figure 4.21: Confusion matrices of the **LDA** classifier for classification of **imagined** finger movement decoding using temporal data, α, and β as features from TCRE (top) and disc electrode (below). Each row indicates true labels and each column indicates predicted labels.
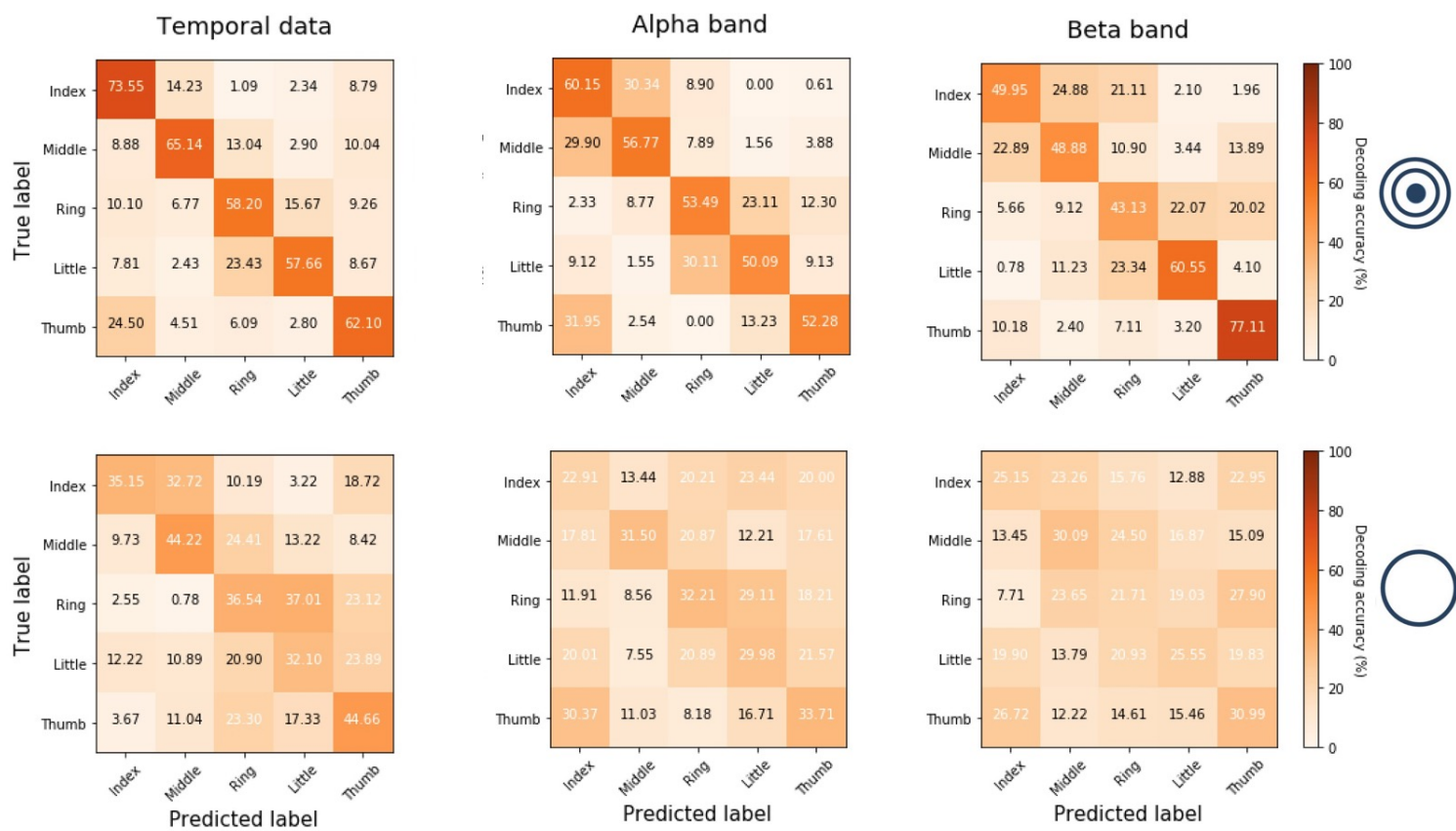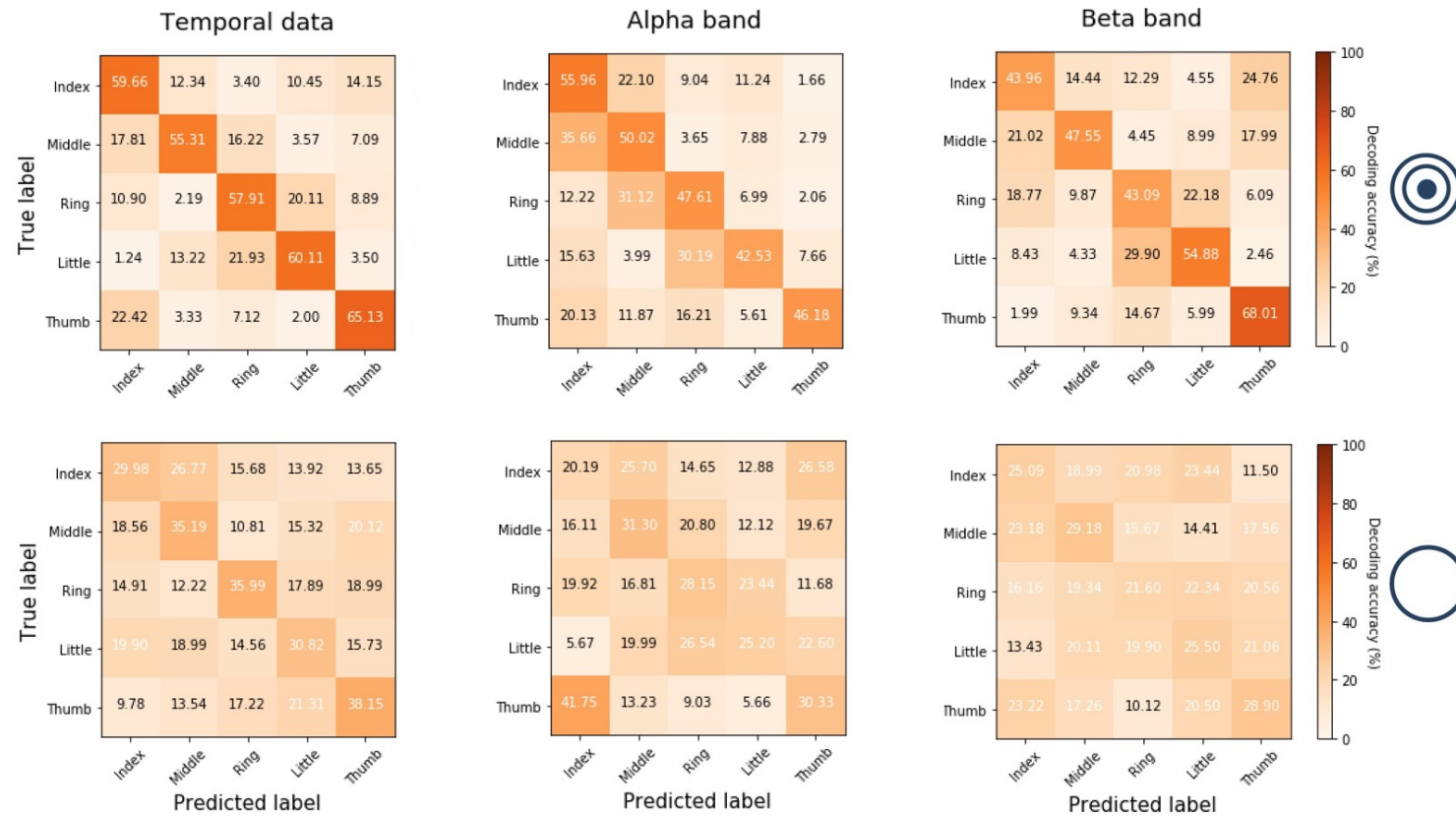
Chapter 5

Conclusion and Future Works

The purpose of this study was to decode real and imaginary finger movements with brain activity acquired via non-invasive EEG. We investigated how well real and imaginary finger movements can be decoded from scalp EEG signals using two different electrode systems: tri-polar concentric ring electrodes and conventional disc electrodes. The successful decoding of finger movements can provide extra degrees of freedom to drive brain computer interface (BCI) applications, especially for neurorehabilitation.

The results show that the TCRE EEG (tEEG) provides approximately a four times enhancement in the SNR compared to disc electrode signals. In addition, we evaluated the interdependency level between neighboring electrodes from tri-polar, disc, and disc with Hjorth's Laplacian method in time and frequency domains by calculating the mutual information (MI) and coherence. The MRP signals recorded with the TCRE system have significantly less MI between electrodes than the conventional disc electrode system and disc electrodes with Hjorth's Laplacian method. Also, the results show that the mean coherence between neighboring tri-polar electrodes was found to be significantly smaller than disc electrode and disc electrode with Hjorth's method, especially at higher frequencies. This lower coherence in the high frequency band between neighboring tri-polar electrodes suggests that the TCREs may record a more localized neuronal activity.

Due to the limitation of the numbers of the TCREs we currently have, we used different montages to record from different part of the brain. The first electrode placement was done by attaching all four TCREs above sensorimotor area on the contralateral cortex. We also recorded from the ipsilateral area (C4 site) and compared the result with the contralateral area (C3 site). We found that the contralateral finger movements produced more pronounced MRP compared with ipsilateral finger movements. This result suggests the possibility of decoding both contralateral finger movements from the ipsilateral side of the brain, and this has a great impact in the BCI, in particu-

80

lar for stroke patients. The last montage we used was to apply the Hjorth's Laplacian on the signal recorded from the outer ring.

To decode different real and imagined fingers movements, we extracted two features from the EEG signals. The first feature is the temporal EEG data, and the second feature is the spectral powers in α and β bands. We compared two classification algorithms: LDA and ANNs. The highest average decoding accuracy of 5-class classification for real movements was 70.04% when we used temporal EEG data as feature and classified it using ANNs. For the imaginary movements, the highest average decoding accuracy of 5-class classification was 63.33% when we used temporal EEG data as feature and classify it using ANNs as well.

This work has a lot of scope for improvement in the future in order to design a BCI application with high reliability using non-invasive EEG. Firstly, it will be interesting to record with TCREs from different areas on the scalp to investigate the behavior of the MRPs at different locations. In the future , these recordings should be repeated with more locations recorded concurrently. Additionally, with future improvement of the TCREs design, such as designing micro-TCREs, we can record even more localized brain signals and hence decode different finger movements with higher accuracy. This hypothesis is based on an ECoG study, where the authors compared between regular-ECoG and micro-ECoG grids and they found that with the micro-ECoG grid they could obtain signals with higher spatial and temporal resolution than with the regular-ECoG grid [101]. Additionally, we are planning to implement a cross-subject classifier, where the classifier is trained across group of subjects and tested on one subject. Currently, the standard practice is to build a new classifier for each subject. This requires more training time for each subject, and it might even be necessary to train the classifier every day for the same subject [115]. We will compare between the classifier performance when it is trained on multiple subjects versus on individual subjects.

To further increase the classification accuracy, we will apply the common spatial pattern (CSP) on EEG data. The goal of CSP is to find spatial filters that optimally capture modulations of brain rhythms. The idea of CSP is to find spatial filters such that the filtered signal is maximal for one class and minimal for the other class [116]. Formally, given per-class average covariance matrices

$\sum_c$, find the simultaneous diagonalizer V of $\sum_{n-1}$ and $\sum_{n+1}$:

$$V^T \Sigma_{n-1} V = D_{-1} \tag{5.1}$$

$$V^T \Sigma_{n+1} V = D_{+1} \tag{5.2}$$

for diagonal D_{-1} and D_{+1} such that $D_{+1} + D_{+1} = I$. This yields a generalized eigenvalue problem of the form:

$$V^T \Sigma_{-1} V = D \Lambda V^T (\Sigma_{-1} + \Sigma_{+1}) V = I \tag{5.3}$$

The k smallest and largest eigenvalues in D correspond to k leftmost/rightmost columns in V (spatial filters) that yield smallest (largest) variance in class -1 and simultaneously largest (smallest) variance in class +1.

Planned future work in this study includes the implementation of EEG source localization techniques to identify areas associated with different fingers movements. The aim of the EEG source localization techniques is visualize the effective EEG sources on the subject's brain surface. In order to do that, we need to solve the inverse and forward problems of EEG. The forward problem can be computed given the geometry of the brain/skull/skin compartments, the conductivities of different tissue types, and the electrode positions. We solve the inverse problem by solving many forward problems. The mathematical steps for solving the inverse problem are as follow. If we represent the scalp recorded potentials by X, the current density by S, and the volume conductor model by L, the inverse problem refers to finding S given known X. This can be solved by solving the following minimization problem.

$$min||X - LS||^2 \tag{5.4}$$

The minimization problem will give us many solutions; therefore, we need to apply some constraints to constrain the sources. When we solve the minimization problem correctly, we will have correct source localization.

The main goal of BCI work is to enable people with neural pathways that have been damaged by any type of diseases to better control their environment. The potential for meeting this goal can be demonstrated by controlling the fingers of a robotic grippe by translating the EEG signals recorded by TCREs into movement commands. This can be done by using simple and inexpensive components such as Arduino, optocouplers, and 3D-printed robotic arm. Our study shows promising results for the use of brain signals recorded from the scalp using TCREs to be used in controlling five individual fingers of a robotic prosthetic hand successfully.

Bibliography

[1]   Hiroshi Shibasaki and Mark Hallett. What is the Bereitschaftspotential? *Clinical Neurophysiology*, 117(11):2341–2356, 2006.

[2]   Jonathan R Wolpaw, Niels Birbaumer, Dennis J McFarland, Gert Pfurtscheller, and Theresa M Vaughan. Brain–computer interfaces for communication and control. *Clinical Neurophysiology*, 113(6):767–791, 2002.

[3]   Anirudh Vallabhaneni, Tao Wang, and Bin He. Brain–computer interface. *Neural Engineering*, pages 85–121, 2005.

[4]   Trent J Bradberry, Rodolphe J Gentili, and José L Contreras-Vidal. Reconstructing three-dimensional hand movements from noninvasive electroencephalographic signals. *Journal of Neuroscience*, 30(9):3432–3437, 2010.

[5]   Luis Fernando Nicolas-Alonso and Jaime Gomez-Gil. Brain computer interfaces, a review. *Sensors*, 12(2):1211–1279, 2012.

[6]   Febo Cincotti, Donatella Mattia, Fabio Aloise, Simona Bufalari, Laura Astolfi, Fabrizio De Vico Fallani, Andrea Tocci, Luigi Bianchi, Maria Grazia Marciani, Shangkai Gao, et al. High-resolution EEG techniques for brain–computer interface applications. *Journal of Neuroscience Methods*, 167(1):31–42, 2008.

[7]   Klaus-Robert Müller, Benjamin Blankertz, Gabriel Curio, et al. Machine learning and signal processing tools for BCI. In *BBCI Workshop: Advances in Neurotechnologies, Berlin 2009*, 2009.

[8]   Niels Birbaumer. Brain–computer-interface research: coming of age. *Clinical Neurophysiology*, 479–83, 2006.

[9]   Gopal Santhanam, Stephen I Ryu, M Yu Byron, Afsheen Afshar, and Krishna V Shenoy. A high-performance brain–computer interface. *Nature*, 442(7099):195, 2006.

[10] Yuanqing Li, Jinyi Long, Tianyou Yu, Zhuliang Yu, Chuanchu Wang, Haihong Zhang, and Cuntai Guan. An EEG-based BCI system for 2-D cursor control by combining Mu/Beta rhythm and P300 potential. *IEEE Transactions on Biomedical Engineering*, 57(10):2495–2505, 2010.

[11] Gernot R Muller-Putz and Gert Pfurtscheller. Control of an electrical prosthesis with an SSVEP-based BCI. *IEEE Transactions on Biomedical Engineering*, 55(1):361–364, 2008.

[12] Lawrence Ashley Farwell and Emanuel Donchin. Talking off the top of your head: toward a mental prosthesis utilizing event-related brain potentials. *Electroencephalography and Clinical Neurophysiology*, 70(6):510–523, 1988.

[13] Gert Pfurtscheller and FH Lopes Da Silva. Event-related EEG/MEG synchronization and desynchronization: basic principles. *Clinical Neurophysiology*, 110(11):1842–1857, 1999.

[14] Gert Pfurtscheller and Christa Neuper. Motor imagery and direct brain-computer communication. *Proceedings of the IEEE*, 89(7):1123–1134, 2001.

[15] Tobias Egner and John H Gruzelier. EEG biofeedback of low beta band components: frequency-specific effects on variables of attention and event-related brain potentials. *Clinical Neurophysiology*, 115(1):131–139, 2004.

[16] Dean J Krusienski, Eric W Sellers, Dennis J McFarland, Theresa M Vaughan, and Jonathan R Wolpaw. Toward enhanced P300 speller performance. *Journal of Neuroscience Methods*, 167(1):15–21, 2008.

[17] Heidi Johansen-Berg, Matthew FS Rushworth, Marko D Bogdanovic, Udo Kischka, Sunil Wimalaratna, and Paul M Matthews. The role of ipsilateral premotor cortex in hand movement after stroke. *Proceedings of the National Academy of Sciences*, 99(22):14518–14523, 2002.

[18] Niels Birbaumer and Leonardo G Cohen. Brain–computer interfaces: communication and restoration of movement in paralysis. *The Journal of Physiology*, 579(3):621–636, 2007.

[19] Herbert Ramoser, Johannes Muller-Gerking, and Gert Pfurtscheller. Optimal spatial filtering of single trial EEG during imagined hand movement. *IEEE Transactions on Rehabilitation Engineering*, 8(4):441–446, 2000.

[20] Leigh R Hochberg, Daniel Bacher, Beata Jarosiewicz, Nicolas Y Masse, John D Simeral, Joern Vogel, Sami Haddadin, Jie Liu, Sydney S Cash, Patrick van der Smagt, et al. Reach and grasp by people with tetraplegia using a neurally controlled robotic arm. *Nature*, 485(7398):372–375, 2012.

[21] Jonathan R Wolpaw and Dennis J McFarland. Control of a two-dimensional movement signal by a noninvasive brain-computer interface in humans. *Proceedings of the National Academy of Sciences of the United States of America*, 101(51):17849–17854, 2004.

[22] Ying Gu, Kim Dremstrup, and Dario Farina. Single-trial discrimination of type and speed of wrist movements from EEG recordings. *Clinical Neurophysiology*, 120(8):1596–1600, 2009.

[23] Alexander J Doud, John P Lucas, Marc T Pisansky, and Bin He. Continuous three-dimensional control of a virtual helicopter using a motor imagery based brain-computer interface. *PloS one*, 6(10):e26322, 2011.

[24] Jie Zhou, Jun Yao, Jie Deng, and Julius PA Dewald. EEG-based classification for elbow versus shoulder torque intentions involving stroke subjects. *Computers in Biology and Medicine*, 39(5):443–452, 2009.

[25] JOJWGSJ Kubanek, KJ Miller, JG Ojemann, JR Wolpaw, and G Schalk. Decoding flexion of individual fingers using electrocorticographic signals in humans. *Journal of Neural Engineering*, 6(6):066001, 2009.

[26] Soumyadipta Acharya, Matthew S Fifer, Heather L Benz, Nathan E Crone, and Nitish V Thakor. Electrocorticographic amplitude predicts finger positions during slow grasping motions of the hand. *Journal of Neural Engineering*, 7(4):046002, 2010.

[27] Amna Javed, Mohsin I Tiwana, Moazzam I Tiwana, Nasir Rashid, Javaid Iqbal, and Umar Shahbaz Khan. Recognition of finger movements using EEG signals for control of upper limb prosthesis using logistic regression. *Biomedical Research*, 28(17), 2017.

[28] Ke Liao, Ran Xiao, Jania Gonzalez, and Lei Ding. Decoding individual finger movements from one hand using human EEG signals. *PloS one*, 9(1):e85192, 2014.

[29] Benoit Cottereau, Karim Jerbi, and Sylvain Baillet. Multiresolution imaging of MEG cortical sources using an explicit piecewise model. *NeuroImage*, 38(3):439–451, 2007.

[30] K Kurata and SP Wise. Premotor and supplementary motor cortex in rhesus monkeys: neuronal activity during externally-and internally-instructed motor tasks. *Experimental Brain Research*, 72(2):237–248, 1988.

[31] Hajime Mushiake, Masahiko Inase, and Jun Tanji. Neuronal activity in the primate premotor, supplementary, and precentral motor cortex during visually guided and internally determined sequential movements. *Journal of Neurophysiology*, 66(3):705–718, 1991.

[32] Walter G Besio. Biomedical electrode for detecting localized electrical signals and providing electrical stimulation, January 8 2013. US Patent 8,352,012.

[33] W Besio, R Aakula, K Koka, and W Dai. Development of a tri-polar concentric ring electrode for acquiring accurate Laplacian body surface potentials. *Annals of Biomedical Engineering*, 34(3):426–435, 2006.

[34] Kanthaiah Koka and Walter G Besio. Improvement of spatial selectivity and decrease of mutual information of tri-polar concentric ring electrodes. *Journal of Neuroscience Methods*, 165(2):216–222, 2007.

[35] Marjan Jahanshahi and Mark Hallett. *The Bereitschaftspotential: Movement-related cortical potentials*. Springer Science & Business Media, 2003.

[36] Ernest Nlandu Kamavuako, Mads Jochumsen, Imran Khan Niazi, and Kim Dremstrup. Comparison of features for movement prediction from single-trial movement-related cortical potentials in healthy subjects and stroke patients. *Computational Intelligence and Neuroscience*, 2015:71, 2015.

[37] Dennis J McFarland, Lynn M McCane, Stephen V David, and Jonathan R Wolpaw. Spatial filter selection for EEG-based communication. *Electroencephalography and Clinical Neurophysiology*, 103(3):386–394, 1997.

[38] F Babiloni, F Cincotti, L Lazzarini, J Millan, J Mourino, M Varsta, J Heikkonen, L Bianchi, and MG Marciani. Linear classification of low-resolution EEG patterns produced by imagined hand movements. *IEEE Transactions on Rehabilitation Engineering*, 8(2):186–188, 2000.

[39] Shang-Ming Zhou, John Q Gan, and Francisco Sepulveda. Classifying mental tasks based on features of higher-order statistics from EEG signals in brain–computer interface. *Information Sciences*, 178(6):1629–1640, 2008.

[40] M Bishop Christopher. *Pattern recognition and machine learning.* Springer-Verlag New York, 2016.

[41] Chuck Anderson. Lecture notes in CS545 machine learning, Fall semester 2014.

[42] Mikhail A Lebedev and Miguel AL Nicolelis. Brain–machine interfaces: past, present and future. *TRENDS in Neurosciences*, 29(9):536–546, 2006.

[43] Dirk Hagemann, Ewald Naumann, and Julian F Thayer. The quest for the EEG reference revisited: a glance from brain asymmetry research. *Psychophysiology*, 38(5):847–857, 2001.

[44] Claudio Carvalhaes and J Acacio de Barros. The surface Laplacian technique in EEG: Theory and methods. *International Journal of Psychophysiology*, 97(3):174–188, 2015.

[45] Bin He. Brain electric source imaging: scalp Laplacian mapping and cortical imaging. *Critical Reviews in Biomedical Engineering*, 27(3-5):149–188, 1999.

[46] Bo Hjorth. An on-line transformation of EEG scalp potentials into orthogonal source derivations. *Electroencephalography and Clinical Neurophysiology*, 39(5):526–530, 1975.

[47] Francois Perrin, Olivier Bertrand, and Jacques Pernier. Scalp current density mapping: value and estimation from potential data. *IEEE Transactions on Biomedical Engineering*, BME-34(4):283–288, 1987.

[48] Samuel K Law, Paul L Nunez, and Ranjith S Wijesinghe. High-resolution EEG using spline generated surface Laplacians on spherical and ellipsoidal surfaces. *IEEE Transactions on Biomedical Engineering*, 40(2):145–153, 1993.

[49] Bin He, Jie Lian, and Guanglin Li. High-resolution EEG: a new realistic geometry spline Laplacian estimation technique. *Clinical Neurophysiology*, 112(5):845–852, 2001.

[50] Leon Lapidus and George F Pinder. *Numerical solution of partial differential equations in science and engineering*. John Wiley & Sons, 2011.

[51] Kanthaiah Besio, Koka, Rajesh Aakula, and Weizhong Dai. Tri-polar concentric ring electrode development for Laplacian electroencephalography. *IEEE Transactions on Biomedical Engineering*, 53(5):926–933, 2006.

[52] Walter G Besio, Hongbao Cao, and Peng Zhou. Application of tripolar concentric electrodes and prefeature selection algorithm for brain–computer interface. *IEEE Transactions on Neural Systems and Rehabilitation Engineering*, 16(2):191–194, 2008.

[53] William D Penny, Stephen J Roberts, Eleanor A Curran, and Maria J Stokes. EEG-based communication: a pattern recognition approach. *IEEE Transactions on Rehabilitation Engineering*, 8(2):214–215, 2000.

[54] F Cincotti, D Mattia, C Babiloni, F Carducci, L Bianchi, Millán del RJ, J Mourino, S Salinari, MG Marciani, and F Babiloni. Classification of EEG mental patterns by using two scalp electrodes and Mahalanobis distance-based classifiers. *Methods of Information in Medicine*, 41(04):337–341, 2002.

[55] Walter G Besio, Karen N Gale, and Andrei V Medvedev. Possible therapeutic effects of transcutaneous electrical stimulation via concentric ring electrodes. *Epilepsia*, 51(s3):85–87, 2010.

[56] X Liu and W Besio. Comparisons of the spatial resolution between disc and tripolar concentric ring electrodes. *Proceedings of the Fifth International Brain–Computer Interface Meeting: Defining the Future, Pacific Grove, California*, page 2, 2013.

[57] B Neil Cuffin and David Cohen. Comparison of the magnetoencephalogram and electroencephalogram. *Electroencephalography and Clinical Neurophysiology*, 47(2):132–146, 1979.

[58] Veikko Suihko and Jaakko Malmivuo. Half-sensitivity volumes in EEG and MEG measurements. In *Proceedings of the Second Ragnar Granit Symposium: EEG and MEG Signal Analysis and Interpretation*, pages 22–23, 1993.

[59] Walter G Besio, Iris E Martínez-Juárez, Oleksandr Makeyev, John N Gaitanis, Andrew S Blum, Robert S Fisher, and Andrei V Medvedev. High-frequency oscillations recorded on the scalp of patients with epilepsy using tripolar concentric ring electrodes. *IEEE Journal of Translational Engineering in Health and Medicine*, 2, 2014.

[60] Y Boudria, X Liu, A Feltane, and W Besio. One-dimensional imaginary movement cursor Control using disc and tripolar electrodes. *Proceedings of the Fifth International Brain–Computer Interface Meeting: Defining the Future, Pacific Grove, California*, page 2, 2013.

[61] Aqsa Shakeel, Muhammad Samran Navid, Muhammad Nabeel Anwar, Suleman Mazhar, Mads Jochumsen, and Imran Khan Niazi. A review of techniques for detection of move-

ment intention using movement-related cortical potentials. *Computational and Mathematical Methods in Medicine*, 2015, 2015.

[62] Hans H Kornhuber and Lüder Deecke. Hirnpotentialänderungen bei willkürbewegungen und passiven bewegungen des menschen: Bereitschaftspotential und reafferente Potentiale. *Pflüger's Archiv für die gesamte Physiologie des Menschen und der Tiere*, 284(1):1–17, 1965.

[63] Akio Ikeda, Hiroshi Shibasaki, Ryuji Kaji, Kiyohito Terada, Takashi Nagamine, Manabu Honda, and Jun Kimura. Dissociation between contingent negative variation (CNV) and Bereitschaftspotential (BP) in patients with parkinsonism. *Electroencephalography and Clinical Neurophysiology*, 102(2):142–151, 1997.

[64] Akio Ikeda, Hans O Lüders, Richard C Burgess, and Hiroshi Shibasaki. Movement-related potentials recorded from supplementary motor area and primary motor area: role of supplementary motor area in voluntary movements. *Brain*, 115(4):1017–1043, 1992.

[65] W Grey Walter. Contingent negative variation: an electric sign of sensori-motor association and expectancy in the human brain. *Nature*, 230:380–384, 1964.

[66] John W Rohrbaugh, Karl Syndulko, and Donald B Lindsley. Brain wave components of the contingent negative variation in humans. *Science*, 191(4231):1055–1057, 1976.

[67] Chioulian Lai, Akio Ikeda, Kiyohito Terada, Takashi Nagamine, Manabu Honda, Xiaoping Xu, Nahoko Yoshimura, Shenglong Howng, Geoff Barrett, and Hiroshi Shibasaki. Event-related potentials associated with judgment: comparison of S1-and S2-choice conditions in a contingent negative variation (CNV) paradigm. *Journal of Clinical Neurophysiology*, 14(5):394–405, 1997.

[68] Ming-Kuei Lu, Noritoshi Arai, Chon-Haw Tsai, and Ulf Ziemann. Movement related cortical potentials of cued versus self-initiated movements: Double dissociated modulation by

dorsal premotor cortex versus supplementary motor area rTMS. *Human Brain Mapping*, 33(4):824–839, 2012.

[69] Dale W McAdam, John R Knott, and Charles S Rebert. Cortical slow potential changes in man related to interstimulus interval and to pre trial prediction of interstimulus interval. *Psychophysiology*, 5(4):349–358, 1969.

[70] Wikipedia. Contingent negative variation — Wikipedia, the free encyclopedia. http://en.wikipedia.org/w/index.php?title=Contingent%20negative%20variation&oldid=886614784, 2019. [Online; accessed 12-January-2018].

[71] JAV Bates. Electrical activity of the cortex accompanying movement. *The Journal of Physiology*, 113(2-3):240–257, 1951.

[72] Tobias Pistohl, Tonio Ball, Andreas Schulze-Bonhage, Ad Aertsen, and Carsten Mehring. Prediction of arm movement trajectories from ECoG-recordings in humans. *Journal of Neuroscience Methods*, 167(1):105–114, 2008.

[73] Wei Wang, Gustavo P Sudre, Yang Xu, Robert E Kass, Jennifer L Collinger, Alan D Degenhart, Anto I Bagic, and Douglas J Weber. Decoding and cortical source localization for intended movement direction with MEG. *Journal of Neurophysiology*, 104(5):2451–2461, 2010.

[74] Justin Baker, William Bishop, Spencer Kellis, Todd Levy, and Paul House. Multi-scale recordings for neuroprosthetic control of finger movements. In *Engineering in Medicine and Biology Society, 2009. EMBC 2009. Annual International Conference of the IEEE*, pages 4573–4577. IEEE, 2009.

[75] Vikram Aggarwal, Mohsen Mollazadeh, Adam G Davidson, Marc H Schieber, and Nitish V Thakor. State-based decoding of hand and finger kinematics using neuronal ensemble and LFP activity during dexterous reach-to-grasp movements. *Journal of Neurophysiology*, 109(12):3067–3081, 2013.

[76] Vladimir Litvak, Alexandre Eusebio, Ashwani Jha, Robert Oostenveld, Gareth R Barnes, William D Penny, Ludvic Zrinzo, Marwan I Hariz, Patricia Limousin, Karl J Friston, et al. Optimized beamforming for simultaneous MEG and intracranial local field potential recordings in deep brain stimulation patients. *Neuroimage*, 50(4):1578–1588, 2010.

[77] Reinhold Scherer, Stavros P Zanos, Kai J Miller, Rajesh PN Rao, and Jeffrey G Ojemann. Classification of contralateral and ipsilateral finger movements for electrocorticographic brain-computer interfaces. *Neurosurgical Focus*, 27(1):E12, 2009.

[78] Rémi Flamary and Alain Rakotomamonjy. Decoding finger movements from ECoG signals using switching linear models. *Frontiers in Neuroscience*, 6:29, 2012.

[79] KJ Miller, S Zanos, EE Fetz, M Den Nijs, and JG Ojemann. Decoupling the cortical power spectrum reveals real-time representation of individual finger movements in humans. *Journal of Neuroscience*, 29(10):3132–3137, 2009.

[80] Marc H Schieber and Lyndon S Hibbard. How somatotopic is the motor cortex hand area? *Science*, 261(5120):489–492, 1993.

[81] Soheila Samiee, Sepideh Hajipour, and Mohammad Bagher Shamsollahi. Five-class finger flexion classification using ECoG signals. In *2010 International Conference on Intelligent and Advanced Systems (ICIAS)*, pages 1–4. IEEE, 2010.

[82] LA Stankevich, KM Sonkin, NV Shemyakina, Zh V Nagornova, Ju G Khomenko, DS Perets, and AV Koval. EEG pattern decoding of rhythmic individual finger imaginary movements of one hand. *Human Physiology*, 42(1):32–42, 2016.

[83] Tetsuro Hayashi, Hiroshi Yokoyama, Isao Nambu, and Yasuhiro Wada. Prediction of individual finger movements for motor execution and imagery: An EEG study. In *2017 IEEE International Conference on Systems, Man, and Cybernetics (SMC)*, pages 3020–3023. IEEE, 2017.

[84] Vladimir Cerny and Jakub Stastny. Application of common spatial patterns on classification of right hand finger movements from EEG signal. *Computational Intelligence and Neuroscience*, 5(3):31–35, 2014.

[85] ST Microelectronics. *LIS3DH: MEMS digital output motion sensor ultra low-power high performance 3-axes "nano" accelerometer*, 21, May, 2010. Rev. 1.

[86] Oleksandr Makeyev, Yacine Boudria, Zhenghan Zhu, Thomas Lennon, and Walter G Besio. Emulating conventional disc electrode with the outer ring of the tripolar concentric ring electrode in phantom and human electroencephalogram data. In *2013 IEEE Signal Processing in Medicine and Biology Symposium (SPMB)*, pages 1–4. IEEE, 2013.

[87] Aysegul Gunduz, Peter Brunner, Mohit Sharma, Eric C Leuthardt, Anthony L Ritaccio, Bijan Pesaran, and Gerwin Schalk. Differential roles of high gamma and local motor potentials for movement preparation and execution. *Brain-Computer Interfaces*, 3(2):88–102, 2016.

[88] Arnaud Delorme and Scott Makeig. EEGLAB: an open source toolbox for analysis of single-trial EEG dynamics including independent component analysis. *Journal of Neuroscience Methods*, 134(1):9–21, 2004.

[89] K Okano and J Tanji. Neuronal activities in the primate motor fields of the agranular frontal cortex preceding visually triggered and self-paced movement. *Experimental Brain Research*, 66(1):155–166, 1987.

[90] Keisetsu Shima and Jun Tanji. Neuronal activity in the supplementary and presupplementary motor areas for temporal organization of multiple movements. *Journal of Neurophysiology*, 84(4):2148–2160, 2000.

[91] Catherine Disselhorst-Klug, Jiri Silny, and Gunter Rau. Improvement of spatial resolution in surface-EMG: a theoretical and experimental comparison of different spatial filters. *IEEE Transactions on Biomedical Engineering*, 44(7):567–574, 1997.

[92] Claude Elwood Shannon. A mathematical theory of communication. *Bell System Technical Journal*, 27(3):379–423, 1948.

[93] Alexander Kraskov, Harald Stögbauer, and Peter Grassberger. Estimating mutual information. *Physical Review E*, 69(6):066138, 2004.

[94] W Besio and K Koka. Mutual information of tri-polar concentric ring electrodes. In *Engineering in Medicine and Biology Society, 2006. EMBS'06. 28th Annual International Conference of the IEEE*, pages 1106–1109. IEEE, 2006.

[95] C Tandonnet, Boris Burle, T Hasbroucq, and F Vidal. Spatial enhancement of EEG traces by surface Laplacian estimation: comparison between local and global methods. *Clinical Neurophysiology*, 116(1):18–24, 2005.

[96] DM MacKay. On-line source-density computation with a minimum of electrons. *Electroencephalography and Clinical Neurophysiology*, 56(6):696–698, 1983.

[97] Pascaline Personnier, Yves Ballay, and Charalambos Papaxanthis. Mentally represented motor actions in normal aging: Iii. Electromyographic features of imagined arm movements. *Behavioural Brain Research*, 206(2):184–191, 2010.

[98] Estelle Raffin, Jérémie Mattout, Karen T Reilly, and Pascal Giraux. Disentangling motor execution from motor imagery with the phantom limb. *Brain*, 135(2):582–595, 2012.

[99] Ling E Wang, Marc Tittgemeyer, Davide Imperati, Svenja Diekhoff, Mitra Ameli, Gereon R Fink, and Christian Grefkes. Degeneration of corpus callosum and recovery of motor function after stroke: a multimodal magnetic resonance imaging study. *Human Brain Mapping*, 33(12):2941–2956, 2012.

[100] Walter G Besio, Xiang Liu, Liling Wang, Andrei V Medvedev, and Kanthaiah Koka. Transcutaneous focal electrical stimulation via concentric ring electrodes reduces synchrony induced by pentylenetetrazole in beta and gamma bands in rats. *International Journal of Neural Systems*, 21(02):139–149, 2011.

[101] Wei Wang, Alan D Degenhart, Jennifer L Collinger, Ramana Vinjamuri, Gustavo P Sudre, P David Adelson, Deborah L Holder, Eric C Leuthardt, Daniel W Moran, Michael L Boninger, et al. Human motor cortical activity recorded with Micro-ECoG electrodes, during individual finger movements. In *Engineering in Medicine and Biology Society, 2009. EMBC 2009. Annual International Conference of the IEEE*, pages 586–589. IEEE, 2009.

[102] Kai J Miller, Eric C Leuthardt, Gerwin Schalk, Rajesh PN Rao, Nick Anderson, Dan Moran, Jeffrey G Ojemann, Wadsworth Institute, and Kai J Miller. Electrocorticographic spectral changes with motor movement. *J Neurosci*, 2007.

[103] Gert Pfurtscheller and W Klimesch. Functional topography during a visuoverbal judgment task studied with event-related desynchronization mapping. *Journal of Clinical Neurophysiology: official publication of the American Electroencephalographic Society*, 9(1):120–131, 1992.

[104] Wim van Winsun, Joseph Sergeant, and Reint Geuze. The functional significance of event-related desynchronization of alpha rhythm in attentional and activating tasks. *Electroencephalography and Clinical Neurophysiology*, 58(6):519–524, 1984.

[105] R Brechet and R Lecasble. Reactivity of mu rhythm to flicker. *Electroencephalography and Clinical Neurophysiology*, 18(7):721, 1965.

[106] Y Koshino and E Niedermeyer. Enhancement of rolandic mu-rhythm by pattern vision. *Electroencephalography and Clinical Neurophysiology*, 38(5):535–538, 1975.

[107] Nathan E Crone, Diana L Miglioretti, Barry Gordon, and Ronald P Lesser. Functional mapping of human sensorimotor cortex with electrocorticographic spectral analysis. ii. Event-related synchronization in the gamma band. *Brain: A Journal of Neurology*, 121(12):2301–2315, 1998.

[108] P Derambure, L Defebvre, K Dujardin, JL Bourriez, JM Jacquesson, A Destee, and JD Guieu. Effect of aging on the spatio-temporal pattern of event-related desynchronization

during a voluntary movement. *Electroencephalography and Clinical Neurophysiology/E-voked Potentials Section*, 89(3):197–203, 1993.

[109] Hai Sun, Timothy M Blakely, Felix Darvas, Jeremiah D Wander, Lise A Johnson, David K Su, Kai J Miller, Eberhard E Fetz, and Jeffery G Ojemann. Sequential activation of premotor, primary somatosensory and primary motor areas in humans during cued finger movements. *Clinical Neurophysiology*, 126(11):2150–2161, 2015.

[110] Mariana P Branco, Zachary V Freudenburg, Erik J Aarnoutse, Martin G Bleichner, Mariska J Vansteensel, and Nick F Ramsey. Decoding hand gestures from primary so-matosensory cortex using high-density ECoG. *Neuroimage*, 147:130–142, 2017.

[111] Venkatesh N Murthy and Eberhard E Fetz. Coherent 25-to 35-Hz oscillations in the sen-sorimotor cortex of awake behaving monkeys. *Proceedings of the National Academy of Sciences*, 89(12):5670–5674, 1992.

[112] Valerie Morash, Ou Bai, Stephen Furlani, Peter Lin, and Mark Hallett. Classifying EEG sig-nals preceding right hand, left hand, tongue, and right foot movements and motor imageries. *Clinical Neurophysiology*, 119(11):2570–2578, 2008.

[113] Malin CB Åberg and Johan Wessberg. Evolutionary optimization of classifiers and features for single-trial EEG discrimination. *Biomedical Engineering Online*, 6(1):32, 2007.

[114] AK Mohamed, Tshilidzi Marwala, and LR John. Single-trial EEG discrimination between wrist and finger movement imagery and execution in a sensorimotor BCI. In *2011 Annual International Conference of the IEEE Engineering in Medicine and Biology Society*, pages 6289–6293. IEEE, 2011.

[115] Glenn F Wilson, CA Russell, JW Monnin, JR Estepp, and JC Christensen. How does day-to-day variability in psychophysiological data affect classifier accuracy? In *Proceedings of the Human Factors and Ergonomics Society Annual Meeting*, volume 54, pages 264–268. SAGE Publications Sage CA: Los Angeles, CA, 2010.

[116] Maureen Clerc, Laurent Bougrain, and Fabien Lotte. *Brain-Computer Interfaces 1: Methods and Perspectives*. John Wiley & Sons, 2016.

.1 Appendix

Software Listing

This appendix contains code used in this dissertation. The below codes were written in the Python and C++ programming languages.

.1.1 Accelerometer code

```cpp
#include <Wire.h>
#include <SPI.h>
#include <Adafruit_LIS3DH.h>
#include <Adafruit_Sensor.h>
// I2C
Adafruit_LIS3DH lis = Adafruit_LIS3DH();


const int outPin = 9;


void setup(void) {
#ifndef ESP8266
  while (!Serial);      // will pause Zero, Leonardo, etc until serial console
    opens
#endif


  Serial.begin(115200);
  pinMode(outPin, OUTPUT);   //Set pin 9 as 'output'


  if (! lis.begin(0x18)) {
    while (1);
  }
}


void loop() {
  sensors_event_t event;
```

```
lis.getEvent(&event);
float y = event.acceleration.y;
Serial.println(y);


if (y > −0.4){
  digitalWrite(outPin,LOW);
}


Serial.println(y);
else{
  digitalWrite(outPin,HIGH);
}
          }
}
```

.1.2   Python code for protocol displaying

```
import time
import sys
import matplotlib
matplotlib.use('TkAgg')
import matplotlib.pyplot as plt
import matplotlib.animation as animation
import numpy as np
from time import gmtime, strftime
import signal
import serial
import pyfirmata



S1 = 3
S2 = 5
```

```python
board = pyfirmata.Arduino('COM3')
board.digital[S1].write(1)
board.digital[S2].write(1)


nChannels = 8

class Protocol(object):

    ####### Initialization    #######
    def __init__(self, nChannels):

        # Constant Parameters
        self.nChannels = nChannels

        self.restDuration = 2   # seconds
        self.moveCommandDuration = 2   # seconds
        self.moveDuration = 2   # seconds

        # Set up display
        self.fig = plt.figure()   # figsize=(10,6)) # (38,20))
        self.fig.patch.set_facecolor('black')
        mng = plt.get_current_fig_manager()
        mng.full_screen_toggle()   # tk on ubuntu
        self.ax = plt.subplot(111, xlim=(0., 6 + 1.5), ylim=(4 + 2, 0.))
        self.text = self.ax.text(3, 3, 'test',
                                      fontsize=50, family='monospace',
                                      color='white', verticalalignment='bottom')

        self.ax.axis('off')


    ####### Initialize the animation #######

    def initAnimation(self):
```

```python
        """Initialize the animation."""
        self.state = 'rest'   # or 'command' or 'move'
        self.text.set_text('')
        self.endCurrentEvent = time.time() + self.restDuration
        self.realMovement = True
        return [self.text]


    ####### Animation #######


    def animate(self, i):
        """Update animation one step."""
        now = time.time()
        if now > self.endCurrentEvent:
            if self.state == 'rest':
                self.text.set_text('   +')
                board.digital[S1].write(0)
                self.state = 'command'
                self.endCurrentEvent = time.time() + self.moveCommandDuration


            elif self.state == 'command':
                board.digital[S1].write(1)


                self.state = 'move'


                self.text.set_text('Move')   # + self.figureNames[self.fingerr
])
                board.digital[S2].write(0)


                self.endCurrentEvent = time.time() + self.moveDuration



            elif self.state == 'move':
                board.digital[S2].write(1)
```

102

```python
                self.state = 'rest'
                self.marker = 0
                self.text.set_text(' ')
                self.endCurrentEvent = time.time() + self.restDuration


        return [self.text]



protocol = Protocol(nChannels)
anim = animation.FuncAnimation(protocol.fig, protocol.animate,
                                init_func=protocol.initAnimation,
                                repeat=False,
                                interval=0.0,
                                blit=True)


plt.show()
```